AFRL-AFOSR-UK-TR-2024-0022

IRONCASTLE - Interpretation and Recognition of Objects using Novel Coupled Attitude and Shape Techniques for Lightcurve Evaluation

Frueh, Carolin
PURDUE UNIVERSITY
2550 NORTHWESTERN AVE # 1100
WEST LAFAYETTE, IN, 47906
USA

02/13/2024
Final Technical Report

DISTRIBUTION A: Distribution approved for public release.

Air Force Research Laboratory
Air Force Office of Scientific Research
European Office of Aerospace Research and Development
Unit 4515 Box 14, APO AE 09421

REPORT DOCUMENTATION PAGE

PLEASE DO NOT RETURN YOUR FORM TO THE ABOVE ORGANIZATION.

1. REPORT DATE	2. REPORT TYPE	3. DATES COVERED	
20240213	Final	START DATE 20190901	END DATE 20230531

4. TITLE AND SUBTITLE
IRONCASTLE - Interpretation and Recognition of Objects using Novel Coupled Attitude and Shape Techniques for Lightcurve Evaluation

5a. CONTRACT NUMBER	5b. GRANT NUMBER	5c. PROGRAM ELEMENT NUMBER
	FA9550-19-1-0407	61102F

5d. PROJECT NUMBER	5e. TASK NUMBER	5f. WORK UNIT NUMBER

6. AUTHOR(S)
Carolin Frueh

7. PERFORMING ORGANIZATION NAME(S) AND ADDRESS(ES)
PURDUE UNIVERSITY
2550 NORTHWESTERN AVE # 1100
WEST LAFAYETTE, IN 47906
USA

8. PERFORMING ORGANIZATION REPORT NUMBER

9. SPONSORING/MONITORING AGENCY NAME(S) AND ADDRESS(ES)	10. SPONSOR/MONITOR'S ACRONYM(S)	11. SPONSOR/MONITOR'S REPORT NUMBER(S)
EOARD UNIT 4515 APO AE 09421-4515	AFRL/AFOSR IOE	AFRL-AFOSR-UK-TR-2024-0022

12. DISTRIBUTION/AVAILABILITY STATEMENT
A Distribution Unlimited: PB Public Release

13. SUPPLEMENTARY NOTES

14. ABSTRACT
In this contract, attitude inversion based on light curves is performed. The results have been highly successful, as outlined in the technical portion of the report. It presents the first method to determine an attitude from a short light curve alone, when the albedo-shape and the observation geometry is known. The method does not need any initial guess, it fully explores all ambiguities of the problem, and it does not require a simple attitude motion, such as a constant spinner, but can determine any attitude motion, including tumbling, spinning, and stable.

15. SUBJECT TERMS

16. SECURITY CLASSIFICATION OF:			17. LIMITATION OF ABSTRACT	18. NUMBER OF PAGES
a. REPORT	b. ABSTRACT	c. THIS PAGE		
U	U	U	SAR	131

19a. NAME OF RESPONSIBLE PERSON	19b. PHONE NUMBER *(Include area code)*
MICHAEL YAKES	00000000

Standard Form 298 (Rev.5/2020)
Prescribed by ANSI Std. Z39.18

DISTRIBUTION A: Distribution approved for public release.

IRONCASTLE - Interpretation and Recognition of Objects using Novel Coupled Attitude Techniques for Lightcurve Evaluation

Prof. Dr. Carolin Frueh (PI)

AFOSR FA9550-19-1-0407
Final Report

Abstract

In this contract, attitude inversion based on light curves is performed. The results have been highly successful, as outlined in the technical portion of the report. It presents the first method to determine an attitude from a short light curve alone, when the albedo-shape and the observation geometry is known. The method does not need any initial guess, it fully explores all ambiguities of the problem, and it does not require a simple attitude motion, such as a constant spinner, but can determine any attitude motion, including tumbling, spinning, and stable.

1 Section 1: Structured Survey Questions

1.1 Award Information

You will be asked for the following information in the survey. The majority of these fields will be sent pre-populated, but can be edited if necessary. You will be able to manually edit any of these fields if information needs to be updated.

- Award Number (Federal Award Identification Number FA9550-19-1-0407)
- Report Type: Final Report
- Principal Investigator: Carolin Frueh
- Principal Investigator Email: cfrueh@purdue.edu

DISTRIBUTION A: Distribution approved for public release.

- Principal Investigator Phone: (765) 494-7436
- Project Title: IRONCASTLE
- Recipient Organization: Purdue University
- Business Office Email:
- Report Due Date: 1 September, 2019
- Report Period Start Date:
- Report Period End Date: May 31, 2023
- Current Program Officer: Michael Yakes

1.2 Publications

L. Robinson, C. Frueh, Light Curve High Fidelity Simulation and Digital Twin, Journal of Astronautical Sciences, in preparation

A. Burton, L. Robinson, C. Frueh, Light Curve Attitude Estimation using Particle Swarm Optimizers, Journal of Guidance, Control, and Dynamics, submitted 2024

A. Friedman, C. Frueh, Observability of Light Curve Inversion for Shape and Feature Determination Exemplified by a Case Analysis, Journal of Astronautical Sciences, 69, 537–569, 10.1007/s40295-021-00293-w, Feb 2022

A. Burton, C. Frueh, Attitude Estimation using Light Curves: A Particle Swarm Approach, SciTech Symposium, Jan 2024

A. Burton, Fast Light Curve Inversion for Regular and Tumbling Attitude Motion, The Advanced Maui Optical and Space Surveillance Technologies (AMOS) Conference, Sep, 2023

A. Burton, C. Frueh, Multi-Hypothesis Light Curve Inversion for Space Object Attitude Determination, 8th European Conference on Space Debris, April 2021

A. Burton, C. Frueh, Mapping the Solution Space for Light Curve Attitude Estimation, COSPAR Scientific Assembly, Feb. 2021

A. Burton, C. Frueh, Light Curve Attitude Estimation Using the Viewing Sphere

DISTRIBUTION A: Distribution approved for public release.

AIAA/AAS Astrodynamics Specialist Conference, Aug. 2020

A. Friedman, C. Frueh, Observability of Light Curve Shape Inversion Based on Optical Data, First Orbital Debris Conference, Houston, TX, Dec. 2019

Alexander Burton, PhD thesis, Attitude and Shape Determination of Space Objects using Light Curves, School of Aeronautics and Astronautics, Purdue University, to be completed Spring 2024

Liam Robinson, MS thesis, Light Curve Simulation And Shape Inversion For Human-Made Space Objects, School of Aeronautics and Astronautics, Purdue University, 2023 (about 50% of the thesis pertains to this contract)

Alex Friedman, PhD thesis, Observability Analysis for Space Situational Awareness, School of Aeronautics and Astronautics, Purdue University, 2020 (about 30% of the thesis pertains to this contract)

1.3 Participants

You will be asked to provide the information below for: (1) PIs; and (2) each person who worked on and was funded by this grant during the current reporting period. Please include all participants including yourself.

- Carolin Frueh, PI
  - ORCID: 0000-0002-0240-5509
  - Project lead
- Alexander Burton
  - PhD student, main student researcher on the project. Development of viewing sphere, analytic expressions, particle swarm approach
- Liam Robinson
  - PhD student, formerly MS student. Development of the high fidelity light curve simulation. Speed up in the simulation which allowed for the inversion of complexly shaped objects.
- Alex Friedmann
  - PhD student, research into the obervability of the light curve inversion problem.

DISTRIBUTION A: Distribution approved for public release.

2 Section 2: Technical Report

2.1 Accomplishments

Principal Discipline: The use of particle swarm optimizers (PSOs) for estimating the attitude of an artificial space object from its observed brightness over time (i.e., its light curve) is a significant improvement on existing techniques. Most current methods of extracting attitude information from an object's light curve either require a good initial guess for how the object is rotating, assume that the object is moving in specific ways–such as mostly spinning around one axis–or are limited to objects of a particular shape. Ideally, an attitude estimation method would not require any information about the object's rotation up-front and would be applicable to an object of any shape and undergoing any kind of rotation.

The PSO method developed in this project makes significant progress towards these goals. It assumes no information about the object's rotation is known; only its shape, reflective properties, and position are needed. In principle, the method also works on light curves produced by objects of any shape and undergoing any rotation. The current implementation does assume that the object is not experiencing torques from external objects. This assumption is made only to reduce computation time and is a reasonable first approximation of the rotation of most space objects. A more general dynamics model can be used to include the effects of external torques, though it would require a much higher computational cost.

In addition to being more generally applicable than many existing methods, the PSO method also takes the ambiguity of the attitude estimation problem into account. Since light curves only include information about the total amount of light reflected off an object at different points in time, a single light curve can correspond to multiple attitude time histories. For example, the same light curve could be produced by the observed object rotating quickly around a fixed axis or slowly tumbling in a complex pattern. The PSO method addresses this issue by trying out many estimated attitude time histories and reporting which fit the observed light curve best. If no estimate clearly fits the observations better than the others, then further observations can be taken as needed to narrow down the possible estimates.

For the above reasons, the PSO method is a significant step towards developing more general and robust techniques for estimating attitude using the minimal information provided by light curves.

Adjacent Disciplines: The research highlights the flexibility of the swarm optimization, but also how much support even a flexible optimizer needs. The research has been picked up in the resolved attitude determination in satellite inspection scenarios.

DISTRIBUTION A: Distribution approved for public release.

The analytic attitude expressions have gained wide interested in the field of general dynamics in the general context, not limited to space, satellites or characterization.

Dissemination Dissemination took place through journal publications, conference presentations and proceeding papers. Invited Keynote speaker at the 3rd IAA Conference on Space Situational Awareness, Apr. 4-6, 2022, Tres Cantos, Madrid, 2022. Outreach at the West Lafayette Highschool and at the West Lafayette Astronomy Club.

2.2 Impacts

In this project the first ever attitude inversion method from light curves without any a priori information has been accomplished. The albedo-shapes need to be known, but there are no restrictions on the object shape, fully realistic satellites are feasible. There are no restrictions on the type of attitude motion; stable spin is not required!

As a result, this project has a high impact. It has lead to follow-up contracting with the European Space Agency and has attracted a lot of attention for commercialization as an attitude determnination product and for the mission support for active debris removal. Interested companies are, among others, Katalyst, Comspoc, Astroscale.

As a side effect the analytic attitude expressions have impacted the general field of rigid body dynamics.

2.3 Changes

A method using particle swarm optimizers to estimate the initial attitude and angular velocity states of an object of interest based on its light curve was developed. Since this is a different method than was discussed in the 2020-2021 interim report, the report begins by discussing the reasons for the changes.

2.3.1 Phasing out the Viewing Sphere

In Burton and Frueh [1] and Burton and Fan [2], the concept of the viewing sphere was used to more efficiently search attitude space for orientations that could have produced the brightness measurements in the light curve. These orientations are referred to as pseudo-measurements. While the viewing sphere method thoroughly searched the attitude space for a given shape and phase angle between the object-sun and object-observer directions, it required significant up-front computation costs. Therefore, to reduce the computation time required to find pseudo-measurements for new shapes and phase angles, a particle swarm optimizer was implemented to find pseudo-measurements.

DISTRIBUTION A: Distribution approved for public release.

2.3.2 Phasing out the Probability Hypothesis Density Filter

The 2020-2021 interim report discusses a light curve inversion method using a probability hypothesis density (PHD) filter. The PHD filter was adopted because of two significant features of the attitude estimation problem using light curves: (1) Since light curve measurements do not generally correspond to a single attitude, an approach must be used that can take the fact of multiple possible attitudes at each time step into account; and (2) the computational cost of propagating extremely large numbers of possible attitudes forward in time makes trying every possible combination of attitudes at each measurement time infeasible.

The PHD filter addressed the above issues by representing the object's state estimate as a probability density function, thus accounting for multiple possible solutions given ambiguous data and automatically removing state estimates that are very unlikely to be true, thus reducing the computational cost. It was later discovered, however, that the computational cost associated with propagating attitude estimates could be greatly reduced by using analytic solutions to the torque-free rotational equations of motion. The reduced computational cost made other estimation methods feasible and led to the adoption of a particle swarm optimizer (PSO) for solving the light curve inversion problem. Using a PSO along with an interior-point algorithm has the advantage of producing precise attitude estimates while having a fast run time due to using analytic instead of numeric propagation. More details and some representative results are discussed later in the report.

2.3.3 Particle Swarm Optimizer

As switch has been made to the Particle Swarm Optimizer. The particle swarm optimizers were based on the local version presented by Eberhart and Kennedy [3]. Their optimizer uses many particles (each representing a state estimate) to search for the minimum of an objective function J. Each particle moves through the domain of the function, keeping track of where the lowest J value it has seen was located (its "personal best"). Each particle also keeps track of the lowest J value seen by its neighbors (the "local best"). At each update step, the particles accelerate randomly towards their personal and local bests. The solver is run until some stopping condition is met. For our purposes, the stopping condition is a certain number of iterations. The personal bests of each of the particles are used to locate the local minima of the objective function, which correspond to pseudo-measurements or plausible attitude time histories, depending on the application.

DISTRIBUTION A: Distribution approved for public release.

References

[1] Alex Burton and Carolin Frueh. Light curve attitude estimation using the viewing sphere. In *Astrodynamics Specialist Conference 2020*, 2020.

[2] Alexander Burton and Siwei Fan. Mapping the solution space for light curve attitude estimation. *43rd COSPAR Scientific Assembly. Held 28 January-4 February*, 43:2193, 2021.

[3] Russell Eberhart and James Kennedy. A new optimizer using particle swarm theory. In *MHS'95. Proceedings of the sixth international symposium on micro machine and human science*, pages 39–43. Ieee, 1995.

DISTRIBUTION A: Distribution approved for public release.

Technical Details and Showing off the Exciting Results

In the following, we are attaching the journal paper, which comprehensively shows the exciting results from this contract, stating the robust attitude determination without a priori attitude information for realistic satellite shapes from light curves.

Furthermore we are attaching the write-up of our digital twin, which allowed the realistic simulation of the light curves even for complex shapes with significant self-shadowing.

DISTRIBUTION A: Distribution approved for public release.

Light Curve Attitude Estimation using Particle Swarm Optimizers

Alexander Burton *, Liam Robinson†, and Carolin Frueh‡
Purdue University, West Lafayette, IN 47907

Knowledge of the attitude of a space object is useful in space situational awareness for independently evaluating a satellite's health and characterizing unknown objects. In cases where only non-resolved optical observations are available, the object's attitude may be estimated using a time sequence of brightness observations, also known as the light curve. This attitude estimation problem is plagued with multiple difficulties: even in the absence of noise and when all other relevant factors are perfectly known, the non-uniqueness of the problem means that multiple attitude time histories may fit the light curve equally well. In addition, there is often insufficient information about the object to generate an initial state guess for an estimator. This paper presents a method that estimates an observed object's attitude and angular velocity while accounting for ambiguities and without needing any initial state guess. The only inputs are the light curve, the object's albedo shape, and the object's position relative to the Sun and the observer. The ability of the estimator to resolve attitude time histories is demonstrated using simulated light curves by comparing state estimates against known true states.

I. Introduction

Space object characterization is a crucial component of space situational awareness. Knowledge of an object's type, shape, reflective properties, and attitude dynamics is useful for identifying the space object, judging its operational state, and predicting its future orbital motion. Optical systems may be used for characterization, but space objects are often too far from an observer for a resolved image to be obtained. In such cases where a resolved image is unavailable, the total brightness of the light from the Sun reflected off the observed object can still be measured. A series of brightness measurements taken over time is called a light curve. Light curves are influenced by the object's shape, material properties, attitude, and position relative to the Sun and observer. The problem of estimating an object's attitude over time from its light curve is also referred to as the attitude inversion problem.

Light curve inversion to estimate a space object's shape and attitude has been studied for over a century [1–7] but, with some exceptions [2], was initially focused on natural bodies such as asteroids. When analyzing the light curve of

*Graduate Student, School of Aeronautics and Astronautics, 701 W. Stadium Ave, West Lafayette, IN 47907, and AIAA Student Member.
†Graduate Student, School of Aeronautics and Astronautics, 701 W. Stadium Ave, West Lafayette, IN 47907, and AIAA Student Member.
‡Associate Professor, School of Aeronautics and Astronautics, 701 W. Stadium Ave, West Lafayette, IN 47907, and AIAA Senior Member.

DISTRIBUTION A: Distribution approved for public release.

a natural body, certain simplifying assumptions can be made, such as that the body is undergoing stable single-axis rotation and its surface is smooth and diffusely reflective [5, 6].

More recently, light curve inversion began to be studied for artificial objects in Earth orbit [8–13]. However, the simplifying assumptions used when investigating natural bodies do not apply to artificial satellites. Satellites are made up of various materials with different reflective properties, their shapes are generally angular rather than smooth, and they are frequently shiny instead of purely diffusely reflecting [9]. Furthermore, satellites cannot always be assumed to be undergoing stable single-axis rotation [9]. Even if a satellite is initially spin-stabilized, its rotation will slow due to the presence of eddy currents [14], and other effects such as solar radiation pressure and shadowing effects will eventually lead to unstable attitude motion [12, 15]. Because of the increased complexity of the light curve inversion problem for artificial objects, it is not uncommon for the shape estimation and attitude estimation components of the inversion process to be examined separately [9, 10, 16–18].

Current attitude inversion methods often require an initial guess for the observed object's attitude and angular velocity [10, 11, 13, 19]. However, initial guesses are not always available, particularly for objects such as space debris or a tumbling satellite, and many attitude estimation methods can only converge to the correct state if the initial state guess is sufficiently good [19]. Convergence is particularly sensitive to errors in the initial angular velocity guess, with multiple authors [10, 20] finding that an unscented Kalman filter (UKF) will only converge for angular velocity errors below 2 deg/s. Using polarized light curve measurements allows convergence for 2 deg/s of angular velocity error, but only if the attitude guess is within 0.6° of the truth [20].

If no *a priori* attitude information is available, then another difficulty is encountered in addition to convergence: the ambiguity of the light curve measurements themselves with respect to attitude. Even in the absence of noise and when the observed object's shape, reflective properties, and position relative to the Sun and the observer are perfectly known, each individual measurement in a light curve generally corresponds to many different attitudes [17, 19, 21–23], and the entire light curve might fit multiple attitude time histories [11, 13, 22, 24]. Methods such as the particle filter [11] or adaptive Gaussian filter [13] are capable of describing the attitude estimate's multimodal probability distribution but still require an initial guess and do not take the entirety of the solution space into account.

One method that does not require an initial state guess has been developed by Clark et al. [22, 25]. This method uses a particle swarm optimizer (PSO) to estimate attitude and optical properties from light curves obtained by space-based observers. A PSO searches the solution space of an optimization problem using particle motion modeled on the social behavior of animals [26]. The attitude inversion approach developed by Clark et al. [22, 25] uses a PSO to identify possible attitudes at each time step. A first derivative test is used to eliminate impossible transitions between attitudes without taking the full rotational dynamics of the object into account [22, 25].

The method in this study was developed independently of Clark et al. [22, 25] and uses two PSOs to estimate the attitude and angular velocity of an observed object while fully modeling torque-free rotational dynamics. Only

DISTRIBUTION A: Distribution approved for public release.

the object's shape, reflective properties, and position relative to the Sun and observer are assumed to be known. The projected use case is for a known piece of space debris or a satellite that is no longer communicating with its operators. Such situations where there is no *a priori* information about the object's attitude and rotational motion are particularly envisioned.

The structure of the remainder of the paper is as follows: Section II describes the analytic attitude solutions used for torque-free attitude propagation, then the two PSOs are outlined in Section III. The phenomenon of "flipped" attitude estimates and how they can be leveraged to generate new estimates is discussed in Section IV. Section V discusses the state estimates generated by applying the PSO inversion method to noiseless simulated light curves of both simple and complex objects. This publication collects and expands on the material previously published as conference proceedings by Burton and Frueh [24] and Burton et al. [27, 28].

II. Analytic Torque-Free Motion

A. Motivation and Attitude Representation

Numeric integration of the rotational equations of motion is computationally expensive, so analytic solutions for the torque-free case are used to propagate attitude quickly in the context of a PSO. Note that rotations are approximately torque-free only over short intervals. For long observation windows, the torques acting on the observed object need to be taken into account. The object's attitude is described using its precession ϕ, nutation θ, and spin ψ angles relative to the angular momentum vector $\boldsymbol{H}$. The angular velocity of the object $\boldsymbol{\omega} = [\omega_x \quad \omega_y \quad \omega_z]^T$ is written in the body-fixed coordinate frame $\hat{b}$. The expressions described in this section apply to any torque-free rotation, including multi-axis tumbling. They may be used for an object with three distinct moments of inertia (MOI) or repeated MOI.

Analytic expressions for the torque-free angular velocity $\boldsymbol{\omega}(t)$ are readily available [29-31]. However, the expressions for $\phi(t)$, $\theta(t)$, and $\psi(t)$ are not often listed, even in textbooks, likely because of the length and complexity of the expressions [32]. As such, the torque-free attitude expressions used by the light curve inversion PSO method are fully written out in this section.

Torque-free attitude motion can be divided into short-axis mode (SAM) and long-axis mode (LAM) rotations. Let the body-fixed coordinate system $\hat{b}$ be a principal axis system such that $I_x \leq I_y \leq I_z$, where I_i is the moment of inertia about $\hat{b}_i$. SAM and LAM rotations can be distinguished mathematically using the dynamic moment of inertia I_d [33]:

$$I_d = \frac{H^2}{2T} \tag{1}$$

where H is the angular momentum magnitude and T is the rotational kinetic energy. If $I_d > I_y$, the object is rotating principally about $\hat{b}_z$ and undergoing SAM rotation. On the other hand, if $I_d < I_y$, the object is undergoing LAM rotation principally about $\hat{b}_x$. If I_d is equal to any of the moments of inertia I_i, then the object is undergoing a single-axis

DISTRIBUTION A: Distribution approved for public release.

rotation about $\hat{b}_i$.

In this study, the attitude of the object is represented using the rotation quaternion $\boldsymbol{q} = (s, \boldsymbol{v})$ from the space-fixed inertial frame $\hat{b}$ to the body-fixed frame, where s is the scalar component and $\boldsymbol{v}$ is the vector component [34]. The attitude over time $\boldsymbol{q}(t)$ is computed as follows:

$$\boldsymbol{q}(t) = \Delta\boldsymbol{q}_{\text{SAM/LAM}} \otimes \boldsymbol{q}_0 \tag{2}$$

where $\boldsymbol{q}_0$ is the quaternion rotating from the space-fixed frame to the body-fixed frame at the initial time step t_0 and $\Delta\boldsymbol{q}_{\text{SAM/LAM}}$ represents the change in the attitude from the initial time. Because of the form of the torque-free attitude solution, the $\Delta\boldsymbol{q}_{\text{SAM/LAM}}$ unit quaternion is, in turn, related to an Euler angle sequence formed out of the precession ϕ, nutation θ, and spin ψ angles. A 313 (ϕ, θ, ψ) Euler angle sequence is used for SAM rotations, and a 131 (ϕ, θ, ψ) Euler angle sequence is used for LAM rotations.

In the case of torque-free rotation, Euler angles may be safely used to propagate attitude analytically without encountering singularities. For the 313 and 131 sequences, gimbal lock only occurs if $\sin\theta = 0$. However, θ is just the angle between $\boldsymbol{H}$ and either $\hat{b}_z$ or $\hat{b}_x$, meaning that if $\sin\theta = 0$ then the object is undergoing single-axis rotation such that $\boldsymbol{\omega} = \omega\hat{b}_z$ for SAM or $\boldsymbol{\omega} = \omega\hat{b}_x$ for LAM. Because no torque is applied to the object, it will never encounter a singularity unless it is initially rotating about only one axis. For objects that start out rotating about a body frame unit vector $\hat{b}_i$, i.e., $I_d = I_i$, a simplified attitude expression can be used that eliminates the need for Euler angles:

$$\Delta\boldsymbol{q}_i(t) = \left(\cos\left(\frac{\omega t}{2}\right), -\sin\left(\frac{\omega t}{2}\right)\hat{b}_i\right) \tag{3}$$

For the general torque-free case, expressions for $\Delta\boldsymbol{q}_{\text{SAM/LAM}}$ are used that involve the Euler angles ϕ, θ, and ψ and the angular momentum unit vector $\hat{h} = \boldsymbol{H}/H = [h_x \quad h_y \quad h_z]^T$. For SAM rotations, the $\Delta\boldsymbol{q}_{\text{SAM}}$ quaternion is as follows:

$$\Delta\boldsymbol{q}_{\text{SAM}}(\phi,\theta,\psi) = \frac{1}{\sqrt{2(h_z+1)}}\left(\begin{array}{c}(h_z+1)\cos\frac{\theta}{2}\cos\left(\frac{\phi+\psi}{2}\right) + \sin\frac{\theta}{2}\left(h_y\cos\left(\frac{\phi-\psi}{2}\right) - h_x\sin\left(\frac{\phi-\psi}{2}\right)\right), \\ \begin{bmatrix} -(h_z+1)\sin\frac{\theta}{2}\cos\left(\frac{\phi-\psi}{2}\right) - \cos\frac{\theta}{2}\left(x\sin\left(\frac{\phi+\psi}{2}\right) - h_y\cos\left(\frac{\phi+\psi}{2}\right)\right) \\ -(h_z+1)\sin\frac{\theta}{2}\sin\left(\frac{\phi-\psi}{2}\right) - \cos\frac{\theta}{2}\left(h_x\cos\left(\frac{\phi+\psi}{2}\right) + h_y\sin\left(\frac{\phi+\psi}{2}\right)\right) \\ -(h_z+1)\cos\frac{\theta}{2}\sin\left(\frac{\phi+\psi}{2}\right) + \sin\frac{\theta}{2}\left(h_x\cos\left(\frac{\phi-\psi}{2}\right) + h_y\sin\left(\frac{\phi-\psi}{2}\right)\right) \end{bmatrix}\end{array}\right) \tag{4}$$

For LAM rotations, $\Delta\boldsymbol{q}_{\text{LAM}}$ is:

DISTRIBUTION A: Distribution approved for public release.

$$\Delta \boldsymbol{q}_{\mathrm{LAM}}(\phi,\theta,\psi) = \frac{1}{\sqrt{2(h_x+1)}}\left((h_x+1)\cos\frac{\theta}{2}\cos\left(\frac{\phi+\psi}{2}\right) - \sin\frac{\theta}{2}\left(h_z\sin\left(\frac{\phi-\psi}{2}\right) + h_y\cos\left(\frac{\phi-\psi}{2}\right)\right)\right.$$
$$\left.\begin{bmatrix} -(h_x+1)\cos\frac{\theta}{2}\sin\left(\frac{\phi+\psi}{2}\right) + \sin\frac{\theta}{2}\left(h_z\cos\left(\frac{\phi-\psi}{2}\right) - h_y\sin\left(\frac{\phi-\psi}{2}\right)\right) \\ (h_x+1)\sin\frac{\theta}{2}\sin\left(\frac{\phi-\psi}{2}\right) + \cos\frac{\theta}{2}\left(h_z\cos\left(\frac{\phi+\psi}{2}\right) - h_y\sin\left(\frac{\phi+\psi}{2}\right)\right) \\ -(h_x+1)\sin\frac{\theta}{2}\cos\left(\frac{\phi-\psi}{2}\right) - \cos\frac{\theta}{2}\left(h_y\cos\left(\frac{\phi+\psi}{2}\right) + h_z\sin\left(\frac{\phi+\psi}{2}\right)\right) \end{bmatrix}\right) \tag{5}$$

The expressions in Eq. (4) and Eq. (5) are derived in the Appendix.

B. Short-Axis Mode (SAM) Expressions

The analytic expressions for SAM angular velocity $\boldsymbol{\omega}(t)$ are taken from Benson et al. [33]. The same solution is found in Samarasinha and A'Hearn [30], and similar ones are derived in Thomson [29] and Murakami [31]:

$$\begin{aligned} \omega_x(t) &= \pm\omega_e\sqrt{\frac{I_d(I_z-I_d)}{I_x(I_z-I_x)}}\,\mathrm{cn}(\tau,k) \\ \omega_y(t) &= \pm\omega_e\sqrt{\frac{I_d(I_z-I_d)}{I_y(I_z-I_y)}}\,\mathrm{sn}(\tau,k) \\ \omega_z(t) &= \pm\omega_e\sqrt{\frac{I_d(I_d-I_x)}{I_z(I_z-I_x)}}\,\mathrm{dn}(\tau,k) \end{aligned} \tag{6}$$

where $\mathrm{sn}(\tau,k)$, $\mathrm{cn}(\tau,k)$, and $\mathrm{dn}(\tau,k)$ are the Jacobi elliptic functions [35], and I_d is the dynamic moment of inertia defined in Eq. (1). If the body frame $\hat{b}$ is not defined such that $I_x \le I_y \le I_z$, then it may be transformed such that the MOI are properly ordered before propagating and transformed back afterward.

The sign of each ω_i component is chosen based on the initial angular velocity $\boldsymbol{\omega}(t_0)$. All terms take the positive sign if $\omega_z(t_0) \ge 0$. If $\omega_z(t_0) < 0$, then ω_z and ω_y take the negative sign unless $\omega_y(t_0) = 0$. In that case, ω_z and ω_x are given the negative sign.

The constant k is the elliptic modulus, τ is a timelike parameter, and ω_e is the effective spin rate. The constants k and ω_e are calculated as follows:

$$k^2 = \frac{(I_y-I_x)(I_z-I_d)}{(I_z-I_y)(I_d-I_x)} \qquad\qquad \omega_e = \frac{2T}{H} \tag{7}$$

And the parameter τ is:

DISTRIBUTION A: Distribution approved for public release.

$$
\begin{aligned}
\tau &= n_\tau (t - t_0) + \tau_0 \\
n_\tau &= \omega_e \sqrt{\frac{I_d (I_d - I_x)(I_z - I_y)}{I_x I_y I_z}} \\
\tau_0 &= \int_0^\Phi \frac{1}{\sqrt{1 - k^2 \sin^2 x}} dx = F(\Phi | k^2)
\end{aligned}
\tag{8}
$$

where $F(\Phi|k^2)$ is the incomplete elliptic integral of the first kind [35]. The angle Φ in Eq. (8) is an angle based on the initial angular velocity $\boldsymbol{\omega}(t_0)$:

$$
\Phi = \tan^{-1}\left(\sqrt{\frac{I_y (I_z - I_y)}{I_x (I_z - I_x)}} \frac{\omega_y(t_0)}{\omega_x(t_0)} \right) \tag{9}
$$

The analytic expressions for torque-free SAM rotation follow Murakami [31]. The nutation angle $\theta(t)$ and spin angle $\psi(t)$ are found by relating the angular momentum unit vector to the Euler angle sequence. Note that the nutation angle $\theta(t)$ is limited to the range $[0, \pi]$.

$$
\theta(t) = \cos^{-1}\left(\frac{I_z \omega_z(t)}{H} \right) \tag{10}
$$

$$
\psi(t) = \tan^{-1}\left(\frac{I_x \omega_x(t)}{I_y \omega_y(t)} \right) \tag{11}
$$

The precession angle $\phi(t)$ is found using the relation between the Euler angle derivative and the body-frame angular velocity [36]:

$$
\dot{\phi} = \frac{1}{\sin\theta} \left(\omega_x \sin\psi + \omega_y \cos\psi \right) \tag{12}
$$

After integrating, the solution is found to be [31]:

$$
\phi(t) = \frac{H}{I_z}(t - t_0) - \frac{H(I_x - I_z)}{n_\tau I_x I_z} \left[\Pi\left(\mathrm{am}(n_\tau t + \tau_0), -\frac{I_z(I_y - I_x)}{I_x(I_z - I_y)}, k \right) - \Pi\left(\mathrm{am}(\tau_0), -\frac{I_z(I_y - I_x)}{I_x(I_z - I_y)}, k \right) \right] \tag{13}
$$

where $\mathrm{am}(\tau, k)$ is the Jacobi amplitude function [35]. The constants k, n_τ, and τ_0 are defined in Eq. (7) and Eq. (8).

The Π function is the Jacobi incomplete elliptic integral of the third kind [37]. While Π is useful for the mathematical derivation, the equivalent symmetric elliptic integrals are more convenient when numerically computing the integral

DISTRIBUTION A: Distribution approved for public release.

[37, 38].

C. Long-Axis Mode (LAM) Expressions

An alternate set of angular velocity and attitude equations is used if the object is undergoing LAM rotation. The LAM angular velocity functions [33] are as follows:

$$\begin{aligned}
\omega_x(t) &= \pm\omega_e\sqrt{\frac{I_d(I_z - I_d)}{I_x(I_z - I_x)}}\,\mathrm{dn}(\tau, k) \\
\omega_y(t) &= \pm\omega_e\sqrt{\frac{I_d(I_d - I_x)}{I_y(I_y - I_x)}}\,\mathrm{sn}(\tau, k) \\
\omega_z(t) &= \pm\omega_e\sqrt{\frac{I_d(I_d - I_x)}{I_z(I_z - I_x)}}\,\mathrm{cn}(\tau, k)
\end{aligned} \tag{14}$$

where the sign of each term is chosen based on the initial angular velocity $\boldsymbol{\omega}(t_0)$. All terms take the positive sign if $\omega_x(t_0) \geq 0$. If $\omega_x(t_0) < 0$, then ω_x and either ω_y or ω_z are given the negative sign. If $\omega_y(t_0) = 0$, then ω_z takes the negative sign; otherwise, ω_y is given it. The parameter τ is defined as in Eq. (8) except that n_τ and τ_0 are given different expressions. The new values for the elliptic modulus k and n_τ are given below:

$$\begin{aligned}
k^2 &= \frac{(I_y - I_z)(I_x - I_d)}{(I_y - I_x)(I_z - I_d)} \\
n_\tau &= \omega_e\sqrt{\frac{I_d(I_z - I_d)(I_y - I_x)}{I_x I_y I_z}}
\end{aligned} \tag{15}$$

and τ_0 is computed as in Eq. (8) with Φ for the LAM case now satisfying the following expression:

$$\Phi = \tan^{-1}\left(\sqrt{\frac{I_y(I_y - I_x)}{I_z(I_z - I_x)}}\,\frac{\omega_y(t_0)}{\omega_z(t_0)}\right) \tag{16}$$

The LAM attitude solution is found in a similar way to the one in Murakami [31]; however, it uses a 131 Euler angle sequence so that ϕ, θ, and ψ are still the precession, nutation, and spin angles, respectively. Because of this change, the expressions are slightly different.

$$\theta(t) = \cos^{-1}\left(\frac{I_x\omega_x(t)}{H}\right) \tag{17}$$

$$\psi(t) = \tan^{-1}\left(\frac{I_z\omega_z(t)}{-I_y\omega_y(t)}\right) \tag{18}$$

DISTRIBUTION A: Distribution approved for public release.

A negative sign is included in the denominator of Eq. (18) so that the quadrant of $\psi(t)$ can be accurately determined.

The precession angle ϕ is found by integrating the relationship between the precession rate and the angular velocity components:

$$\dot{\phi} = \frac{1}{\sin\theta}\left(\omega_z \sin\psi - \omega_y \cos\psi\right) \tag{19}$$

After integration, the $\phi(t)$ expression is found:

$$\phi(t) = \frac{H}{I_x}(t - t_0) + \frac{H(I_x - I_z)}{n_\tau I_x I_z}\left[\Pi\left(\mathrm{am}(n_\tau t + \tau_0), -\frac{I_x(I_z - I_y)}{I_z(I_y - I_x)}, k^2\right) - \Pi\left(\mathrm{am}(\tau_0), -\frac{I_x(I_z - I_y)}{I_z(I_y - I_x)}, k^2\right)\right] \tag{20}$$

where k and n_τ are defined in Eq. (15), and τ_0 is found with Eq. (8) using Φ from Eq. (16). Again, it is recommended that the symmetric elliptic integrals be used to numerically evaluate Π [37, 38].

D. Initial Euler Angles

The Euler angles ϕ, θ, and ψ for both the SAM and LAM cases are computed from the body-frame angular momentum unit vector $\hat{h}$. The initial angles are found using similar expressions in both the SAM and LAM regimes, so they are discussed together. First, the initial nutation angle θ_0 is computed.

$$\theta_0 = \begin{cases} \cos^{-1}(h_x) & \text{if } I_d < I_y \\ \cos^{-1}(h_z) & \text{if } I_d > I_y \end{cases} \tag{21}$$

Recall that if $I_d = I_i$, the object is undergoing single-axis rotation about the axis $\hat{b}_i$ and attitude is propagated using Eq. (3). Next, the initial spin angle ψ_0 is found that satisfies the following relations:

$$\begin{cases} \sin\psi_0 = \dfrac{h_z}{\sqrt{h_y^2 + h_z^2}} \quad \cos\psi_0 = \dfrac{-h_y}{\sqrt{h_y^2 + h_z^2}} & \text{if } I_d < I_y \\ \sin\psi_0 = \dfrac{h_x}{\sqrt{h_x^2 + h_y^2}} \quad \cos\psi_0 = \dfrac{h_y}{\sqrt{h_x^2 + h_y^2}} & \text{if} I_d \geq I_y \end{cases} \tag{22}$$

Finally, the initial precession angle ϕ_0 is computed.

$$\phi_0 = 4\tan^{-1}\left(\frac{-\sqrt{(\cos\theta_0 + 1)(1 - \cos\psi_0)}}{A + \sqrt{2(\cos\theta_0 + 1)}}\right) \tag{23}$$

where

DISTRIBUTION A: Distribution approved for public release.

$$A = \begin{cases} \sqrt{(\cos\theta_0 + 1)(\cos\psi_0 + 1)} & \text{if } \sin\psi_0 \geq 0 \\ -\sqrt{(\cos\theta_0 + 1)(\cos\psi_0 + 1)} & \text{if } \sin\psi_0 < 0 \end{cases} \tag{24}$$

The expressions for the initial Euler angle values in Eq. (21), Eq. (22), and Eq. (23) are derived in the Appendix.

III. Attitude Inversion Method

The attitude inversion method used in this study is outlined in Fig. 1. The first "possible attitude" PSO finds attitudes that could correspond to the initial light curve measurements. The second "full state" PSO searches the space of initial attitudes and angular velocities to find an initial state corresponding to the light curve as a whole. This second PSO uses the possible attitudes found by the first as the starting point for its search. The estimated states that best fit the measurements are then refined using a quasi-Newton optimizer [39]. The only inputs required for the attitude inversion process are the light curve measurements, the problem geometry, and the observed object's shape and reflective properties. An initial state guess is not required because of how the PSOs search the solution space. The method makes no assumptions about the object's motion apart from it being approximately torque-free during the observation period.

A. Possible Attitude Particle Swarm Optimizer

1. Cost Function

The goal of the first, or "possible attitude," PSO is to identify possible attitudes of the object at the time of the first light curve measurement. The measured light curve is defined as a vector z of intensity measurements:

$$z = \begin{bmatrix} I_{m,0} & I_{m,1} & \dots & I_{m,N-1} & I_{m,N} \end{bmatrix} \tag{25}$$

where N is the number of measurements in the light curve and $I_{m,j}$ is the intensity measurement observed at time tji. The time t_j is referred to as the j-th measurement time or the j-th time step. As z is the measured light curve, it is a function of the true object attitude at each measurement time.

The fit of a particular attitude to the initial measurement is described using the cost function J_{att}:

$$J_{\text{att}} = \frac{I_{m,0} - I_L(\hat{\boldsymbol{q}})}{I_{m,0}} \tag{26}$$

where $I_{m,0}$ is the measured light curve intensity at the initial time step in Watts per meter squared, I_L is the simulated intensity for a given attitude, and $\hat{\boldsymbol{q}}$ is the estimated quaternion rotating from an approximately inertial space-fixed coordinate frame to a body-fixed frame in the object of interest.

DISTRIBUTION A: Distribution approved for public release.

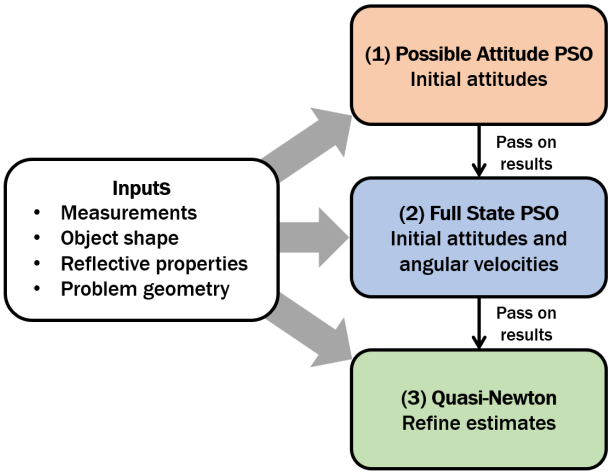

Fig. 1 A flowchart giving an overview of the attitude inversion process [27].

2. Initialization

The structure of the two PSOs used in this study is outlined in Fig. 2. First, the PSO is initialized with particles (yellow). Second, the particles are moved through the solution space for a set number of iterations (blue). Finally, the best state estimates found by each particle are output (gray).

The initialization phase of a PSO consists of four steps: first, the set of particles is created; second, the cost function at each particle's location is evaluated; third, each particle is assigned the neighbors it will communicate with during the optimization process; finally, the best solutions seen by each particle and its neighbors are stored.

For the possible attitude PSO, particles are created in a three-dimensional attitude space. Ultimately, this PSO outputs solutions in the form of unit quaternions $\hat{\boldsymbol{q}}_0$ [34]. However, quaternions are internally represented using four-dimensional spherical coordinates $\alpha, \beta, \gamma \in [-\pi, \pi]$ to allow the motion of particles in the solution space to be unconstrained. Spherical coordinates are used by the PSOs instead of the Euler angles described in Section II because the estimated initial attitude $\hat{\boldsymbol{q}}_0$ is distinct from the $\Delta\boldsymbol{q}$ term as seen in Eq. (2).

$$\hat{\boldsymbol{q}}_0 = \left(\sin\alpha \sin\beta \sin\gamma, \begin{bmatrix} \cos\alpha & \sin\alpha\cos\beta & \sin\alpha\sin\beta\cos\gamma \end{bmatrix}^T \right) \tag{27}$$

The particles are initialized as evenly spaced in attitude space with spherical coordinates $\hat{\boldsymbol{x}}_i = [\alpha_i \quad \beta_i \quad \gamma_i]^T$. Each particle is also assigned a random initial velocity $\boldsymbol{v}_i = [v_{i,\alpha} \quad v_{i,\beta} \quad v_{i,\gamma}]^T$ in the solution space. This step corresponds to Block (1) in Fig. 2.

The initialization process continues with the evaluation of the cost function J_{att} at each particle's location $\hat{\boldsymbol{x}}_i$. Each particle stores its current position and the corresponding cost as the best solution $\hat{\boldsymbol{x}}_{B,i}$ it has seen with cost $J_{B,i}$.

The PSO may also allow particles to communicate with each other. If this is the case, then in Block (3), each particle is assigned other particles as "neighbors," and the lowest-cost solution seen by each particle and its neighbors is stored

DISTRIBUTION A: Distribution approved for public release.

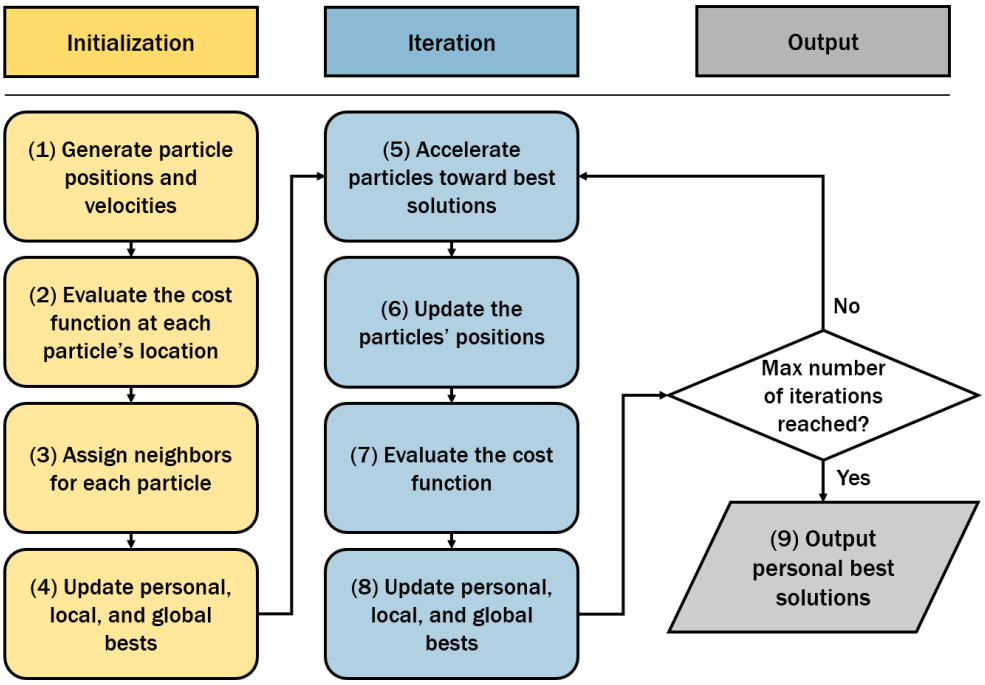

Fig. 2 A flowchart of the structure of the two PSOs used in the attitude inversion method.

as its local best $\hat{\boldsymbol{x}}_{l,i}$ with cost $J_{l,i}$. The best solution seen by any particle in the swarm may also be recorded as the globally best solution $\hat{\boldsymbol{x}}_g$ with cost J_g. Allowing particles to be informed by what other swarm members have seen makes it more likely that the swarm will converge on a global minimum rather than many local minima.

3. Iterations

After initializing the PSO, the particles are moved through solution space a set number of times to look for the minima of Jatt in Blocks (5) through (8) of the flowchart in Fig. 2. Before moving the particles, their velocities are updated based on the best solutions found so far. In Block (5), each particle is accelerated by a random amount according to the following expression:

$$\boldsymbol{v}_i^+ = \boldsymbol{v}_i^- + c_v \left[R_b(\hat{\boldsymbol{x}}_{B,i} - \hat{\boldsymbol{x}}_i) + w_l R_l(\hat{\boldsymbol{x}}_{l,i} - \hat{\boldsymbol{x}}_i) + w_g R_g(\hat{\boldsymbol{x}}_g - \hat{\boldsymbol{x}}_i) \right], \qquad R_x \sim U(0,1) \tag{28}$$

where $\boldsymbol{v}_i^{-/+}$ is the velocity of the i-th particle before and after the update, c_v is a positive constant, and the R_x terms are random numbers between 0 and 1. The non-negative weights w_l and w_g control how much importance is given to the local best and globally best solutions, respectively. The magnitude of $\boldsymbol{v}_i^+$ is capped at a set value $v_{\max}$.

For the possible attitude PSO, w_l and w_g are set to zero. These settings force each particle to consider only the best solutions it has personally encountered, meaning that the PSO will find a larger number of local minima than if the

DISTRIBUTION A: Distribution approved for public release.

particles communicated with each other. In many contexts, this would not be desirable behavior. However, the possible attitude PSO aims to locate as many attitudes as possible, so particles settling into many local minima is desirable in this context.

Once the particle velocities have been updated, the particles are moved through the solution space in Block (6) using the expression shown below:

$$\hat{\boldsymbol{x}}_i^+ = \hat{\boldsymbol{x}}_i^- + \boldsymbol{v}_i^+ \tag{29}$$

where $\hat{\boldsymbol{x}}_i^{-/+}$ is the position of the i-th particle before and after being updated.

Next, the cost function J_{att} is evaluated at each particle's new location in Block (7). The particles' personal and local best solutions and the swarm's global best solution are then updated in Block (8). If the PSO has run for the desired number of iterations, it outputs the personal best solutions $\hat{\boldsymbol{x}}_{i,B}$ found by each particle. If not, the PSO returns to Block (5), and the particles are accelerated and moved again per Eq. (28) and Eq. (29).

4. Motion in Angle Space

The definition of the attitude space representation in Eq. (27) constrained the spherical coordinates $\{\alpha, \beta, \gamma\}$ to be between $-\pi$ and π, but Eq. (29) allows unconstrained movement of the particles through solution space. Therefore, the periodic nature of $\hat{\boldsymbol{q}}(\alpha, \beta, \gamma)$ in Eq. (27) is leveraged to keep the particles within that range.

Let $\xi \in \{\alpha, \beta, \gamma\}$ be one of the spherical coordinates. The periodicity of the attitude representation means that changing ξ by $\pm 2\pi$ results in the same attitude representation. The addition and subtraction operations in Eq. (28) and Eq. (29) are therefore calculated as follows:

$$\xi_A \pm \xi_B = \begin{cases} \xi_A \pm \xi_B - 2\pi & \text{if } (\xi \pm \gamma) > \pi \\ \xi_A \pm \xi_B + 2\pi & \text{if } (\xi_A \pm \xi_B) < -\pi \\ \xi_A \pm \xi_B & \text{otherwise} \end{cases} \tag{30}$$

As a result of these operations, whenever a particle's location is updated, any spherical coordinates that would fall outside the allowed range are shifted by 2π so that they fall inside it.

B. Full State Particle Swarm Optimizer

1. State and Cost Function

Once a set of possible attitudes is found at the initial measurement time, a second "full state" PSO is used to find initial attitude and angular velocity states $\hat{\boldsymbol{y}}_i$ matching the measured light curve:

DISTRIBUTION A: Distribution approved for public release.

$$\hat{\boldsymbol{y}}_i \coloneqq \begin{bmatrix} \hat{\boldsymbol{x}}_i \\ \hat{\boldsymbol{\omega}}_i \end{bmatrix} \qquad \hat{\boldsymbol{x}}_i \coloneqq \begin{bmatrix} \alpha_i \\ \beta_i \\ \gamma_i \end{bmatrix} \qquad \boldsymbol{\omega}_i = \begin{bmatrix} \omega_{i,x} \\ \omega_{i,y} \\ \omega_{i,z} \end{bmatrix} \tag{31}$$

where α_i, β_i, and γ_i correspond to the same angles in Eq. (27), and $\omega_{i,x}$, $\omega_{i,y}$, and $\omega_{i,z}$ are the components of the object's estimated angular velocity $\hat{\boldsymbol{\omega}}_i$.

The cost function J_{LC} of the full state inversion PSO is based on how well a propagated light curve $\hat{\boldsymbol{z}}_i$ matches the measured light curve $\boldsymbol{z}$. This cost function is distinct from the possible attitude PSO cost function Eq. (26), which only compares the two light curves at the first time step.

$$J_{\text{LC}}(\hat{\boldsymbol{y}}_i) = c_{\text{sc}} \sum_{j=0}^{N-1} \left(I_{m,j} - I_L(\hat{\boldsymbol{q}}_j)\right)^2 = c_{\text{sc}} ||\boldsymbol{z} - \hat{\boldsymbol{z}}_i||^2 \tag{32}$$

where N is the number of measurements in the input light curve, $I_{m,j}$ is the measured light curve intensity at time t_j, and $\hat{\boldsymbol{q}}_j$ is the attitude at t_j found by propagating the initial state $\hat{\boldsymbol{y}}_i$ using Eq. (10), Eq. (11), and Eq. (13) for SAM rotations, or Eq. (17), Eq. (18), and Eq. (20) for LAM rotations. The constant c_{sc} is a scaling factor to compensate for numerical issues involving very small measurements.

Because the cost J_{LC} is not normalized, a nondimensionalized error E_{frac} is used to report how well a state estimate matches the light curve instead of the raw cost value. E_{frac} is the ratio between the magnitude of the difference between the estimate's light curve and the measured light curve, divided by the magnitude of the measurement vector.

$$E_{\text{frac}}(\hat{\boldsymbol{y}}_i) = \frac{\sqrt{J_{\text{LC}}}}{c_{\text{sc}}||\boldsymbol{z}||} = \frac{||\boldsymbol{z} - \hat{\boldsymbol{z}}_i||}{||\boldsymbol{z}||} \tag{33}$$

where J_{LC} is defined as in Eq. (32) and $\boldsymbol{z}$ is the vector of light curve measurements.

2. *Full State PSO Particle Creation*

The states $\hat{\boldsymbol{y}}_i$ in Eq. (31) are divided into two kinds: the initial attitude states $\hat{\boldsymbol{x}}_i$, and the initial angular velocity states $\hat{\boldsymbol{\omega}}_i$. When initializing the PSO, the attitude and angular velocity states are generated separately, and then a particle is initialized for each attitude-angular-velocity pairing.

The initial attitude states are the possible attitudes found using the possible attitude PSO, and the angular velocity states are selected with a maximum magnitude equal to the Nyquist frequency of the input light curve. These angular velocity states may be either randomly generated as in Burton and Frueh [24] or distributed approximately evenly within the sphere [28]. Assuming that the light curve measurements are Δt seconds apart, then this maximum magnitude is as

DISTRIBUTION A: Distribution approved for public release.

follows:

$$\omega_{\max} = \frac{\pi}{\Delta t} \text{ rad/s} \tag{34}$$

Once n initial attitudes $\hat{\boldsymbol{x}}_{(k)}$ and m initial angular velocities $\hat{\boldsymbol{\omega}}_{(k)}$ have been generated, they are combined to form the set of nm initial state guesses $\hat{\boldsymbol{y}}_i$ where

$$\{\hat{\boldsymbol{y}}_1, \hat{\boldsymbol{y}}_2, ..., \hat{\boldsymbol{y}}_m, \hat{\boldsymbol{y}}_{m+1}, ..., \hat{\boldsymbol{y}}_{nm}\} = \left\{ \begin{bmatrix} \hat{\boldsymbol{x}}_{(1)} \\ \hat{\boldsymbol{\omega}}_{(1)} \end{bmatrix}, \begin{bmatrix} \hat{\boldsymbol{x}}_{(1)} \\ \hat{\boldsymbol{\omega}}_{(2)} \end{bmatrix}, ..., \begin{bmatrix} \hat{\boldsymbol{x}}_{(1)} \\ \hat{\boldsymbol{\omega}}_{(m)} \end{bmatrix}, \begin{bmatrix} \hat{\boldsymbol{x}}_{(2)} \\ \hat{\boldsymbol{\omega}}_{(1)} \end{bmatrix}, ..., \begin{bmatrix} \hat{\boldsymbol{x}}_{(n)} \\ \hat{\boldsymbol{\omega}}_{(m)} \end{bmatrix} \right\} \tag{35}$$

The initial velocities of the particles are then randomly generated. The velocities of each particle in the attitude state space $\boldsymbol{v}_{i,x}$ and angular velocity state space $\boldsymbol{v}_{i,\omega}$ are generated and updated separately.

For the full state PSO, the local weight w_l and global weight w_g in Eq. (28) are not necessarily set to zero. Therefore, particles are assigned neighbors at initialization, which are used to obtain the $\hat{\boldsymbol{x}}_{l,i}$ solutions. Each particle's neighbors are the n_l particles with the same initial attitude estimate $\hat{\boldsymbol{x}}_i$ and the angular velocities closest to $\hat{\boldsymbol{\omega}}_i$.

3. Motion in the Solution Spaces

After initialization, the full state PSO is run as described in Section III.A.3. However, because the attitude and angular velocity estimate spaces have different properties, the state components $\hat{\boldsymbol{x}}_i$ and $\hat{\boldsymbol{\omega}}_i$ are updated separately.

The spherical coordinates representing the attitude quaternion are bounded on $[-\pi, \pi]$ just as for the possible attitude PSO. Therefore, the differences between a particle's attitude estimate $\hat{\boldsymbol{x}}_i$ and its the best solutions $\hat{\boldsymbol{x}}_{B/l/g,i}$ are calculated using Eq. (30). The position of a particle in attitude space is also updated according to Eq. (30) to ensure the spherical coordinates stay in the allowed range.

The angular velocity space is treated as a Cartesian space and updated using Eq. (28) and Eq. (29). Any particles whose angular velocity estimate magnitude exceeds $\omega_{\max}$ from Eq. (34) have their velocities $\boldsymbol{v}_{i,\omega}$ reversed and are moved so that they lie on the sphere with radius $\omega_{\max}$.

Note that the attitude and angular velocity estimates may use different maximum velocities v_{max} and acceleration constants c_v when updating a particle's velocity in their respective spaces using Eq. (28).

IV. The Flip Problem

Symmetries in the propagation of light [40, 41] significantly impact the results found by any attitude inversion method. The quantity $I_m(\hat{u}, \hat{s})$ is defined as the light measured from a uniform surface by an observer in the direction $\hat{u}$ given a light source in the direction $\hat{s}$. The same amount of light will be seen if the light source and observer directions are swapped. In mathematical form:

DISTRIBUTION A: Distribution approved for public release.

$$I_m(\hat{u}, \hat{s}) = I_m(\hat{s}, \hat{u}) \tag{36}$$

It will be demonstrated below that there are always at least two attitude time histories that produce the same vector of measurements z, assuming the problem geometry does not change.

At the j-th time step, if the inertial-frame $\hat{u}$ and $\hat{s}$ vectors do not change over the observation window, then the body-frame unit vectors can be found as follows:

$$\begin{aligned} (0, \underset{b}{\hat{u}_j}) &= \Delta\boldsymbol{q}_j \otimes \boldsymbol{q}_0 \otimes (0, \underset{e}{\hat{u}}) \\ (0, \underset{b}{\hat{s}_j}) &= \Delta\boldsymbol{q}_j \otimes \boldsymbol{q}_0 \otimes (0, \underset{e}{\hat{s}}) \end{aligned} \tag{37}$$

where b indicates a vector written in the body frame, and e indicates a vector written in the space-fixed inertial frame. $\Delta\boldsymbol{q}_j = \Delta\boldsymbol{q}\text{SAM/LAM}(\phi_j, \theta_j, \psi_j)$ as defined in Eq. (4) and Eq. (5) for the Euler angles ϕ_j, θ_j, and ψ_j. As shown in Section II, the values of the Euler angles depend only on time t and the initial angular momentum of the object.

A new quaternion $\boldsymbol{q}_{\text{flip}}$ is defined that rotates 180° about the bisector of $\hat{u}$ and $\hat{s}$.

$$\boldsymbol{q}_{\text{flip}} = \left(0, \frac{\hat{u} + \hat{s}}{2}\right) \tag{38}$$

From Eq. (38), it follows that:

$$\begin{aligned} (0, \underset{e}{\hat{u}_{\text{flip}}}) &= \boldsymbol{q}_{\text{flip}} \otimes (0, \underset{e}{\hat{u}}) = (0, \underset{e}{\hat{s}}) \\ (0, \underset{e}{\hat{s}_{\text{flip}}}) &= \boldsymbol{q}_{\text{flip}} \otimes (0, \underset{e}{\hat{s}}) = (0, \underset{e}{\hat{u}}) \end{aligned} \tag{39}$$

where $\hat{u}_{\text{flip}}$ and $\hat{s}_{\text{flip}}$ indicate the vectors after the rotation. Based on Eq. (37), the values of $\hat{u}_{flip}$ and $\hat{s}_{flip}$ at the j-th time step are as follows:

$$\begin{aligned} (0, \underset{b}{\hat{u}_{j,\text{flip}}}) &= \Delta\boldsymbol{q}_j \otimes \boldsymbol{q}_0 \otimes (0, \underset{e}{\hat{u}_{\text{flip}}}) = \Delta\boldsymbol{q}_j \otimes \boldsymbol{q}_0 \otimes (0, \underset{e}{\hat{s}}) \\ (0, \underset{b}{\hat{s}_{j,\text{flip}}}) &= \Delta\boldsymbol{q}_j \otimes \boldsymbol{q}_0 \otimes (0, \underset{e}{\hat{s}_{\text{flip}}}) = \Delta\boldsymbol{q}_j \otimes \boldsymbol{q}_0 \otimes (0, \underset{e}{\hat{u}}) \end{aligned} \tag{40}$$

Because the initial Euler angle values ϕ_0, θ_0, and ψ_0 only depend on the initial angular momentum of the object, $\Delta\boldsymbol{q}(t_j)$ is not changed by the transformation. Therefore, at all time steps:

DISTRIBUTION A: Distribution approved for public release.

$$I_m(\hat{u}_{j,\text{flip}}, \hat{s}_{j,\text{flip}}) = I_m(\hat{s}_j, \hat{u}_j) = I_m(\hat{u}_j, \hat{s}_j) \tag{41}$$

The above demonstrates that rotating an object 180° about the bisector of the constant $\hat{u}$ and $\hat{s}$ will not change the set of measurements z.

As a result, for any set of brightness measurements collected over a period in which the space-fixed frame $\hat{u}$ and $\hat{s}$ vectors are approximately constant, there will always be a minimum of two attitude time histories that fit the measurements equally well: the truth and the "flipped" estimate. These results explain the attitude estimates 180° from the truth identified in previously published research on the PSO attitude inversion method [24]. As discussed in Section V, the truth may be distinguished from the "flipped" estimate by taking another set of measurements with a different problem geometry. In addition, to ensure that more of the solution space is searched when the best estimates from the full state PSO are refined, the "flipped" counterparts of the estimates are also refined. The "flipped" counterpart of an attitude estimate is found by rotating the attitude of the object using $\boldsymbol{q}_{\text{flip}}$ in Eq. (38).

V. Results

The PSO attitude inversion method is demonstrated by estimating the attitude of space objects using noiseless simulated light curves. Each light curve consists of 25 simulated measurements taken over 40 seconds, corresponding to a Nyquist frequency of 1.885 rad/s. For a set number of measurements, the Nyquist frequency is coupled to the observation window's length and puts a constraint on the maximum angular velocity that can be resolved.

The positions of the object, observer, and Sun are assumed to be perfectly known, along with the object's shape and reflective properties. For each case, the observed object is in a circular geostationary orbit over the 106° W line of longitude (semi-major axis 42,241 km, eccentricity 0, inclination 0). The measurements are taken by a ground-based observer at 106° W, 45° N. In each case, the object's total angular velocity magnitude is 1.5 rad/s, and a set of 769 angular velocities is used to initialize the full state PSO. These angular velocities are evenly spaced in a sphere with a radius equal to the Nyquist frequency.

In Case 1, a cylindrical object reflecting light purely diffusely is observed. In Case 2, a regular tetrahedron reflecting light according to a Cook-Torrance model is observed. Case 3 uses a model of the Landsat 8 satellite [42] instead of the regular tetrahedron. A second observer is also added that takes 25 additional measurements offset 2.2 seconds from the originals. The attitude time history of the Landsat 8 model is identical to that of the tetrahedron in Case 2. These differences are summarized in Table 1.

The light curve measurements are simulated in different ways for the three objects. For the regular cylinder, the light reflecting off of each surface is calculated directly using a Lambertian reflection model [18]. Since the reflection model assumes that the object is made of flat facets, the cylinder's curved sides are approximated as being made up of 32

DISTRIBUTION A: Distribution approved for public release.

Table 1 A summary of the setup for each test case.

Case	Object Model	Observers	Light Curves	Offset	Total Measurements
1	Cylinder	1	1	—	25
2	Tetrahedron	1	2	—	25
3	Landsat 8	2	2	2.2 sec	50

rectangular faces. For the tetrahedron, a Cook-Torrance reflection model [43] with a diffuse reflection coefficient of 0.8 and specular coefficient of 0.2 is used for all surfaces. The same reflection model is used for the Landsat 8 model. In order to model reflections quickly for the more complex satellite, however, the measurements used in Case 4 are generated using a neural network model [44] trained using high-fidelity simulated measurements [18].

These results and most of the accompanying discussion were originally published in Burton et al. [28].

A. Case 1: Spinning GEO Cylinder with One Observer

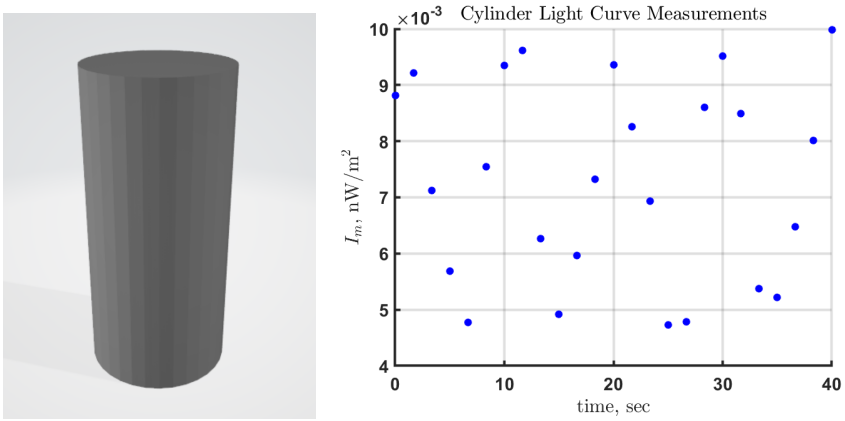

a) Model used for reflections. **b) The simulated light curve measurements.**

Fig. 3 The cylinder model and measurements for the Case 1 object [28].

The light curve analyzed in Case 1 is produced by a diffusely-reflecting cylinder [18] that is meant to approximate a formerly spin-stabilized rocket upper stage. The cylinder has a radius of 2.7 m and a height of 11.7 m [45]. The cylinder's moments of inertia are calculated by assuming a 2000 kg mass that is evenly distributed through the cylinder's volume: $I_{x,\text{cyl}} = I_{y,\text{cyl}} = 26.460 \cdot 10^3$ kg $\cdot$ m^2, $I_{z,\text{cyl}} = 7.290 \cdot 10^3$ kg $\cdot$ m^2.

The cylinder is shown in Fig. 3a, and as discussed above, the sides are made up of 32 rectangular faces for the purposes of simulating reflections. The cylinder's surfaces all have a diffuse reflection coefficient of 0.8.

The initial attitude of the cylinder is chosen such that its axis of symmetry is 30° from the inertial z-axis, and the angular velocity ω_0 is primarily along the body-fixed z-axis to imitate a formerly spin-stabilized upper stage.

DISTRIBUTION A: Distribution approved for public release.

$$\begin{aligned} \boldsymbol{q}_0 &= \left(0.2588, \begin{bmatrix} 0 & 0 & 0.9659 \end{bmatrix}^T\right) \\ \boldsymbol{\omega}_0 &= \begin{bmatrix} 0.2000 & 0.2000 & 1.4731 \end{bmatrix}^T \text{ rad/s} \end{aligned} \tag{42}$$

The observed light curve is shown in Fig. 3b. Using these input measurements, the possible attitude PSO finds 114 possible initial attitudes after running for ten iterations with 1,728 particles. The full state PSO is initialized using these possible attitudes, resulting in 87,666 particles. After running for 50 iterations, the best 250 solutions output by the full state PSO and their "flipped" counterparts are refined using the quasi-Newton method.

The five estimates which best fit the input measurements are shown in Table 2. The error E_{frac} in the estimated light curves is defined as in Eq. (33), and the average errors in the estimated direction of the axis of symmetry and angular velocity are calculated using the difference between the true and estimated object state at each measurement time. Only the error in the estimated direction of the cylinder's axis is reported because rotations about the axis of a completely symmetric cylinder would not affect the observed brightness I_m. The bold Rank 1 estimate is the one that best fits the input measurements and is, therefore, most likely to be the actual object state, according to the estimator.

The best-fitting estimates for the cylinder case are either less than one arcsec from the true axis direction on average or 180° away from it. Note that these cases with 180° of axis direction error are not true "flipped" estimates as discussed in Section IV because of their large angular velocity error. Truly "flipped" estimates are generated by changing an observed object's attitude while keeping its angular velocity fixed in the body frame. The high angular velocity error observed in, for example, the Rank 2 estimate indicates that the attitude error results from symmetries in the observed object. Given the highly symmetric nature of the cylindrical object, it is inevitable that symmetries would also appear in the attitude time history estimates. Nonetheless, the PSO attitude estimator is able to identify the true attitude time history as among those that fit the measurements well, even without any initial information about the object's attitude and rotation.

Table 2 Errors in the Case 1 cylinder axis pointing direction and angular velocity estimates [28].

		Initial Estimate Error		Average Estimate Error	
Rank	E_{frac}	Axis [deg]	Ang. Vel. [rad/s]	Axis [deg]	Ang. Vel. [rad/s]
1	$\mathbf{1.345 \cdot 10^{-7}}$	$\mathbf{2.185 \cdot 10^{-5}}$	$\mathbf{6.623 \cdot 10^{-8}}$	$\mathbf{2.514 \cdot 10^{-5}}$	$\mathbf{1.355 \cdot 10^{-7}}$
2	$1.599 \cdot 10^{-7}$	180.000	2.973	180.000	2.974
3	$1.745 \cdot 10^{-7}$	$7.167 \cdot 10^{-5}$	$4.531 \cdot 10^{-7}$	$6.712 \cdot 10^{-5}$	$3.271 \cdot 10^{-7}$
4	$2.016 \cdot 10^{-7}$	180.000	2.973	180.000	2.974
5	$3.726 \cdot 10^{-7}$	180.000	2.973	180.000	2.974

DISTRIBUTION A: Distribution approved for public release.

B. Case 2: GEO Uniformly-Reflecting Regular Tetrahedron

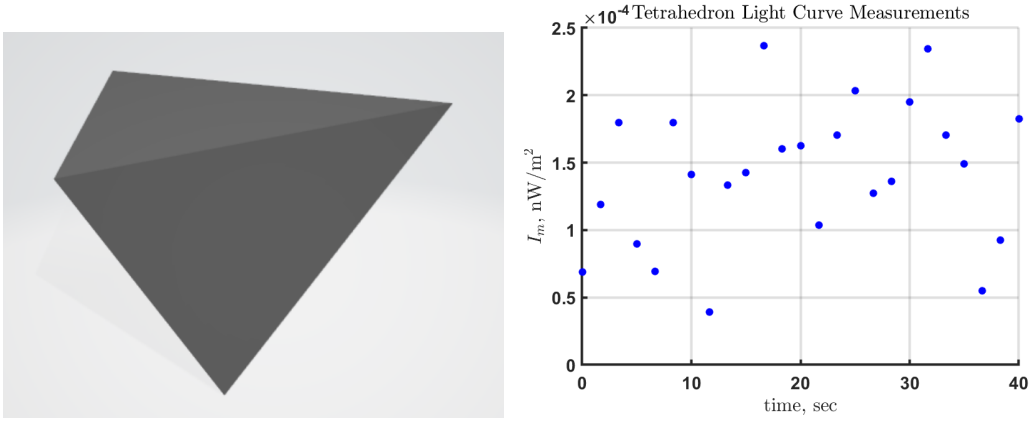

a) The regular tetrahedron. **b) The observed light curve.**

Fig. 4 The Case 2 observed object (a) and measured light curve (b) [28].

The second test case involves a uniformly-reflecting regular tetrahedron with side lengths of 1.63 m, shown in Fig. 4a. The observed brightness is simulated using a Cook-Torrance reflection model [43] with a 0.8 diffuse reflection coefficient and a 0.2 specular reflection coefficient for each surface. The mass of the tetrahedron is not evenly distributed, and it has the following moments of inertia: $I_{x,\text{tet}} = 1.0$ kg $\cdot$ m^2, $I_{y,\text{tet}} = 1.5$ kg $\cdot$ m^2, $I_{z,\text{tet}} = 2.0$ kg $\cdot$ m^2.

The initial state of the tetrahedron is randomly generated with the magnitude of the angular velocity vector set to 1.5 rad/s.

$$\begin{aligned} \boldsymbol{q}_0 &= \left(0.1005, \begin{bmatrix} 0.3015 & 0.5025 & 0.8040 \end{bmatrix}^T\right) \\ \boldsymbol{\omega}_0 &= \begin{bmatrix} 0.8566 & -1.1271 & 0.4959 \end{bmatrix}^T \text{ rad/s} \end{aligned} \tag{43}$$

The possible attitude PSO finds 111 attitudes after running for ten iterations with 32,768 particles. The full state PSO generates 85,359 particles by pairing the attitudes with the sampled angular velocity guesses. After 50 iterations, the 250 best-fitting attitude estimates are refined by the quasi-Newton method. Table 3 shows the best of these automatically refined estimates. For Cases 2 and 3, the total difference between the true and estimated attitudes is reported.

The Rank 1 through 3 estimates are all approximately equal to the true attitude time history. The Rank 1 estimate has a mean attitude error of only 0.6 arcsec and a mean angular velocity error of $2.708 \cdot 10^{-6}$ rad/s. This low level of error indicates that an asymmetric moment of inertia is sufficient for the true attitude of the object to be observable, even if, visually, it is completely symmetric. The estimated light curve and its normalized errors at each measurement time are shown in Fig. 5. The errors in Fig. 5b are normalized using the magnitude of the observed measurement vector $||z||$. The error in the estimated light curve at each measurement time is at most $1.25 \cdot 10^{-6}$, for a total E_{frac} of $1.453 \cdot 10^{-6}$.

DISTRIBUTION A: Distribution approved for public release.

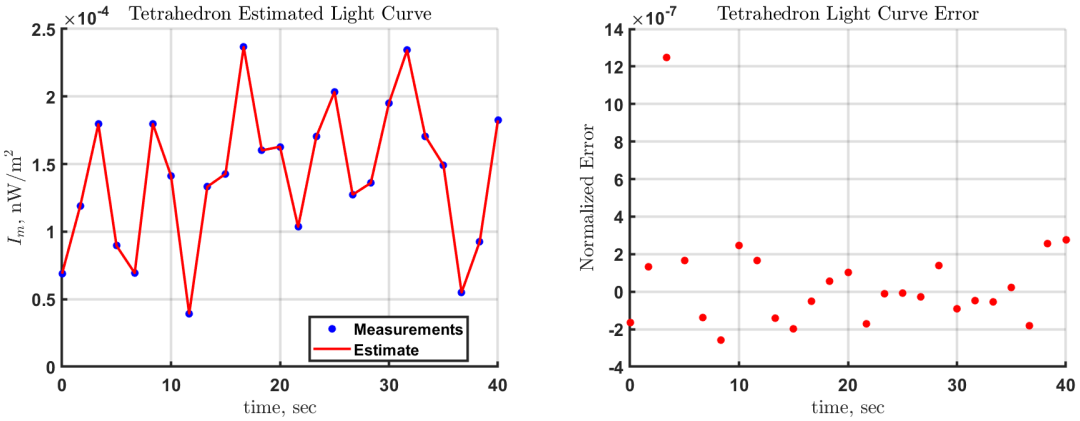

a) The estimated light curve. **b) The estimate's normalized error.**

Fig. 5 The best estimated light curve and its normalized error at each measurement time for Case 2 [28].

The Rank 4 and 5 estimates are an average of 108.535° away from the true attitude time history and have an average angular velocity error of 2.803 rad/s. These attitude time histories have an E_{frac} of approximately $1.9 \cdot 10^{-4}$ and likely fit the measurements so well because of the symmetries in the object shape. However, their E_{frac} value is two orders of magnitude higher than the Rank 1 estimate, meaning that the accurate attitude estimates are still identifiable for noiseless measurements.

The Rank 6 through 11 estimates are approximations of the "flipped" attitude time history discussed in Section IV. Note that a completely "flipped" attitude time history for this light curve would have an E_{frac} of $1.8 \cdot 10^{-3}$, higher than any of the estimates listed in Table 3. The Rank 6 through 11 estimates are "nearly-flipped" attitude time histories with a lower E_{frac}. However, as was the case for the Rank 4 and 5 estimates, these E_{frac} values are orders of magnitude higher than the accurate attitude estimate's E_{frac}, meaning that the two can be distinguished.

Table 3 Errors in the Case 2 tetrahedron attitude and angular velocity estimates [28].

		Initial Estimate Error		Average Estimate Error	
Rank	E_{frac}	Attitude [deg]	Ang. Vel. [rad/s]	Attitude [deg]	Ang. Vel. [rad/s]
1	$\mathbf{1.453 \cdot 10^{-6}}$	$\mathbf{1.391 \cdot 10^{-4}}$	$\mathbf{5.737 \cdot 10^{-6}}$	$\mathbf{1.666 \cdot 10^{-4}}$	$\mathbf{2.708 \cdot 10^{-6}}$
⋮					
4	$1.915 \cdot 10^{-4}$	67.328	2.831	108.535	2.803
5	$1.942 \cdot 10^{-4}$	67.329	2.831	108.535	2.803
6	$4.401 \cdot 10^{-4}$	179.973	$8.784 \cdot 10^{-4}$	179.932	$7.475 \cdot 10^{-4}$

C. Case 3: Full Satellite Model

The third test case involves the same attitude profile and problem geometry as Case 2, but the observed object's shape is changed to that of the Landsat 8 satellite [42] as shown in Fig. 6a. This test case aims to examine the effect of

DISTRIBUTION A: Distribution approved for public release.

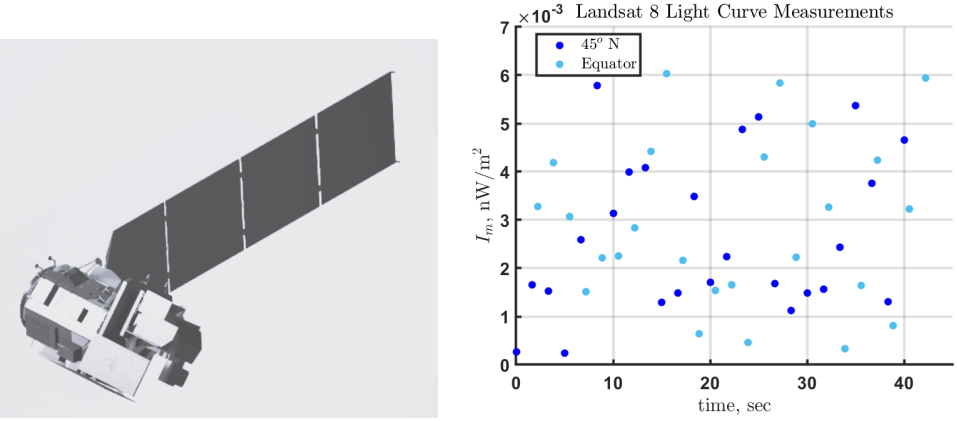

a) The Landsat 8 model. **b) The observed light curves.**

Fig. 6 The Landsat 8 object model and two-observer light curve for Case 3 [28, 42].

an object's shape and reflection model on the attitude estimate. Hence, the new object retains the same initial conditions as in Eq. (43).

As in Case 2, the model reflects light according to a Cook-Torrance model [43] with a 0.8 diffuse reflection coefficient and 0.2 specular reflection coefficient on each surface. However, because the shape of the Landsat 8 model is so complex, accurately simulating reflections for the millions of measurements simulated by the PSOs is extremely computationally intensive. Therefore, the reflections are approximated using a neural network trained on high-quality simulated reflections to reduce computation time. This neural network is used to produce both the observed measurements z and the estimated measurements $\hat{z}$.

Using an approximation for the reflection model results in decreased estimate accuracy, even though the same model is used both to compute the measurements and by the estimator. If only a single observer is used to find the attitude estimate, then the attitude estimate that best fits the measured light curves has an E_{frac} of 0.02746 with an average attitude error of 5.6°. In addition, the second best fitting attitude estimate is "flipped" relative to the true attitude with an E_{frac} of 0.03073, only slightly higher than the best attitude estimate. These results indicate that a single observer may have difficulty distinguishing between accurate and "flipped" attitude estimates for the Landsat 8 model.

This increased estimate error caused by the reflection approximations can be compensated for by using multiple observers to increase the attitude's observability. Case 3 uses two near-simultaneous light curves measured by two observers to find the attitude estimate of the Landsat 8 model. The first light curve is measured by an observer at 45° N latitude, as in the previous two test cases. The second light curve is offset by 2.2 seconds relative to the first and is measured from a point directly south of the first observer on the equator.

The possible attitude PSO is run for 100 iterations using 314,432 particles and finds 129 initial attitudes. These initial attitudes are then given to the full state PSO. The second PSO is run for 50 iterations, and the 250 best state estimates and their "flipped" counterparts are refined using the quasi-Newton method.

DISTRIBUTION A: Distribution approved for public release.

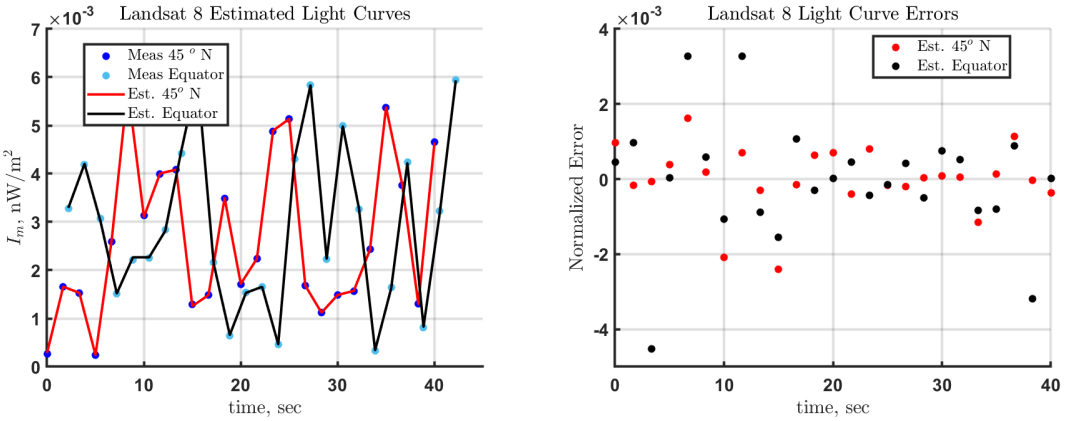

a) The estimated light curves seen by each observer. **b) The estimates' normalized errors.**

Fig. 7 The best estimated light curves and their normalized errors at each measurement time for Case 3 [28].

The five estimates that best fit the input light curves are shown in Table 4. The Rank 1 estimate has an E_{frac} of only $6.538 \cdot 10^{-3}$ and an average attitude error of 0.7954°. The light curves corresponding to the Rank 1 estimate, as seen by the two observers, are shown in Fig. 7. From the plot of measurement errors in Fig. 7b, the largest normalized error in any single estimated measurement is $4.532 \cdot 10^{-3}$.

Table 4 Errors in the Case 3 Landsat 8 attitude and angular velocity estimates [28].

		Initial Estimate Error		Average Estimate Error	
Rank	E_{frac}	Attitude [deg]	Ang. Vel. [rad/s]	Attitude [deg]	Ang. Vel. [rad/s]
1	$\mathbf{6.538 \cdot 10^{-3}}$	**0.9811**	**0.01184**	**0.7954**	$\mathbf{5.928 \cdot 10^{-3}}$
2	0.03422	5.157	0.02409	2.734	0.01598
3	0.04290	4.157	0.05430	3.451	0.02420
4	0.04648	5.900	0.08572	9.306	0.04874
5	0.04904	4.305	0.1066	3.499	0.04682

The Rank 2 through 5 estimates all have an average attitude error that ranges between 2.734° and 9.306°. These estimates also have low errors in their angular velocity estimates, never exceeding an average error of 0.04874 rad/s out of a true angular velocity magnitude of 1.5 rad/s.

Unlike the single-observer attitude estimates, the two-observer estimates reported in Table 4 do not include any "flipped" attitude time histories. "Flipped" attitude time histories are not present because they cannot simultaneously fit light curves measured by multiple observers. Therefore, having multiple observers may be useful when estimating attitude using real measurements whose noise might otherwise make it difficult to distinguish accurate attitude estimates from "flipped" ones.

Further testing also shows that the accuracy and consistency of the attitude estimator varies depending on the observed object's initial attitude and angular velocity. Therefore, additional work must be done to tune the estimator

DISTRIBUTION A: Distribution approved for public release.

properly for cases involving approximated measurements. Since more accurate estimates are correlated with lower E_{frac} values, such tuning can be done using only the light curve measurements, even if the true state of the object is unknown.

VI. Conclusions

Artificial space objects may have stable or tumbling attitude profiles and cannot be assumed to rotate at a constant rate about one axis. Similarly, when performing a light curve inversion, there is not always an *a priori* information about an observed object's attitude state. The particle swarm optimizer (PSO) inversion method addresses these difficulties by estimating an object's attitude and angular velocity using only its light curve without needing any *a priori* information about the object's rotation or an initial guess for its state. Arbitrary torque-free attitude motion can be quickly simulated using analytic expressions for attitude. The PSO inversion method only assumes that the problem geometry and the object's shape and reflective properties are known. Using PSOs to search the space of possible attitude and angular velocity states allows the method to account for the ambiguity of the estimation problem.

The results of the inversion process are shown for three test cases using noiseless simulated measurements. In the first test case, the direction of the axis of a rotating cylinder in a geosynchronous equatorial orbit is accurately estimated using 25 simulated measurements. However, due to symmetries in the object, other attitude profiles fit the light curve almost as well.

The correct attitude time history is found for a visually symmetric regular tetrahedron in the second test case. The solver can identify the attitude time histories closest to the truth because of the asymmetries in the tetrahedron's moments of inertia.

The third test case applies the attitude inversion process to a more complex Landsat 8 satellite model using near-simultaneous measurements from two observers at different locations. A neural network approximates a Cook-Torrance reflection model, making the attitude estimation process computationally tractable. The best estimate found by the PSO method for the Landsat 8 model has an average attitude error of less than 1°. This performance is not consistent for all initial states, however. Additional tuning of the solver or a more robust reflection approximation method may improve the consistency of the attitude estimate for complex non-convex shapes.

Appendix

The expressions for $\Delta\boldsymbol{q}_{\text{SAM}}$ and $\Delta\boldsymbol{q}_{\text{LAM}}$ in Eq. (4) and Eq. (5) are derived. First, the quaternions $\boldsymbol{q}_{313}$ and $\boldsymbol{q}_{131}$ relating Euler angles to a quaternion are derived, then the quaternions are used to describe the attitude of the rotating object. Finally, the initial Euler angle expressions Eq. (21), Eq. (22), and Eq. (23) are derived.

A. 313 Sequence Quaternion

The rotation corresponding to a 313 (ϕ, θ, ψ) Euler angle sequence is written in quaternion form as follows:

DISTRIBUTION A: Distribution approved for public release.

$$\boldsymbol{q}_{313} = (s_{313}, \boldsymbol{v}_{313}) = \boldsymbol{q}_3(\psi) \otimes \boldsymbol{q}_1(\theta) \otimes \boldsymbol{q}_3(\phi) \tag{44}$$

where $\boldsymbol{q}_1(\xi)$ or $\boldsymbol{q}_3(\xi)$ represents rotation about a single axis by an angle ξ.

$$\boldsymbol{q}_1(\xi) = \left(\cos\frac{\xi}{2}, \begin{bmatrix}\sin\frac{\xi}{2} & 0 & 0\end{bmatrix}^T\right) \qquad \boldsymbol{q}_3(\xi) = \left(\cos\frac{\xi}{2}, \begin{bmatrix}0 & 0 & \sin\frac{\xi}{2}\end{bmatrix}^T\right) \tag{45}$$

The quaternion multiplication $\otimes$ is defined as follows [46]:

$$\begin{aligned} \boldsymbol{q}_C &= (s_C, \boldsymbol{v}_C) = \boldsymbol{q}_A \otimes \boldsymbol{q}_B = (s_A, \boldsymbol{v}_A) \otimes (s_B, \boldsymbol{v}_B) \\ s_C &= s_A s_B - \boldsymbol{v}_A \cdot \boldsymbol{v}_B \\ \boldsymbol{v}_C &= s_A \boldsymbol{v}_B + s_B \boldsymbol{v}_B - \boldsymbol{v}_A \times \boldsymbol{v}_B \end{aligned} \tag{46}$$

Multiplying the three quaternions in Eq. (44) results in the following expression for $\boldsymbol{q}_{313}$:

$$\boldsymbol{q}_{313}(\phi,\theta,\psi) = \boldsymbol{q}_3(\psi) \otimes \boldsymbol{q}_{313}(\phi,\theta) = \left(\cos\frac{\phi}{2}\cos\frac{\theta}{2}\cos\frac{\psi}{2} - \sin\frac{\phi}{2}\cos\frac{\theta}{2}\sin\frac{\psi}{2}, \begin{bmatrix}\cos\frac{\phi}{2}\sin\frac{\theta}{2}\cos\frac{\psi}{2} + \sin\frac{\phi}{2}\sin\frac{\theta}{2}\sin\frac{\psi}{2} \\ \sin\frac{\phi}{2}\sin\frac{\theta}{2}\cos\frac{\psi}{2} - \cos\frac{\phi}{2}\sin\frac{\theta}{2}\sin\frac{\psi}{2} \\ \cos\frac{\phi}{2}\cos\frac{\theta}{2}\sin\frac{\psi}{2} + \sin\frac{\phi}{2}\cos\frac{\theta}{2}\cos\frac{\psi}{2}\end{bmatrix}\right) \tag{47}$$

The expression in Eq. (47) can be further simplified using the sum and difference trigonometric identities [47] to reach the form shown below:

$$\boldsymbol{q}_{313}(\phi,\theta,\psi) = \left(\cos\frac{\theta}{2}\cos\left(\frac{\phi+\psi}{2}\right), \begin{bmatrix}\sin\frac{\theta}{2}\cos\left(\frac{\phi-\psi}{2}\right) \\ \sin\frac{\theta}{2}\sin\left(\frac{\phi-\psi}{2}\right) \\ \cos\frac{\theta}{2}\sin\left(\frac{\phi+\psi}{2}\right)\end{bmatrix}\right) \tag{48}$$

B. 131 Sequence Quaternion

The quaternion $\boldsymbol{q}_{131}(\phi,\theta,\psi)$ corresponding to a 131 (ϕ,θ,ψ) Euler angle sequence is calculated in a similar way to the 313 sequence quaternion. The quaternion $\boldsymbol{q}_{131}(\phi,\theta,\psi)$ is equivalent to the following product:

$$\boldsymbol{q}_{131}(\phi,\theta,\psi) = \boldsymbol{q}_1(\psi) \otimes \boldsymbol{q}_3(\theta) \otimes \boldsymbol{q}_1(\phi) \tag{49}$$

DISTRIBUTION A: Distribution approved for public release.

where $\boldsymbol{q}_i(\xi)$ are defined as in Eq. (45) and $\otimes$ is defined as in Eq. (46). The product of the three quaternions is shown below:

$$\boldsymbol{q}_{131}(\phi,\theta,\psi) = \boldsymbol{q}_1(\psi)\otimes\boldsymbol{q}_{13}(\phi,\theta) = \left(\cos\frac{\phi}{2}\cos\frac{\theta}{2}\cos\frac{\psi}{2} - \sin\frac{\phi}{2}\cos\frac{\theta}{2}\sin\frac{\psi}{2}, \begin{bmatrix} \sin\frac{\phi}{2}\cos\frac{\theta}{2}\cos\frac{\psi}{2} + \cos\frac{\phi}{2}\cos\frac{\theta}{2}\sin\frac{\psi}{2} \\ \cos\frac{\phi}{2}\sin\frac{\theta}{2}\sin\frac{\psi}{2} - \sin\frac{\phi}{2}\sin\frac{\theta}{2}\cos\frac{\psi}{2} \\ \cos\frac{\phi}{2}\sin\frac{\theta}{2}\cos\frac{\psi}{2} + \sin\frac{\phi}{2}\sin\frac{\theta}{2}\sin\frac{\psi}{2} \end{bmatrix}\right) \tag{50}$$

Simplifying Eq. (50) with the sum and difference trigonometric identities results in the following expression:

$$\boldsymbol{q}_{131}(\phi,\theta,\psi) = \left(\cos\frac{\theta}{2}\cos\left(\frac{\phi+\psi}{2}\right), \begin{bmatrix} \cos\frac{\theta}{2}\sin\left(\frac{\phi+\psi}{2}\right) \\ -\sin\frac{\theta}{2}\sin\left(\frac{\phi-\psi}{2}\right) \\ \sin\frac{\theta}{2}\cos\left(\frac{\phi-\psi}{2}\right) \end{bmatrix}\right) \tag{51}$$

C. Short-Axis Mode Attitude Representation

In SAM rotation, the object is rotating principally about its short axis $\hat{b}_z$. Therefore, in a 313 (ϕ,θ,ψ) Euler angle sequence, the first angle ϕ is the precession angle of the object about the angular momentum unit vector $\hat{h}$, the second angle θ is the nutation angle between $\hat{h}$ and $\hat{b}_z$, and the third angle ψ is the spin angle about $\hat{b}_z$.

The attitude of an object undergoing SAM rotation can be represented by first making a rotation to align $\hat{b}_z$ with $\hat{h}$, then multiplying by $\boldsymbol{q}_{313}$.

$$\Delta\boldsymbol{q}_{\text{SAM}} = \left(\boldsymbol{q}_{313}(\phi,\theta,\psi)\otimes\boldsymbol{q}_{H,SAM}\right)^* \tag{52}$$

where $\boldsymbol{q}_{H,SAM}$ corresponds to a rotation that aligns $\hat{b}_z$ and $\hat{h}$. Since $\boldsymbol{q}_{313}$ and $\boldsymbol{q}_{H,SAM}$ rotate from the body-fixed frame to the inertial frame, their conjugate must be taken before they can be used to represent attitude with $\boldsymbol{q}_{\text{SAM}}$.

The quaternion $\boldsymbol{q}_{H,SAM}$ written is as follows:

$$\boldsymbol{q}_{H,SAM} = \left(\cos\frac{\theta_H}{2}, \sin\frac{\theta_H}{2}\frac{\hat{b}_z\times\hat{h}}{|\hat{b}_z\times\hat{h}|}\right) \tag{53}$$

where θ_H is the angle between $\hat{h}$ and $\hat{b}_z$. If, at the initial time, the angular momentum unit vector written using body-frame coordinates is equal to $\hat{h} = [h_x \quad h_y \quad h_z]^T$, then

$$\cos\theta_H = \hat{h}\cdot\hat{b}z = h_z \tag{54}$$

DISTRIBUTION A: Distribution approved for public release.

The scalar component of Eq. (53) is found using the cosine half-angle formula.

$$\cos\frac{\theta_H}{2} = \sqrt{\frac{\cos\theta_H + 1}{2}} = \sqrt{\frac{h_z + 1}{2}} \tag{55}$$

The factor $\sin\frac{\theta_H}{2}$ is found in a similar way.

$$\sin\frac{\theta_H}{2} = \sqrt{\frac{1 - \cos\theta_H}{2}} = \sqrt{\frac{1 - h_z}{2}} \tag{56}$$

The magnitude of the cross-product is

$$|\hat{b}_z \times \hat{h}| = \sqrt{h_x^2 + h_y^2} = \sqrt{1 - h_z^2} = \sqrt{(1 - h_z)(1 + h_z)} \tag{57}$$

Substituting Eq. (55) through Eq. (57) into Eq. (53) results in the final expression for $\boldsymbol{q}_{H,SAM}$ for SAM rotations:

$$\boldsymbol{q}_{H,SAM} = \left(\sqrt{\frac{h_z + 1}{2}}, \frac{1}{\sqrt{2(h_z + 1)}}\begin{bmatrix} -h_y & h_x & 0 \end{bmatrix}^T\right) \tag{58}$$

Multiplying $\boldsymbol{q}_{313}$ by $\boldsymbol{q}_{H,SAM}$ and taking the conjugate results in the following expression for attitude:

$$\begin{aligned}\Delta\boldsymbol{q}_{\text{SAM}}(\phi,\theta,\psi) = \frac{1}{\sqrt{2(h_z+1)}}\Bigg(&(h_z+1)\cos\frac{\theta}{2}\cos\left(\frac{\phi+\psi}{2}\right) + \sin\frac{\theta}{2}\left(h_y\cos\left(\frac{\phi-\psi}{2}\right) - h_x\sin\left(\frac{\phi-\psi}{2}\right)\right),\\ &\begin{bmatrix} -(h_z+1)\sin\frac{\theta}{2}\cos\left(\frac{\phi-\psi}{2}\right) - \cos\frac{\theta}{2}\left(x\sin\left(\frac{\phi+\psi}{2}\right) - h_y\cos\left(\frac{\phi+\psi}{2}\right)\right)\\ -(h_z+1)\sin\frac{\theta}{2}\sin\left(\frac{\phi-\psi}{2}\right) - \cos\frac{\theta}{2}\left(h_x\cos\left(\frac{\phi+\psi}{2}\right) + h_y\sin\left(\frac{\phi+\psi}{2}\right)\right)\\ -(h_z+1)\cos\frac{\theta}{2}\sin\left(\frac{\phi+\psi}{2}\right) + \sin\frac{\theta}{2}\left(h_x\cos\left(\frac{\phi-\psi}{2}\right) + h_y\sin\left(\frac{\phi-\psi}{2}\right)\right)\end{bmatrix}\Bigg)\end{aligned} \tag{59}$$

If the initial Euler angles are chosen such that Eq. (59) is equal to the identity quaternion $(1, \mathbf{0})$, then Eq. (59) represents the change in attitude from the initial time step, and the SAM attitude representation can be written as follows:

$$\boldsymbol{q}_{\text{SAM}} = \Delta\boldsymbol{q}_{\text{SAM}} \otimes \boldsymbol{q}_0 \tag{60}$$

where $\Delta\boldsymbol{q}_{\text{SAM}}$ is as in Eq. (4) and $\boldsymbol{q}_0$ is the attitude quaternion at the initial time step.

D. Long-Axis Mode Attitude Representation

The expression for LAM attitude change $\Delta\boldsymbol{q}_{\text{LAM}}$ is derived in a similar way to $\Delta\boldsymbol{q}_{\text{SAM}}$. For LAM motion, the three angles of a 131 (ϕ, θ, ψ) Euler angle sequence correspond to the precession ϕ, nutation θ, and spin ψ angles of an object relative to the $\hat{h}$ as it rotates primarily about the body-fixed $\hat{b}_x$ axis. The quaternion $\Delta\boldsymbol{q}_{\text{LAM}}$ is therefore equal to the

DISTRIBUTION A: Distribution approved for public release.

following:

$$\Delta \boldsymbol{q}_{\mathrm{LAM}} = \left(\boldsymbol{q}_{131}(\phi,\theta,\psi) \otimes \boldsymbol{q}_{H,LAM}\right)^{*} \tag{61}$$

where $\boldsymbol{q}_{H,LAM}$ represents a rotation aligning $\hat{b}_x$ with $\hat{h}$. It is found using a similar method to $\boldsymbol{q}_{H,SAM}$.

$$\boldsymbol{q}_{H,LAM} = \left(\sqrt{\frac{h_x+1}{2}}, \frac{1}{\sqrt{2(h_x+1)}}\begin{bmatrix} 0 & -h_z & h_y \end{bmatrix}^T\right) \tag{62}$$

Eq. (61) is then used to calculate $\Delta \boldsymbol{q}_{\mathrm{LAM}}$.

$$\Delta \boldsymbol{q}_{\mathrm{LAM}}(\phi,\theta,\psi) = \frac{1}{\sqrt{2(h_x+1)}}\left(\begin{array}{c}(h_x+1)\cos\frac{\theta}{2}\cos\left(\frac{\phi+\psi}{2}\right) - \sin\frac{\theta}{2}\left(h_z\sin\left(\frac{\phi-\psi}{2}\right) + h_y\cos\left(\frac{\phi-\psi}{2}\right)\right) \\ \begin{bmatrix} -(h_x+1)\cos\frac{\theta}{2}\sin\left(\frac{\phi+\psi}{2}\right) + \sin\frac{\theta}{2}\left(h_z\cos\left(\frac{\phi-\psi}{2}\right) - h_y\sin\left(\frac{\phi-\psi}{2}\right)\right) \\ (h_x+1)\sin\frac{\theta}{2}\sin\left(\frac{\phi-\psi}{2}\right) + \cos\frac{\theta}{2}\left(h_z\cos\left(\frac{\phi+\psi}{2}\right) - h_y\sin\left(\frac{\phi+\psi}{2}\right)\right) \\ -(h_x+1)\sin\frac{\theta}{2}\cos\left(\frac{\phi-\psi}{2}\right) - \cos\frac{\theta}{2}\left(h_y\cos\left(\frac{\phi+\psi}{2}\right) + h_z\sin\left(\frac{\phi+\psi}{2}\right)\right)\end{bmatrix}\end{array}\right) \tag{63}$$

Choosing the initial Euler angles such that Eq. (63) is equal to the identity quaternion $(1, \mathbf{0})$ at the initial time t_0, allows $\boldsymbol{q}_{\mathrm{LAM}}$ to be written as follows:

$$\boldsymbol{q}_{\mathrm{LAM}} = \Delta \boldsymbol{q}_{\mathrm{LAM}} \otimes \boldsymbol{q}_0 \tag{64}$$

where $\Delta \boldsymbol{q}_{\mathrm{LAM}}$ is equal to Eq. (5).

E. Short-Axis Mode Initial Euler Angles

At the initial time step, the Euler angles ϕ_0, θ_0, and ψ_0 are chosen such that $\Delta \boldsymbol{q}_{\mathrm{SAM}}(t_0) = (1, \mathbf{0})$. The initial nutation angle θ_0 and spin angle ψ_0 for SAM rotations are found using the angular momentum unit vector $\hat{h} = [h_x \quad h_y \quad h_z]^T$ written in the body-fixed frame. An object is undergoing SAM rotation if the dynamic moment of inertia I_d from Eq. (1) is greater than the intermediate moment of inertia I_y. The components of the unit vector $\hat{h}$ can be written in terms of the 313 Euler angles as follows:

$$h_x = \sin\theta_0 \sin\psi_0 \qquad h_y = \sin\theta_0 \cos\psi_0 \qquad h_z = \cos\theta_0 \tag{65}$$

From Eq. (65) it is obvious that the initial nutation angle θ_0 is equal to the following:

DISTRIBUTION A: Distribution approved for public release.

$$\theta_0 = \cos^{-1}(h_z) \tag{66}$$

The above expression is identical to Eq. (21) for $I_d > I_y$. The initial nutation angle θ_0 is always chosen such that $\theta_0 \in [0, \pi]$.

The initial value of the spin angle ψ_0 can also be found.

$$\psi_0 = \tan^{-1}\left(\frac{h_z/\sin\theta_0}{h_y/\sin\theta_0}\right) \tag{67}$$

This expression is equivalent to Eq. (22) for $I_d > I_y$.

Since the precession angle ϕ does not appear in Eq. (65), the initial precession angle ϕ_0 is found by setting $\Delta\boldsymbol{q}_{\text{SAM}} = (1, \mathbf{0})$. Since $\Delta\boldsymbol{q}_{\text{SAM}}$ is a unit quaternion, it will be sufficient to find a ϕ_0 that results in the scalar component of Eq. (4) equalling 1.

$$\frac{1}{\sqrt{2(h_z+1)}}\left\{(h_z+1)\cos\frac{\theta_0}{2}\cos\left(\frac{\phi_0+\psi_0}{2}\right) + \sin\frac{\theta_0}{2}\left[h_y\cos\left(\frac{\phi_0-\psi_0}{2}\right) - h_x\sin\left(\frac{\phi_0-\psi_0}{2}\right)\right]\right\} = 1 \tag{68}$$

The sine and cosine sum and difference formulas [47] are used to expand Eq. (68) so that ϕ_0 can be separated from the other Euler angles.

$$\begin{aligned}(h_z+1)\cos\frac{\theta_0}{2}\left(\cos\frac{\phi_0}{2}\cos\frac{\psi_0}{2} - \sin\frac{\phi_0}{2}\sin\frac{\psi_0}{2}\right) + \\ \sin\frac{\theta_0}{2}\left[h_y\left(\cos\frac{\phi_0}{2}\cos\frac{\psi_0}{2} + \sin\frac{\phi_0}{2}\sin\frac{\psi_0}{2}\right) - h_x\left(\sin\frac{\phi_0}{2}\cos\frac{\psi_0}{2} - \cos\frac{\phi_0}{2}\sin\frac{\psi_0}{2}\right)\right] = \sqrt{2(h_z+1)}\end{aligned} \tag{69}$$

After rearranging the terms, Eq. (69) is rewritten as an equation in the following form:

$$A\cos\frac{\phi_0}{2} + B\sin\frac{\phi_0}{2} = C \tag{70}$$

where A, B, and C are constants.

$$\begin{aligned}A &= (h_z+1)\cos\frac{\theta_0}{2}\cos\frac{\psi_0}{2} + \sin\frac{\theta_0}{2}\left(h_y\cos\frac{\psi_0}{2} + h_x\sin\frac{\psi_0}{2}\right) \\ B &= -(h_z+1)\cos\frac{\theta_0}{2}\sin\frac{\psi_0}{2} - \sin\frac{\theta_0}{2}\left(h_x\cos\frac{\psi_0}{2} - h_y\sin\frac{\psi_0}{2}\right) \\ C &= \sqrt{2(h_z+1)}\end{aligned} \tag{71}$$

The constants in Eq. (71) can be rewritten solely in terms of θ_0 and ψ_0 using the relations in Eq. (65).

DISTRIBUTION A: Distribution approved for public release.

$$
\begin{aligned}
A &= (\cos\theta_0 + 1)\cos\frac{\theta_0}{2}\cos\frac{\psi_0}{2} + \sin\theta_0 \sin\frac{\theta_0}{2}\left(\cos\psi_0\cos\frac{\psi_0}{2} + \sin\psi_0\sin\frac{\psi_0}{2}\right) \\
B &= -(\cos\theta_0 + 1)\cos\frac{\theta_0}{2}\sin\frac{\psi_0}{2} - \sin\theta_0\sin\frac{\theta_0}{2}\left(\sin\psi_0\cos\frac{\psi_0}{2} - \cos\psi_0\sin\frac{\psi_0}{2}\right) \\
C &= \sqrt{2(\cos\theta_0 + 1)}
\end{aligned}
\tag{72}
$$

The half angles in Eq. (72) can be further rewritten using the half-angle formulas [47].

$$
\cos\frac{\xi}{2} = \pm\sqrt{\frac{1+\cos\xi}{2}} \qquad\qquad \sin\frac{\xi}{2} = \pm\sqrt{\frac{1-\cos\xi}{2}} \tag{73}
$$

where ξ is some angle. Recalling that $\theta_0 \in [0, \pi]$ and $\psi_0 \in [0, 2\pi]$, it follows that $\cos(\theta_0/2)$, $\sin(\theta_0/2)$, and $\sin(\psi_0/2)$ are always positive, and $\cos(\psi_0/2)$ is negative everywhere that $\sin\psi_0$ is negative. By inspection of Eq. (72), it can be seen that A will be negative if $\sin\psi_0$ and $\cos(\psi_0/2)$ are negative. It can also be demonstrated that B is always negative, though the proof is omitted.

$$
\begin{aligned}
A &= \pm\left[(\cos\theta_0 + 1)\frac{\sqrt{(1+\cos\theta_0)(1+\cos\psi_0)}}{2} + \sin\theta_0\frac{\sqrt{1-\cos\theta_0}}{2}\left(\cos\psi_0\sqrt{1+\cos\psi_0} + |\sin\psi_0|\sqrt{1-\cos\psi_0}\right)\right] \\
B &= -\left[(\cos\theta_0 + 1)\frac{\sqrt{(1+\cos\theta_0)(1-\cos\psi_0)}}{2} + \sin\theta_0\frac{\sqrt{1-\cos\theta_0}}{2}\left(|\sin\psi_0|\sqrt{1+\cos\psi_0} - \cos\psi_0\sqrt{1-\cos\psi_0}\right)\right]
\end{aligned}
\tag{74}
$$

Simplified forms for A and B in Eq. (74) are derived by finding expressions for A^2 and B^2. After many simplifications, the following expressions are reached:

$$
A^2 = (\cos\theta_0 + 1)(\cos\psi_0 + 1) \qquad\qquad B^2 = (\cos\theta_0 + 1)(1 - \cos\psi_0) \tag{75}
$$

Note that the same forms are reached whether $\sin\psi_0$ is positive or negative. The constant A from Eq. (70) can now be written in the simplified form corresponding to Eq. (24). The simplified forms of both A and B are given below:

$$
A = \begin{cases} \sqrt{(\cos\theta_0 + 1)(\cos\psi_0 + 1)} & \text{if } \sin\psi_0 \geq 0 \\ -\sqrt{(\cos\theta_0 + 1)(\cos\psi_0 + 1)} & \text{if } \sin\psi_0 < 0 \end{cases} \qquad B = -\sqrt{(\cos\theta_0 + 1)(1 - \cos\psi_0)} \tag{76}
$$

DISTRIBUTION A: Distribution approved for public release.

The expression in Eq. (70) can now be used to find ϕ_0 by performing a Weierstrass substitution [48] to turn the equation into a quadratic polynomial.

$$\sin\frac{\phi_0}{2} = \frac{2r}{1+r^2} \qquad \cos\frac{\phi_0}{2} = \frac{1-r^2}{1+r^2} \qquad r = \tan\frac{\phi_0}{4} \tag{77}$$

After performing this substitution, it can be shown that Eq. (70) is equivalent to the following:

$$-(A+C)r^2 + 2Br + (A-C) = 0 \tag{78}$$

Since $A + C$ is never zero, then the roots of Eq. (78) can be found using the quadratic formula.

$$\tan\frac{\phi_0}{4} = r = \frac{B \mp \sqrt{A^2+B^2-C^2}}{A+C} \tag{79}$$

From Eq. (24), it is simple to show that $A^2 + B^2 - C^2 = 0$. Therefore, ϕ_0 can be written as follows:

$$\phi_0 = 4\tan^{-1}\left(\frac{B}{A+C}\right) \tag{80}$$

where the above expression is equivalent to Eq. (23).

F. Long-Axis Mode Initial Angles

The initial Euler angle values for long-axis mode (LAM) rotations are found in a similar way to the SAM initial angles. LAM rotation occurs when the dynamic moment of inertia I_d in Eq. (1) is less than the intermediate moment of inertia I_y. For LAM rotation, the initial body-frame angular moment unit vector $\hat{h} = [h_x \quad h_y \quad h_z]^T$ components are related to the nutation and spin angles as follows:

$$h_x = \cos\theta_0 \qquad h_y = -\sin\theta_0\cos\psi_0 \qquad h_z = \sin\theta_0\sin\psi_0 \tag{81}$$

The initial nutation angle θ_0 and spin angle ψ_0 can therefore be written as shown below:

$$\theta_0 = \cos^{-1}(h_x) \qquad \psi_0 = \tan^{-1}\left(\frac{h_z/\sin\theta_0}{-h_y/\sin\theta_0}\right) \tag{82}$$

The expressions in Eq. (82) are equivalent to Eq. (21) and Eq. (22) for $I_d < I_y$.

DISTRIBUTION A: Distribution approved for public release.

By setting the scalar component of $\Delta \boldsymbol{q}_{\mathrm{LAM}}$ in Eq. (63) equal to 1, it is found that the LAM initial precession angle ϕ_0 relates to the other initial Euler angles using the same relations as found for SAM rotations. The LAM equivalent to Eq. (70) is as follows:

$$D \cos \frac{\phi_0}{2} + E \sin \frac{\phi_0}{2} = F \tag{83}$$

where

$$\begin{aligned} D &= (\cos\theta_0 + 1)\cos\frac{\theta_0}{2}\cos\frac{\psi_0}{2} + \sin\theta_0 \sin\frac{\theta_0}{2}\left(\cos\psi_0\cos\frac{\psi_0}{2} + \sin\psi_0\sin\frac{\psi_0}{2}\right) \\ E &= -(\cos\theta_0 + 1)\cos\frac{\theta_0}{2}\sin\frac{\psi_0}{2} - \sin\theta_0\sin\frac{\theta_0}{2}\left(\sin\psi_0\cos\frac{\psi_0}{2} - \cos\psi_0\sin\frac{\psi_0}{2}\right) \\ F &= \sqrt{2(\cos\theta_0 + 1)} \end{aligned} \tag{84}$$

In Eq. (84), D, E, and F are all identical to the A, B, and C expressions in Eq. (72). Therefore, the initial precession angle ϕ_0 expressions in Eq. (23) and Eq. (24) are valid for both SAM and LAM rotations.

Funding Sources

This work was partly supported by the Air Force Office of Scientific Research through the grant AFOSR FA9950-19-1-0407 and by the European Space Agency.

References

[1] Russell, H. N., "On the Light-Variations of Asteroids and Satellites," *The Astrophysical Journal*, Vol. 24, No. 1, 1906, pp. 1–18.

[2] Williams, J., "The determination of the orientation of a tumbling cylinder from the shape of the light curve," *Office of Aerospace Research*, 1967, p. 31.

[3] Kaasalainen, M., Lamberg, L., Lumme, K., and Bowell, E., "Interpretation of lightcurves of atmosphereless bodies. I-General theory and new inversion schemes," *Astronomy and Astrophysics*, Vol. 259, 1992, pp. 318–332.

[4] Kaasalainen, M., and Torppa, J., "Optimization Methods for Asteroid Lightcurve Inversion: I. Shape Determination," *Icarus*, Vol. 153, No. 1, 2001, pp. 24–36. https://doi.org/https://doi.org/10.1006/icar.2001.6673, URL https://www.sciencedirect.com/science/article/pii/S0019103501966734.

[5] Kaasalainen, M., and Torppa, J., "Optimization methods for asteroid lightcurve inversion: I. shape determination," *Icarus*, Vol. 153, No. 1, 2001, pp. 24–36. https://doi.org/https://doi.org/10.1006/icar.2001.6673, URL https://www.sciencedirect.com/science/article/pii/S0019103501966734.

DISTRIBUTION A: Distribution approved for public release.

[6] Kaasalainen, M., Torppa, J., and Muinonen, K., "Optimization methods for asteroid lightcurve inversion: II. The complete inverse problem," *Icarus*, Vol. 153, No. 1, 2001, pp. 37–51. https://doi.org/https://doi.org/10.1006/icar.2001.6674, URL https://www.sciencedirect.com/science/article/pii/S0019103501966746.

[7] Ďurech, J., and Kaasalainen, M., "Photometric signatures of highly nonconvex and binary asteroids," *Astronomy & Astrophysics*, Vol. 404, No. 2, 2003, pp. 709–714. https://doi.org/10.1051/0004-6361:20030505.

[8] Hall, D., Africano, J., Archambeault, D., Birge, B., Witte, D., and Kervin, P., "Amos observations of nasa's image satellite," *The 2006 AMOS Technical Conference Proceedings*, 2006, pp. 10–14.

[9] Hall, D., Calef, B., Knox, K., Bolden, M., and Kervin, P., "Separating attitude and shape effects for non-resolved objects," *The 2007 AMOS Technical Conference Proceedings*, Maui Economic Development Board, Inc. Kihei, Maui, HI, 2007, pp. 464–475.

[10] Wetterer, C. J., and Jah, M., "Attitude determination from light curves," *Journal of Guidance, Control, and Dynamics*, Vol. 32, No. 5, 2009, pp. 1648–1651.

[11] Linares, R., Crassidis, J., and Jah, M., "Particle filtering light curve based attitude estimation for non-resolved space objects," *Advances in the Astronautical Sciences*, Vol. 152, 2014, pp. 119–130.

[12] Benson, C. J., Scheeres, D. J., Ryan, W. H., and Ryan, E. V., "Cyclic complex spin state evolution of defunct GEO satellites," *Proceedings of the Advanced Maui Optical and Space Surveillance Technologies Conference, Maui, HI*, 2018.

[13] Cabrera, D. V., Utzmann, J., and Förstner, R., "The adaptive Gaussian mixtures unscented Kalman filter for attitude determination using light curves," *Advances in Space Research*, Vol. 71, No. 6, 2023, pp. 2609–2628.

[14] Balster, P., Jones, G., Hofer, G., Newsom, D., and Frueh, C., "Object Characteristic Determination Using Brightness Measurements," *Proceedings of the Advanced Maui Optical and Space Surveillance (AMOS) Technologies Conference*, 2023, p. 72.

[15] Früh, C., and Jah, M. K., "Coupled orbit attitude motion of high area-to-mass ratio (HAMR) objects including efficient self-shadowing," *Acta Astronautica*, Vol. 95, 2014, pp. 227–241. https://doi.org/https://doi.org/10.1016/j.actaastro.2013.11.017.

[16] Fan, S., and Frueh, C., "A Direct Light Curve Inversion Scheme in the Presence of Measurement Noise," *The Journal of the Astronautical Sciences*, Vol. 67, 2019. https://doi.org/10.1007/s40295-019-00190-3.

[17] Burton, A., and Frueh, C., "Two Methods for Light Curve Inversion for Space Object Attitude Determination," *8th European Conference on Space Debris*, 2021.

[18] Robinson, L., and Frueh, C., "Light Curve Inversion for Reliable Shape Reconstruction of Human-Made Space Objects," *Proceedings of the 32nd AIAA/AAS Astrodynamics Specialist Conference*, 2022, pp. 1–19.

[19] Dianetti, A. D., "Resident Space Object Characterization Using Polarized and Multispectral Light Curves," Ph.D. thesis, State University of New York at Buffalo, 2020.

DISTRIBUTION A: Distribution approved for public release.

[20] Dianetti, A. D., and Crassidis, J. L., "Resident Space Object Characterization Using Polarized Light Curves," *Journal of Guidance, Control, and Dynamics*, Vol. 46, No. 2, 2023, pp. 246–263.

[21] Burton, A., and Frueh, C., "Light Curve Attitude Estimation using the Viewing Sphere," *Astrodynamics Specialist Conference 2020*, 2020.

[22] Clark, R., Dave, S., Wawrow, J., and Lee, R., "Performance of Parameterization Algorithms for Resident Space Object (RSO) Attitude Estimates," *Proceedings of the Advanced Maui Optical and Space Surveillance Technologies, Maui, HI, USA*, 2020, pp. 15–18.

[23] Gagnon, S. R., and Crassidis, J. L., "Augmenting Light Curve Based Attitude Estimation with Geometric Information," *AIAA SCITECH 2022 Forum*, 2022, p. 1767.

[24] Burton, A., and Frueh, C., "Fast Light Curve Inversion for All - Regular and Tumbling - Attitudes," *Advanced Maui Optical and Space Surveillance Technologies Conference 2023*, 2023.

[25] Clark, R., Fu, Y., Dave, S., and S K Lee, R., "Resident space object (RSO) attitude and optical property estimation from space-based light curves," *Advances in Space Research*, Vol. 70, No. 11, 2022, pp. 3271–3280. https://doi.org/https://doi.org/10.1016/j.asr.2022.08.068, URL https://www.sciencedirect.com/science/article/pii/S0273117722008043.

[26] Eberhart, R., and Kennedy, J., "A new optimizer using particle swarm theory," *MHS'95. Proceedings of the sixth international symposium on micro machine and human science*, Ieee, 1995, pp. 39–43.

[27] Burton, A., Robinson, L., and Frueh, C., "Attitude estimation from light curves using particle swarm optimizers," *The Second International Orbital Debris Conference*, 2023.

[28] Burton, A., Robinson, L., and Frueh, C., "Attitude Estimation Using Light Curves: A Particle Swarm Approach," *AIAA SciTech 2024 Forum*, 2024.

[29] Thomson, W., "Introduction to space dynamics." *Introduction to space dynamics.. WT Thomson. Dover Publications Inc*, 1986.

[30] Samarasinha, N. H., and A'Hearn, M. F., "Observational and dynamical constraints on the rotation of Comet P/Halley," *Icarus*, Vol. 93, No. 2, 1991, pp. 194–225.

[31] Murakami, C., "Analytical solution of the Euler-Poinsot problem," *Journal of Geometry and Symmetry in Physics*, Vol. 60, 2021, pp. 25–46.

[32] Fukushima, T., "Simple, regular, and efficient numerical integration of rotational motion," *The Astronomical Journal*, Vol. 135, No. 6, 2008, p. 2298.

[33] Benson, C. J., Scheeres, D. J., and Moskovitz, N. A., "Spin state evolution of asteroid (367943) Duende during its 2013 earth flyby," *Icarus*, Vol. 340, 2020, p. 113518.

DISTRIBUTION A: Distribution approved for public release.

[34] Vince, J., "Quaternion Algebra," *Quaternions for Computer Graphics*, Springer London, London, 2021, pp. 77–103. https://doi.org/10.1007/978-1-4471-7509-4_6.

[35] Abramowitz, M., and Stegun, I. A., *Handbook of mathematical functions with formulas, graphs, and mathematical tables*, Vol. 55, US Government printing office, 1948.

[36] Longuski, J., and Frueh, C., "AAE 340 Dynamics and Vibrations," Purdue University Lecture Notes, January 2019.

[37] Zill, D., and Carlson, B., "Symmetric elliptic integrals of the third kind," *Mathematics of computation*, Vol. 24, No. 109, 1970, pp. 199–214.

[38] Carlson, B. C., "Normal Elliptic Integrals of the First and Second Kinds," University of North Texas Libraries, UNT Digital Library, May 1963. URL https://digital.library.unt.edu/ark:/67531/metadc1201580/, last accessed June 8, 2023.

[39] Wright, S. J., *Numerical optimization*, 2006, Chaps. Quasi-Newton Methods, pp. 136–143.

[40] Hapke, B., *Theory of reflectance and emittance spectroscopy*, Cambridge university press, 2012, Chap. 10.3 Reciprocity, pp. 264–265.

[41] Minnaert, M., "The reciprocity principle in lunar photometry," *Astrophysical Journal, vol. 93, p. 403-410 (1941).*, Vol. 93, 1941, pp. 403–410.

[42] Meaney, C., "Landsat 8 (LDCM)," NASA 3D Resources, June 2016. URL https://nasa3d.arc.nasa.gov/detail/landsat-8, last accessed on 10/25/23.

[43] Duvenhage, B., Bouatouch, K., and Kourie, D., "Numerical Verification of Bidirectional Reflectance Distribution Functions for Physical Plausibility," *SAICSIT '13: Proceedings of the South African Institute for Computer Scientists and Information Technologists Conference*, 2013, pp. 200–208. https://doi.org/10.1145/2513456.2513499.

[44] Pedregosa, F., Varoquaux, G., Gramfort, A., Michel, V., Thirion, B., Grisel, O., Blondel, M., Prettenhofer, P., Weiss, R., Dubourg, V., Vanderplas, J., Passos, A., Cournapeau, D., Brucher, M., Perrot, M., and Duchesnay, E., "Scikit-learn: Machine Learning in Python," *Journal of Machine Learning Research*, Vol. 12, 2011, pp. 2825–2830.

[45] Alliance, U. L., "Vulcan Centaur Cutaway Poster (PDF)," https://www.ulalaunch.com/docs/default-source/rockets/vulcancentaur.pdf?sfvrsn=10d7f58f_2, 2022. Last accessed December 5, 2023.

[46] Markley, F. L., and Crassidis, J. L., *Fundamentals of spacecraft attitude determination and control*, Vol. 1286, Springer, 2014.

[47] Falduto, V., Lippman, D., Norwood, R., Rachael, G., and Abramson, J. P., "Algebra and trigonometry," , 2015.

[48] Merlet, J.-P., "A note on the history of trigonometric functions and substitutions," *Proceedings of HMM*, 2004.

DISTRIBUTION A: Distribution approved for public release.

LIST OF SYMBOLS

I	irradiance in $\left[\frac{W}{m^2}\right]$
$\check{I}$	normalized irradiance in $[W]$
I_0	Irradiance of Vega $\left[\frac{W}{m^2}\right]$
m	Apparent magnitude $[nondim]$
JD	Julian date
T	Julian centuries
θ_{GMST}	Greenwich mean sidereal time
θ_r	Angular offset of the first zero of the Airy disk diffraction pattern
$C_{\text{airy}}(\theta)$	CCD signal amplitude due to an Airy disk diffraction pattern $[ADU]$
k	Wavenumber
r_d	Telescope aperture radius $[m]$
r_o	Telescope central obstruction radius $[m]$
d	Telescope aperture diameter $[m]$
A_{aperture}	Telescope aperture area $[m^2]$
A_{eff}	Telescope effective aperture area $[m^2]$
f	Telescope focal length $[m]$
λ	Wavelength $[m]$
$FWHM$	Full width at half maximum
$C_{\text{gauss}}(\theta)$	CCD signal amplitude due to a Gaussian approximation of the Airy disk $[ADU]$
$\mathcal{ZM}(\lambda)$	Representative zero apparent magnitude star irradiance spectrum $\left[\frac{W}{m^2 \cdot m}\right]$
$\text{QE}(\lambda)$	Quantum efficiency spectrum $\left[\frac{ADU}{m}\right]$
$\text{ATM}(\lambda)$	Atmospheric transmission spectrum $\left[\frac{1}{m}\right]$
$K_{\text{cd}}(\lambda)$	Luminous efficacy spectrum $\left[\frac{lm}{W}\right]$
$\mathcal{S}_{\text{int}}$	CCD ADU conversion factor $\left[\frac{ADU}{W \cdot m^{-2} \cdot s}\right]$
$\text{sun}(\lambda)$	Solar irradiance spectrum $\left[\frac{W}{m^2 \cdot m}\right]$
$\mathcal{A}(\lambda)$	Airglow radiance spectrum $\left[\frac{W}{m^2 \cdot m \cdot sr}\right]$
$\mathcal{A}_{\text{int}}$	Intermediate airglow signal $\left[\frac{1}{s \cdot sr}\right]$
θ_z	Zenith angle $[rad]$

DISTRIBUTION A: Distribution approved for public release.

$\mathrm{AM}(\theta_z)$	Relative airmass function $[nondim]$
s_{pix}	Telescope pixel scale $\left[\frac{arcsec}{pix}\right]$
Δt	CCD integration time $[s]$
$B_{\mathrm{poll},z}$	Zenith light pollution brightness in magnitudes per square arcsecond
$\bar{S}_{\mathrm{airglow}}$	Mean airglow signal $[ADU]$
γ	Solar zenith angle $[deg]$
$B_{twi,z}$	Zenith twilight brightness in magnitudes per square arcsecond
$\bar{S}_{\mathrm{twilight}}$	Mean twilight signal $[ADU]$
$\mathcal{Z}$	Zero magnitude starlight signal $[\frac{ADU}{s}]$
$\bar{S}_{\mathrm{star}}$	Mean integrated starlight signal $[ADU]$
F_{rs}	Moonlight Rayleigh scattering radiance spectrum $\left[\frac{W}{m^2 \cdot m \cdot sr}\right]$
F_{ms}	Moonlight Mie scattering radiance spectrum $\left[\frac{W}{m^2 \cdot m \cdot sr}\right]$
F_{mt}	Total scattered moonlight radiance spectrum $\left[\frac{W}{m^2 \cdot m \cdot sr}\right]$
$f(\theta)$	Lunar brightness phase function $[nondim]$
$\bar{S}_{\mathrm{moon}}$	Mean scattered moonlight signal $[ADU]$
$\bar{S}_{\mathrm{zod}}$	Mean zodiacal light signal $[ADU]$
$\lambda_{\mathrm{background}}$	Mean of background signal Poisson distribution $[ADU]$
$\hat{\boldsymbol{n}}$	Face outward pointing unit normal vector
(v_1, v_2, v_3)	First, second, and third vertices $v_{\mathrm{i}} \in \mathbb{R}^3$ on a given triangular face
h_{i}	Support of the ith face
$\boldsymbol{E}$	Extended Gaussian Image
f_r	Bidirectional Reflectance Distribution Function
$\hat{\boldsymbol{\ell}}$	Illumination direction unit vector
$\hat{\boldsymbol{o}}$	Observation direction unit vector
$\hat{\boldsymbol{h}}$	Halfway unit vector
C_d	Coefficient of diffuse reflection
C_s	Coefficient of specular reflection
C_a	Coefficient of absorption
n	Specular exponent

DISTRIBUTION A: Distribution approved for public release.

2. Light Curve Simulation

Light curve simulation and inversion requires background knowledge in attitude kinematics, time and coordinate systems, computer graphics, and photometry. This section is broken into two major parts: simulating the object and its properties, and simulating the observations. The object simulation discussion proceeds with:

1. Orbit and attitude propagation,
2. Discrete mesh representations of shapes,
3. Reflectance functions,
4. Simulating light curves for convex objects,
5. Simulating light curves for nonconvex objects.

The discussion of the observation simulation proceeds with:

1. Time and coordinate systems,
2. Modeling the telescope sensor,
3. Modeling the background,
4. Observer constraints.

This overall ordering for the simulation section of this work was chosen to promote an understanding of the object and its reflection properties in a simplified manner before expanding on the physics of the observer to introduce noise and accurate observation intervals to the light curve. To preface this section, the light curve and its common units must first be defined.

DISTRIBUTION A: Distribution approved for public release.

2.0.1 The Light Curve

The light curve expresses the observed brightness of an object over time. In literature, that brightness is commonly expressed in terms of irradiance, apparent magnitude, or photoelectron counts. These units are discussed in Section 2.1.9 This work also considers the normalized irradiance for some simulation and inversion tasks. Converting between these representations is accomplished with Eqs 2.79 and 2.30.

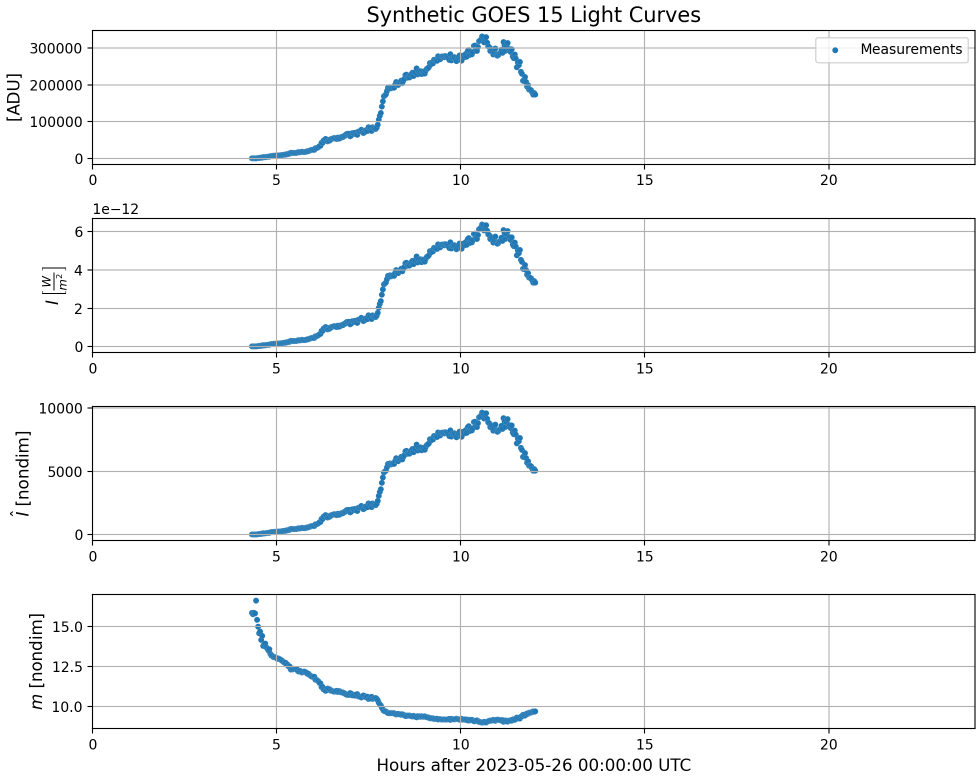

Figure 2.1. Synthetic light curves in counts, irradiance, normalized irradiance, and apparent magnitude

Figure 2.1 details this equivalence with the same light curve expressed in these four unit systems. This figure also displays an important characteristic of real measured light curves: they are always contaminated with noise. As a result, the "true mean" signal in Figure 2.1 cannot be obtained through the raw measurements, and is merely computed here as a stepping stone to the measured digital signal in the CCD. The sources of this noise are described in detail in Section 2.5.

DISTRIBUTION A: Distribution approved for public release.

2.1 Simulating Space Object Dynamics and Properties

2.1.1 Orbit Propagation

There are many environmental perturbations that influence the natural motion of space objects in orbits around Earth. In LEO, drag and the J_2 term of Earth's gravity field due to equatorial oblateness are the dominant perturbations [4]. In MEO and GEO, solar radiation pressure (SRP) and the third-body effects of the Sun and Moon become increasingly important while drag is negligible [4]. For the purposes of accurate light curve simulation, the orbit propagation must be accurate enough for the hour to week-long scenarios, and it should also be easy to access real initial conditions for objects of interest near the propagation dates. To access historical and predicted trajectories of real space objects in the public catalog, Two-Line Element sets (TLEs) are used. TLEs are short, standardized collections of orbital elements and mission information, produced from observations of the object in question close to the publication date [3]. TLEs are available programmatically through Space-Track, a service provided by the US Space Force's 18th Space Defense Squadron [49]. The Simplified General Perturbations 4 (SGP4) propagator is used to propagate near-Earth objects from TLEs. SGP4 models the secular effects of the first few zonal terms of Earth's gravity field, drag through an exponential density atmosphere, and some of the effects of third bodies like the Sun and Moon [3]. It should be noted that an improved propagator known as SGP4-XP has been developed to better model SRP, cislunar objects, gravitational harmonics, and atmospheric drag [50]. TLEs for SGP4-XP and SGP4 are not interchangeable [50]. The SGP4 propagator takes as input a Two-Line Element (TLE) set along with the Julian dates to propagate the object to and returns the position and velocity in the True Equator, Mean Equinox reference frame described in Section 2.4.4 [3]. While SGP4 does not model some important perturbations like SRP, the availability of frequently updated TLEs for regularly tracked objects alleviates most concerns, although errors on the order of a few kilometers are still expected for LEO objects [3].

Orbital propagation for the simulations performed in this work was done using SGP4 with TLE interpolation. For a given set of Julian dates and the satellite name in question, Space-Track is queried to find all TLEs produced for that object in the interval of interest.

DISTRIBUTION A: Distribution approved for public release.

SGP4 is run for all Julian dates and all TLEs, and the final position at each Julian date is linearly interpolated between the most recent past TLE and the next future TLE. If there is only one neighboring TLE, its position is used without interpolation.

2.1.2 Attitude Propagation

In order to effectively compute reflections and shadows on the surfaces of space objects, that object must have an assigned orientation in inertial space. While defunct satellites and space debris are slowly spun up by the Yarkovsky-O'Keefe-Radzievskii-Paddack (YORP) effect, the short-term motion of non-operational space objects is well-approximated by torque-free motion [51]. Developing the kinematics of torque-free motion first requires an understanding of common kinematic representations of orientation.

The orientation — or attitude — of a rigid body in three dimensions is implicitly understood to be relative to some other reference frame. The direction of a unit vector can be expressed with two numbers — the azimuth and elevation of that vector. Naively, this could be extrapolated to conclude that six numbers are needed to express an orientation. Because the basis vectors form an orthonormal set $\left\{\hat{\boldsymbol{b}}_1, \hat{\boldsymbol{b}}_2, \hat{\boldsymbol{b}}_3\right\}$, it follows for a right-handed system that $\hat{\boldsymbol{b}}_3 = \hat{\boldsymbol{b}}_1 \times \hat{\boldsymbol{b}}_2$, $\hat{\boldsymbol{b}}_2 = \hat{\boldsymbol{b}}_3 \times \hat{\boldsymbol{b}}_1$, and $\hat{\boldsymbol{b}}_1 = \hat{\boldsymbol{b}}_2 \times \hat{\boldsymbol{b}}_3$. Each of these equations constrains one further degree of freedom, revealing that a minimum of three quantities are necessary to express the relative orientation of two reference frames. This minimum bound does not make any statements about the usefulness of three element sets; at least four dimensions are needed to remove singularities [52].

2.1.2.1 The Direction Cosine Matrix

The direction cosine matrix (DCM) is a 3×3 symmetric, orthogonal matrix, expressing the three basis vectors of one frame in another. This amounts to projecting each basis vector in the first frame onto each basis vector of the second frame — the cosine of the angle between the compared vectors. It is notated with two capital letters, the rightmost indicating the reference frame of the input vectors and the leftmost indicating the transformed frame. Alternatively, the DCM is sometimes expressed as C when the frames involved are arbitrary

DISTRIBUTION A: Distribution approved for public release.

or do not need to be denoted. For example, the DCM $[\mathcal{BN}]$ takes a vector ${}^{\mathcal{N}}\boldsymbol{r}$ in the $\mathcal{N}$ frame to the $\mathcal{B}$ frame as ${}^{\mathcal{B}}\boldsymbol{r}$ [53]:

$$ {}^{\mathcal{B}}\boldsymbol{r} = [\mathcal{BN}]\,{}^{\mathcal{N}}\boldsymbol{r}. \tag{2.1} $$

The orthogonal property of the DCM implies $[\mathcal{BN}]^{-1} = [\mathcal{BN}]^{T}$ such that $[\mathcal{BN}]^{T} = [\mathcal{NB}]$ [53]. Note that the DCM is also notated as C for a transformation between two arbitrary reference frames.

2.1.2.2 Principal Rotation Parameters

Another common attitude representation is the Euler angle-axis set, otherwise known as principal rotation parameters [52]. Euler's rotation theorem guarantees that any relative orientation can be expressed as a single rotation about an axis $\hat{\boldsymbol{\lambda}} \in \mathbb{S}^2$ by an angle $\theta \in [0, 2\pi]$ [52]. The set $\left\{\hat{\boldsymbol{\lambda}}, \theta\right\}$ is known as a principal rotation parameter, abbreviated PRP hereafter. The DCM C with entries C_{ij} for the ith row and jth column is mapped to the PRP representation with [53]:

$$ \theta = \cos^{-1}\left(\frac{1}{2}\left[C_{11} + C_{22} + C_{33} - 1\right]\right), \tag{2.2} $$

$$ \hat{\boldsymbol{\lambda}} = \frac{1}{2\sin\theta}\begin{bmatrix} C_{23} - C_{32} \\ C_{31} - C_{13} \\ C_{12} - C_{21} \end{bmatrix}, $$

The mapping from a PRP $\left\{\hat{\boldsymbol{\lambda}}, \theta\right\}$ to a DCM C is also relatively straightforward [53]:

$$ C = I_3 + \sin\theta\left[\hat{\boldsymbol{\lambda}}\times\right] + (1 - \cos\theta)\left[\hat{\boldsymbol{\lambda}}\times\right]^2, \tag{2.3} $$

were I_3 is the $[3 \times 3]$ identity matrix and $[v\times]$ is the matrix cross product operator, defined on $\boldsymbol{v} \in \mathbb{R}^3$ as [53]:

DISTRIBUTION A: Distribution approved for public release.

$$[\boldsymbol{v}\times] = \begin{bmatrix} 0 & -v_3 & v_2 \\ v_3 & 0 & -v_1 \\ -v_2 & v_1 & 0 \end{bmatrix}. \tag{2.4}$$

This operator is useful as it rephrases the cross product as matrix multiplication, i. e. $\boldsymbol{v} \times \boldsymbol{u} = [\boldsymbol{v}\times]\,\boldsymbol{u}$. While the PRP $\{\theta, \hat{\boldsymbol{\lambda}}\}$ is a four element set, there are only three degrees of freedom due to the unit norm constraint on $\hat{\boldsymbol{\lambda}}$.

2.1.2.3 Quaternions

The quaternion represents attitude with a point on the surface of the hypersphere $\mathbb{S}^3$. In terms of the PRP axis and angle $\left\{\hat{\boldsymbol{\lambda}}, \theta\right\}$, the quaternion $\boldsymbol{q}$ is given by [52]:

$$\boldsymbol{q} = \begin{bmatrix} \hat{\boldsymbol{\lambda}} \sin\left(\frac{\theta}{2}\right) \\ \cos\left(\frac{\theta}{2}\right) \end{bmatrix}. \tag{2.5}$$

The first three entries of the quaternion are often called the vector component, with the final entry being the scalar component. Some authors reorder the quaternion, placing the scalar term first. Often the entries of a single quaternion are referenced by index such that $\boldsymbol{q} = [q_1, q_2, q_3, q_4]$. Similarly, the vector portion of the quaternion is referenced with $\boldsymbol{q}_{1:3}$. The quaternion can be mapped back to the PRP [52] via:

$$\begin{aligned} \theta &= 2\cos^{-1}(q_4) \\ \hat{\boldsymbol{\lambda}} &= \frac{\boldsymbol{q}_{1:3}}{\sin\frac{\theta}{2}}. \end{aligned} \tag{2.6}$$

The quaternion maps to the DCM C [52] via:

$$C = \begin{bmatrix} -q_2^2 - q_3^2 + q_1^2 + q_4^2 & 2\,q_1q_2 + 2\,q_3q_4 & 2\,q_1q_3 - 2\,q_2q_4 \\ 2\,q_1q_2 - 2\,q_3q_4 & -q_1^2 - q_3^2 + q_2^2 + q_4^2 & 2\,q_1q_4 + 2\,q_2q_3 \\ 2\,q_1q_3 + 2\,q_2q_4 & 2\,q_2q_3 - 2\,q_1q_4 & -q_1^2 - q_2^2 + q_3^2 + q_4^2 \end{bmatrix} \tag{2.7}$$

DISTRIBUTION A: Distribution approved for public release.

2.1.3 Attitude Kinematics

Quaternion kinematic differential equations are chosen for simulating object attitude profiles as they have no singularity and produce very smooth dynamics that are easy to integrate when compared to three-variable representations that possess singularities. Given the current orientation quaternion $\boldsymbol{q} = [q_1, q_2, q_3, q_4]^T$ representing the orientation of the body frame in inertial space and angular velocity of the body frame in inertial space $\boldsymbol{\omega} = [\omega_1, \omega_2, \omega_3]^T$ the quaternion derivative is computed via [52]:

$$\begin{bmatrix} \dot{q}_1 \\ \dot{q}_2 \\ \dot{q}_3 \\ \dot{q}_4 \end{bmatrix} = \frac{1}{2} \begin{bmatrix} q_4 & -q_3 & q_2 & q_1 \\ q_3 & q_4 & -q_1 & q_2 \\ -q_2 & q_1 & q_4 & q_3 \\ -q_1 & -q_2 & -q_3 & q_4 \end{bmatrix} \begin{bmatrix} \omega_1 \\ \omega_2 \\ \omega_3 \\ 0 \end{bmatrix}. \tag{2.8}$$

2.1.4 Attitude Dynamics

Rigid body dynamics can be easily expressed in the body principal axes for an object with the diagonal inertia tensor $J = \text{diag}\,(J_1, J_2, J_3)$ with an arbitrary torque vector $\boldsymbol{M} = [M_1, M_2, M_3]^T$ in the same frame via [52]:

$$\begin{bmatrix} \dot{\omega}_1 \\ \dot{\omega}_2 \\ \dot{\omega}_3 \end{bmatrix} = \begin{bmatrix} (M_1 + J_2\omega_2\omega_3 - J_3\omega_2\omega_3)/J_1 \\ (M_2 - J_1\omega_1\omega_3 + J_3\omega_1\omega_3)/J_2 \\ (M_3 + J_1\omega_1\omega_2 - J_2\omega_1\omega_2)/J_3 \end{bmatrix}. \tag{2.9}$$

Equations 2.9 and 2.8 are numerically integrated to yield the orientation time history which is necessary for later light curve simulations. Often, $\boldsymbol{M} = \boldsymbol{0}$ is chosen to simulate the torque-free evolution of an initial orientation and spin state, neglecting small attitude perturbations over the simulation interval.

2.1.5 Discrete Shape Representations

A computer can represent 3D objects implicitly or explicitly. An implicit representation might be the solution to an algebraic equation, i. e. $x^2 + y^2 + z^2 = 1$ defines a sphere of

DISTRIBUTION A: Distribution approved for public release.

radius 1 centered at the origin. Often, a shape may be defined by a set of signed distance functions (SDFs). An SDF takes in a point in $\mathbb{R}^3$ and outputs the distance from the object, returning negative distance if the queried point is inside the shape. The object can then be rendered via ray marching. A ray is cast from the camera out into the scene for each pixel of the screen, each performing distance queries along its length until it intersects the object or diverges.

By contrast, an explicit shape representation creates complex 3D geometry from simple 2D building blocks. In the most common case, object faces are defined by triangles. This means that at the scale of the individual faces, the shape is always composed of flat surfaces that meet at sharp angles. While this can add complexity to many fields of shape analysis and geometry processing, triangulated surfaces are perfect for light curve shape inversion. Human-made space objects like most satellites are composed of flat faces, with the exception of parabolic antennas and cylindrical rocket bodies.

2.1.5.1 The Object File Format

One common text file format for 3D model files is `.obj`, developed by Wavefront Technologies in the early 1990s [54]. Each OBJ file consists of a list of vertex positions and face definitions, with optional vertex normals and tangents. An `.obj` listing for a cube is included for reference in Appendix 6.4. Given the vertex positions and adjacency information stored in the model file, useful properties of the object can be computed for use later in both light curve simulation and shape inversion.

2.1.5.2 Properties of Triangulated Meshes

For each triangular face F_i of the model defined by vertices $F_\mathrm{i} = \{v_1, v_2, v_3\}$, the outward-pointing face normal is computed with:

$$\hat{\boldsymbol{n}} = \frac{(v_2 - v_1) \times (v_3 - v_1)}{\| (v_2 - v_1) \times (v_3 - v_1) \|_2}. \tag{2.10}$$

The face area a is computed with:

DISTRIBUTION A: Distribution approved for public release.

$$a = \frac{\| (v_2 - v_1) \times (v_3 - v_1) \|_2}{2}. \tag{2.11}$$

The support h_i of the ith face — the perpendicular distance from the origin to the plane defining the face — is computed with the position of any vertex on that face, i. e. , the first vertex $v_{\mathrm{i},1}$, and the face normal vector $\hat{\boldsymbol{n}}_\mathrm{i}$:

$$h_\mathrm{i} = v_{\mathrm{i},1} \cdot \hat{\boldsymbol{n}}_\mathrm{i}. \tag{2.12}$$

The volume of the object v is computed:

$$v = \frac{1}{3} \sum_{\mathrm{i}=0}^{|F|} \boldsymbol{h}_\mathrm{i} \cdot \boldsymbol{a}_\mathrm{i}. \tag{2.13}$$

In Equation 2.13, $|F|$ is the number of faces defining the object. $\boldsymbol{h}$ and $\boldsymbol{a}$ are column vectors collecting all face supports and areas. The Extended Gaussian Image $\boldsymbol{E}$, a quantity defined in 3.2.1, is computed row-wise for the ith face with:

$$\boldsymbol{E}_\mathrm{i} = \boldsymbol{a}_\mathrm{i} \hat{\boldsymbol{n}}_\mathrm{i}. \tag{2.14}$$

2.1.6 The Bidirectional Reflectance Distribution Function

Although light curves come from unresolved measurements, the interactions that produce them are directly driven by the shape and material properties of the object being observed. In order to simulate accurate light curves, all relevant optical interactions must be modeled. In broad terms, this boils down to determining how the object is illuminated, how it casts shadows on itself, and how it is observed.

At the microscopic scale, the surface of an object is composed of facets — small areas sharing a normal vector. The macroscopic optical properties of the material is driven by the distribution of sizes and normal directions of these microfacets. If the facet normals are distributed in biased orientations, the macroscopic surface may show anisotropy, leading to the appearance of brushed metal. If the microfacet normals are at large angles to each other, the surface may appear dull as the direction of the outgoing light may be largely independent

DISTRIBUTION A: Distribution approved for public release.

from the incoming direction. Subsurface effects — where incoming light rays scatter *inside* the surface — can also change the macroscopic properties of the material.

This discussion raises an important question; how should the macroscopic outcomes of the microscopic interactions of incident light on a surface be modeled? The bidirectional reflectance distribution function (BRDF) is a tool from computer graphics that addresses this problem. The BRDF is a function on the hemisphere which expresses the fraction of light per solid angle (radiance $\mathcal{R}$) leaving the surface in a given direction, divided by the incident power per unit area (irradiance $\mathcal{I}$). The general formulation for the BRDF reflectance fraction f_r is given by [55]:

$$f_r(\boldsymbol{x}, \hat{\boldsymbol{\ell}}, \hat{\boldsymbol{o}}) = \frac{d\mathcal{R}\left(\boldsymbol{x}, \hat{\boldsymbol{o}}\right)}{d\mathcal{I}\left(\hat{\boldsymbol{\ell}}, \boldsymbol{x}\right)}. \tag{2.15}$$

In Equation 2.15, $\boldsymbol{x} \in \mathbb{R}^3$ is the point on the object's surface where the BRDF is evaluated. $\hat{\boldsymbol{\ell}} \in \mathbb{S}^2$ is the incoming illumination unit vector and $\hat{\boldsymbol{o}} \in \mathbb{S}^2$ is the outgoing unit vector. Note that this work treats $f_r(\boldsymbol{x}, \hat{\boldsymbol{\ell}}, \hat{\boldsymbol{o}})$ and $f_r(\hat{\boldsymbol{\ell}}, \hat{\boldsymbol{o}})$ as equivalent in later descriptions, leaving the evaluation point $\boldsymbol{x}$ implied. This definition is useful for building intuition about the form of the BRDF, but to represent a physically plausible reflection process, a candidate function must satisfy three additional constraints. A physically plausible BRDF must conserve energy — more energy cannot be reflected from the surface than was incident on it. It must also be reciprocal — switching the observer and illumination directions should not change the BRDF value as the surface interaction. This reciprocity is sometimes known as the *Helmholtz Reciprocity Rule* in literature [56]. Finally, plausible BRDFs are positive — they take on nonnegative values for all valid inputs [56]. A surface cannot reflect negative light, so this is expected. Explicitly, energy conservation is expressed with [56]:

$$\forall \hat{\boldsymbol{\ell}} \in \mathbb{S}^2 : \int_{\hat{\boldsymbol{o}} \in \mathbb{S}^2} f_r(\hat{\boldsymbol{\ell}}, \hat{\boldsymbol{o}})\, d\mathbb{S}^2 \leq 1. \tag{2.16}$$

Equation 2.16 states that for all possible illumination directions $\hat{\boldsymbol{\ell}}$, integrating all possible outgoing observer directions $\hat{\boldsymbol{o}}$ on the unit sphere cannot return greater than one from the energy conservation integral. Reciprocity can be formalized as:

DISTRIBUTION A: Distribution approved for public release.

$$\forall \hat{\boldsymbol{\ell}}, \hat{\boldsymbol{o}} \in \mathbb{S}^2 : \quad f_r(\hat{\boldsymbol{\ell}}, \hat{\boldsymbol{o}}) = f_r(\hat{\boldsymbol{o}}, \hat{\boldsymbol{\ell}}). \tag{2.17}$$

Now that the requirements for a plausible physical BRDF have been established, a collection of commonly-used BRDFs can be presented. The following BRDFs are all energy conserving, reciprocal, and nonnegative. Real-world materials are modeled with these BRDFs by fitting the free parameters of a given BRDF to measured reflectance data [28]. If a BRDF can be fit to the data with low error, that reflection function can be considered to be a faithful model for the true physics.

2.1.6.1 Lambertian

The simplest BRDF is one that reflects equally in all directions. This BRDF is termed Lambertian or diffuse.

$$f_r(\hat{\boldsymbol{\ell}}, \hat{\boldsymbol{o}}) = \frac{C_d}{\boldsymbol{\pi}} \tag{2.18}$$

In Equation 2.18, $0 \leq C_d \leq 1$ is the surface's coefficient of diffuse reflection. For example, $C_d = 0.4$ means that the surface reflects 40% of incident radiation and absorbs the other 60%.

While the diffuse BRDF reflects energy isotropically, many real-world reflections are highly biased. At the extreme end, a perfect mirror reflection is effectively a Dirac delta function in the reflected illumination direction. Many real-world materials are well modeled as a linear combination of diffuse and specular effects.

2.1.6.2 Phong

A simple specular BRDF model is that developed by Phong in 1975 [24]. The Phong model splits the BRDF into a Lambertian term governed by C_d and a specular term governed the coefficient of specular reflection $0 \leq C_s \leq 1$ and the specular exponent $n \geq 0$ [55].

$$f_r(\hat{\boldsymbol{\ell}}, \hat{\boldsymbol{o}}) = \frac{C_d}{\boldsymbol{\pi}} + \frac{C_s \frac{n+2}{2\boldsymbol{\pi}} (\hat{\boldsymbol{o}} \cdot \hat{\boldsymbol{r}})^n}{\hat{\boldsymbol{n}} \cdot \hat{\boldsymbol{\ell}}} \tag{2.19}$$

DISTRIBUTION A: Distribution approved for public release.

In Equation 2.19, $\hat{\boldsymbol{r}}$ is the reflected illumination vector, computed via $\hat{r} = \frac{2(\hat{\boldsymbol{n}}\cdot\hat{\boldsymbol{\ell}})\hat{\boldsymbol{n}}-\hat{\boldsymbol{\ell}}}{\|2(\hat{\boldsymbol{n}}\cdot\hat{\boldsymbol{\ell}})\hat{\boldsymbol{n}}-\hat{\boldsymbol{\ell}}\|}$. As n increases, the specular glint becomes sharper and more intense, eventually approaching a perfect mirror reflection. Because of the introduction of a new coefficient of reflection, a new constraint is needed to maintain energy conservation. Because C_d and C_s each represent the *fraction* of light reflected in each mode, it should be clear that $C_d + C_s \leq 1$. This can also be reformulated with an explicit coefficient of absorption C_a which captures the fraction of incident radiation absorbed by the surface, yielding $C_d + C_s + C_a = 1$. It must be noted that the Phong model is only approximately reciprocal as it is based on the reflected incident vector $\hat{\boldsymbol{r}}$ instead of the halfway vector $\hat{\boldsymbol{h}}$ used by other models [55].

2.1.6.3 Blinn-Phong

The Blinn-Phong BRDF is similar to the Phong BRDF, but it parameterizes the specular lobe in terms of the halfway vector $\hat{\boldsymbol{h}}$ [55]. This vector is halfway between the illumination and observer directions such that $\hat{\boldsymbol{h}} = \hat{\boldsymbol{\ell}} + \hat{\boldsymbol{o}}$ which needs to be normalized before use. As the halfway vector approaches the surface normal vector, the observer must be approaching the reflected illumination vector, leading to a more intense specular highlight.

$$f_r(\hat{\boldsymbol{\ell}}, \hat{\boldsymbol{o}}) = \frac{C_d}{\pi} + \frac{C_s \frac{n+2}{2\pi}(\hat{\boldsymbol{n}}\cdot\hat{\boldsymbol{h}})^n}{4(\hat{\boldsymbol{n}}\cdot\hat{\boldsymbol{\ell}})(\hat{\boldsymbol{n}}\cdot\hat{\boldsymbol{o}})} \tag{2.20}$$

2.1.6.4 Glossy

The so-called glossy BRDF simulates reflections from plastic materials using an Gaussian distribution around the specular scattering lobe [55]:

$$f_r(\hat{\boldsymbol{\ell}}, \hat{\boldsymbol{o}}) = \frac{C_d}{\pi} + \frac{C_s}{2\pi\sigma^2\left(\hat{\boldsymbol{n}}\cdot\hat{\boldsymbol{\ell}}\right)} \mathrm{e}^{\frac{-(\hat{\boldsymbol{r}}\cdot\hat{\boldsymbol{o}})^2}{2\sigma^2}}, \tag{2.21}$$

where the parameter σ controls the spread — the standard deviation — of the specular Gaussian. It must be noted that the Glossy model is only approximately reciprocal as it is based on the reflected incident vector $\hat{\boldsymbol{r}}$ instead of the halfway vector $\hat{\boldsymbol{h}}$ used by other models [55].

DISTRIBUTION A: Distribution approved for public release.

2.1.6.5 Cook-Torrance

The Cook-Torrance explicitly accounts for the orientation of the microfacets making up the surface [26]. This model is built from a facet slope distribution term D_{ct}, a Fresnel term F, and a geometric attenuation factor G_{ct}. The slope distribution term describes the probability density of a given facet being oriented with a normal vector aligned with the halfway vector $\hat{\boldsymbol{h}}$ [26]. A common formulation of this term is due to Beckmann, where $\alpha \in [0, 1]$ is the roughness of the surface [26]:

$$D_{ct} = \frac{1}{\pi\alpha^2 \left(\hat{\boldsymbol{n}} \cdot \hat{\boldsymbol{h}}\right)^4} \exp\left(\frac{1 - \left(\hat{\boldsymbol{n}} \cdot \hat{\boldsymbol{h}}\right)^2}{\alpha^2 \left(\hat{\boldsymbol{n}} \cdot \hat{\boldsymbol{h}}\right)^2}\right). \tag{2.22}$$

The Fresnel term accounts for the variation in specular reflection due to the angle of incidence. In reality, this term is a function of wavelength, but it is often approximated as a function of the coefficient of specular reflection C_s as well as the halfway and illumination directions $\hat{\boldsymbol{h}}$ and $\hat{\boldsymbol{\ell}}$ respectively [26]:

$$F = C_s + (1 - C_s)\left(1 - \left(\hat{\boldsymbol{h}} \cdot \hat{\boldsymbol{\ell}}\right)\right)^5. \tag{2.23}$$

The geometric attenuation term G_{ct} expresses how microfacets shadow each other, and can be approximated with [26]:

$$G_{ct} = \min\left\{1, \frac{2\left(\hat{\boldsymbol{n}} \cdot \hat{\boldsymbol{h}}\right)\left(\hat{\boldsymbol{n}} \cdot \hat{\boldsymbol{o}}\right)}{\hat{\boldsymbol{o}} \cdot \hat{\boldsymbol{h}}}, \frac{2\left(\hat{\boldsymbol{n}} \cdot \hat{\boldsymbol{h}}\right)\left(\hat{\boldsymbol{n}} \cdot \hat{\boldsymbol{\ell}}\right)}{\hat{\boldsymbol{o}} \cdot \hat{\boldsymbol{h}}}\right\}. \tag{2.24}$$

The overall reflectance for the Cook-Torrance BRDF is given by:

$$f_r(\hat{\boldsymbol{\ell}}, \hat{\boldsymbol{o}}) = \frac{C_d}{\pi} + \frac{D_{ct} \cdot G_{ct} \cdot F}{4\left(\hat{\boldsymbol{n}} \cdot \hat{\boldsymbol{\ell}}\right)\left(\hat{\boldsymbol{n}} \cdot \hat{\boldsymbol{o}}\right)} \tag{2.25}$$

2.1.6.6 Oren-Nayar

The Oren-Nayar BRDF is an improved model of diffuse reflectance for many real-world materials like ceramics and the surface of the Moon. These materials diverge from the

DISTRIBUTION A: Distribution approved for public release.

Lambertian model near the horizon, reflecting much more light than would be predicted by simple cosine loss [27]. This BRDF relies on the surface roughness α to compute a set of scalars A, B, C, and angles α and β [27]:

$$
\begin{aligned}
A &= 1 - 0.5\frac{\alpha^2}{\alpha^2 + 0.33} \\
B &= 0.45\frac{\alpha^2}{\alpha^2 + 0.09} \\
C &= \frac{\text{proj}_{\hat{\boldsymbol{n}}}\left(\hat{\boldsymbol{\ell}}\right)}{\|\text{proj}_{\hat{\boldsymbol{n}}}\left(\hat{\boldsymbol{\ell}}\right)\|} \cdot \frac{\text{proj}_{\hat{\boldsymbol{n}}}\left(\hat{\boldsymbol{o}}\right)}{\|\text{proj}_{\hat{\boldsymbol{n}}}\left(\hat{\boldsymbol{o}}\right)\|} \\
\beta &= \max\left\{\cos^{-1}\left(\hat{\boldsymbol{\ell}} \cdot \hat{\boldsymbol{n}}\right),\ \cos^{-1}\left(\hat{\boldsymbol{o}} \cdot \hat{\boldsymbol{n}}\right)\right\} \\
\gamma &= \min\left\{\cos^{-1}\left(\hat{\boldsymbol{\ell}} \cdot \hat{\boldsymbol{n}}\right),\ \cos^{-1}\left(\hat{\boldsymbol{o}} \cdot \hat{\boldsymbol{n}}\right)\right\}.
\end{aligned}
\tag{2.26}
$$

With these values computed, the reflectance of the Oren-Nayar BRDF is given by [27]:

$$
f_r(\hat{\boldsymbol{\ell}}, \hat{\boldsymbol{o}}) = \frac{C_d}{\boldsymbol{\pi}}\left(A + \left(B \max\left\{C, 0\right\} \sin\beta \tan\gamma\right)\right). \tag{2.27}
$$

2.1.6.7 Ashikhmin-Shirley

The Ashikhmin-Shirley BRDF is unique among those presented in this section as it allows for anisotropic reflection which can be non-negligible for metals [25]. This model is parameterized by the diffuse reflection coefficient C_d, the specular reflection coefficient C_s, as well as two specular exponents n_u and n_v. When $n_u = n_v$, the model behaves much like the Phong BRDF. The full BRDF is expressed [25]:

DISTRIBUTION A: Distribution approved for public release.

$$\rho_d = \frac{28C_d}{23\pi}(1 - C_s)\left(1 - \left(1 - \frac{\hat{\boldsymbol{n}} \cdot \hat{\boldsymbol{\ell}}}{2}\right)^5\right)\left(1 - \left(1 - \frac{\hat{\boldsymbol{n}} \cdot \hat{\boldsymbol{o}}}{2}\right)^5\right) \tag{2.28}$$

$$\rho_s = \frac{\sqrt{(n_u + 1)(n_v + 1)}}{8\pi} \frac{\left(\hat{\boldsymbol{n}} \cdot \hat{\boldsymbol{h}}\right)^{\frac{n_u\left(\hat{\boldsymbol{h}} \cdot \boldsymbol{u}\right)^2 + n_v\left(\hat{\boldsymbol{h}} \cdot \boldsymbol{v}\right)^2}{1 - \left(\hat{\boldsymbol{h}} \cdot \hat{\boldsymbol{n}}\right)^2}}}{\left(\hat{\boldsymbol{h}} \cdot \hat{\boldsymbol{\ell}}\right) \max\left\{\hat{\boldsymbol{n}} \cdot \hat{\boldsymbol{o}}, \hat{\boldsymbol{n}} \cdot \hat{\boldsymbol{\ell}}\right\}} F$$

$$f_r(\hat{\boldsymbol{\ell}}, \hat{\boldsymbol{o}}) = \rho_d + \rho_s.$$

In Equation 2.28, F is the same Fresnel factor in Equation 2.23 while $\boldsymbol{u}$ and $\boldsymbol{v}$ are predefined surface basis vectors perpendicular to the surface normal.

2.1.7 BRDF Summary

Figure 2.2. Implemented BRDFs rendered with arbitrary parameters, demonstrating the qualitative differences between lighting models

DISTRIBUTION A: Distribution approved for public release.

Material	C_d	C_s	n
Solar panel (Phong) [57]	0.15	0.25	0.26
Bus structure (Phong) [57]	0.34	0.40	8.9
Multilayer insulation (MLI) (Phong)	0.1	0.9	20
White paint (Phong)	0.9	0.1	1

Table 2.1. Reflection properties of real materials. MLI and white paint parameters are estimated qualitatively by the author. Significant variance may exist between objects depending on surface finishes [28].

2.1.8 Real Material Properties

Producing accurate light curves requires accurate optical properties for the simulated materials. Matusik et al. compiled measured bidirectional reflectance data from over 100 real materials including various metals and paints that might be found on human-made space objects [28]. Optimally, such a dataset would be used to model the structure, solar panels, and antenna surfaces of the simulated objects. However, it is far more computationally efficient to fit one of the presented three parameter BRDFs to observed data. The Phong model parameters used for simulations in this work are listed in Table 2.1.

2.1.9 Brightness Units

2.1.9.1 Irradiance

Irradiance is the standard SI linear unit used to describe the total amount of energy incident on a surface from a given source. An irradiance of 1 $\left[\frac{W}{m^2}\right]$ implies that a 10 $[m^2]$ area would experience 10 $[W]$ of incident power. The mean irradiance of the Sun — termed the solar constant — is derived from the mean luminosity of the Sun $L_s = 3.828 \cdot 10^{26}$ $[W]$ and a distance of 1 Astronomical Unit 1 $[AU] = 149597870.7$ $[km]$ [4]. The mean solar constant is then computed via

$$I_s = \frac{L_s}{4\pi \left(AU\right)^2} \approx 1361.0 \left[\frac{W}{m^2}\right]. \tag{2.29}$$

DISTRIBUTION A: Distribution approved for public release.

In reality, the exoatmospheric irradiance at Earth varies [4]. Figure 2.3 displays the small variations in the solar irradiance due to the solar cycle and the much larger variations due to Earth's eccentric orbit.

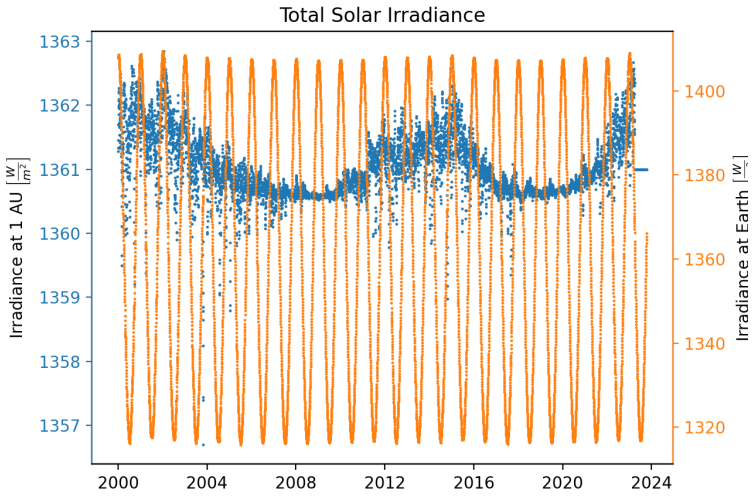

Figure 2.3. Total solar irradiance variations at Earth and 1 AU. The solar cycle is apparent when distance is held constant at 1 AU, yielding small variations in the peak intensity at Earth.

2.1.9.2 Apparent Magnitude

Apparent magnitude — also known as visual or relative magnitude — is a reverse logarithmic scale that originates in astronomy [4]. Stellar sources span many orders of magnitude of brightness, making a logarithmic scale a helpful middle ground for comparison. Note that apparent magnitude always expresses brightness at the observer's location; absolute magnitude is a different quantity that normalizes brightness from a distance of 10 parsecs [4]. Apparent magnitude m is computed from irradiance via [4]:

$$m = -2.5 \log_{10} \left(\frac{I}{I_0} \right). \tag{2.30}$$

DISTRIBUTION A: Distribution approved for public release.

In Equation 2.30, I is the irradiance of the source of interest and I_0 is irradiance of the zero-point source. This makes sense; substituting $I = I_0$ returns $m = 0$. The star Vega is usually taken to be the zero-point with irradiance $I_0 = 2.518021002 \cdot 10^{-8} \left[\frac{W}{m^2}\right]$ [4].

Equation 2.30 is rearranged to compute irradiance from a given apparent magnitude m, yielding:

$$I = I_0 \cdot 10^{-0.4m}. \tag{2.31}$$

2.1.9.3 Normalized Irradiance

The light curve simulation methods presented in this work use normalized irradiance, the received irradiance of an object at a distance of 1 meter per $[W/m^2]$ of the distant source illuminating it. This is a non-standard quantity in the literature, but proves useful for the same reasons absolute magnitude is used by astronomers. Adjusting the signal to a standard distance and illumination strength enables the simulation and inversion of light curves in a non-dimensional environment. This simplifies simulation and makes the shape inversion optimizations more robust. To make the conversion explicit, irradiance in $[W/m^2]$ observed at a distance r in meters from an object is converted to normalized irradiance due to the Sun $\check{I}$ by accounting for the r^2 loss due to distance and the I_s total solar irradiance:

$$\check{I} = \frac{r^2}{I_s} I. \tag{2.32}$$

To be precise, the normalized irradiance has units m^2 and can be interpreted as the area of a flat plate illuminated by a 1 $[W/m^2]$ light source required to reflect the same irradiance in the direction of the observer. Throughout this work, normalized irradiance is treated as being nondimensional for light curve simulation and inversion purposes as its physical interpretation is largely irrelevant.

DISTRIBUTION A: Distribution approved for public release.

2.1.10 Simulating Normalized Light Curves of Convex Objects

Light curve simulation for convex geometry can be solved semi-analytically as each face's contribution to the measured irradiance can be computed individually [10]. Determining whether a face is illuminated requires two horizon checks to determine visibility from the Sun and to the observer. For a face i at timestep j with normal vector $\hat{\boldsymbol{n}}_{\mathrm{i}}$, these horizon checks are expressed by the shadowing condition μ_{ij}.

$$\mu_{\mathrm{ij}} = \begin{cases} 1 \text{ if } (\hat{\boldsymbol{o}}_{\mathrm{j}} \cdot \hat{\boldsymbol{n}}_{\mathrm{i}}) > 0 \text{ and } \left(\hat{\boldsymbol{\ell}}_{\mathrm{j}} \cdot \hat{\boldsymbol{n}}_{\mathrm{i}}\right) > 0 \text{ and } \delta_{\mathrm{ij,ss}} = 0 \text{ and } \delta_{\mathrm{ij,os}} = 0 \\ 0 \text{ otherwise} \end{cases} \tag{2.33}$$

The unit vectors $\hat{\boldsymbol{o}}$ and $\hat{\boldsymbol{\ell}}$ point from the center of mass of the object to the observer and Sun, respectively. The outward-pointing face normal unit vector $\hat{\boldsymbol{n}}$ is chosen by convention for all mesh operations. The self-shadowing and observer-shadowing conditions, $\delta_{\mathrm{ij,ss}}$ and $\delta_{\mathrm{ij,os}}$, are always zero for convex polyhedra but are crucial for accurately simulating nonconvex geometry. For objects with concavities, self-shadowing refers to shadows cast by an object onto itself and observer-shadowing refers to otherwise visible faces blocked by other portions of the geometry.

The irradiance I received by the observer at timestep j is the sum of the received irradiance from all faces, where the BRDF is evaluated at each face. Each contribution is expressed as the product of the normalized irradiance $\check{I}$. This can be scaled to adjust for the distance from the observer to the object and the solar constant to yield the noiseless received irradiance. For any physically plausible BRDF $f_r(\hat{\boldsymbol{\ell}}, \hat{\boldsymbol{o}})$, the normalized light curve for a convex object is expressed as a sum over all faces i at time step j [5]:

$$\check{I}_{\mathrm{j}} = \sum_{\mathrm{i}=1}^{m} \mu_{\mathrm{ij}} a_{\mathrm{i}} f_r(\hat{\boldsymbol{\ell}}_{\mathrm{j}}, \hat{\boldsymbol{o}}_{\mathrm{j}}) \, (\hat{\boldsymbol{o}}_{\mathrm{j}} \cdot \hat{\boldsymbol{n}}_{\mathrm{i}}) \left(\hat{\boldsymbol{\ell}}_{\mathrm{j}} \cdot \hat{\boldsymbol{n}}_{\mathrm{i}}\right). \tag{2.34}$$

In Equation 2.34, a_{i} is the area of the ith face. Note that $f_r(\hat{\boldsymbol{\ell}}_{\mathrm{j}}, \hat{\boldsymbol{o}}_{\mathrm{j}})$ must be computed separately for each face to account for normal vector and coefficient of reflection differences.

DISTRIBUTION A: Distribution approved for public release.

This normalized light curve can be dimensionalized by the total solar irradiance and the distance r_j between the observer $\boldsymbol{r}_\mathrm{obs}$ to the object center of mass $\boldsymbol{r}_\mathrm{obj}$:

$$I_\mathrm{j} = \frac{I_s \check{I}_\mathrm{j}}{r_\mathrm{j}^2}. \tag{2.35}$$

Note that using $r_\mathrm{j} = \|\boldsymbol{r}_\mathrm{obj} - \boldsymbol{r}_\mathrm{obs}\|$ is a simplifying assumption as some faces of the object are further or closer to the Sun than the center of mass. As the scale of human-made space objects are a factor of 10^{10} to 10^{12} smaller than the distance to the Sun, the difference across the surface of the object is negligible.

2.1.11 Simulating Normalized Light Curves of Nonconvex Objects

The light curve simulation framework developed in this work relies on a pixel-by-pixel image rendering on the GPU to compute the total reflected irradiance at each timestep of the simulation. As a result, a background in common computer graphics terminology and reference frames is necessary to understand the transformation from coordinates in the object body frame to a pixel in the final image.

2.1.11.1 Camera Projections and Terminology

In computer graphics, a camera is defined by its position $\boldsymbol{r}_{cam}$, target $\boldsymbol{t}_{cam}$, reference up direction $\boldsymbol{u}_{cam}$, and a field of view FOV. In order to render a 3D scene to a 2D image using this camera, a transformation is needed. An orthographic camera accomplishes this transformation by orthogonally projecting points onto a plane perpendicular to camera look direction $\boldsymbol{t}_{cam} - \boldsymbol{r}_{cam}$. The volume of space that falls into view of the camera is known as the frustum [58]. An important consequence of orthogonal projection is that objects further away from the camera do not shrink in the image, which is sometimes advantageous. A perspective projection forms a more complex frustum that expands outwards from a near plane to a proportionally larger far plane. Because of the expansion of the frustum, geometry processed by the perspective transformation shrinks as it moves further from the near plane.

DISTRIBUTION A: Distribution approved for public release.

Figure 2.4 displays the geometry of these camera frustums, with additional reference frames detailed in Section 2.1.11.2.

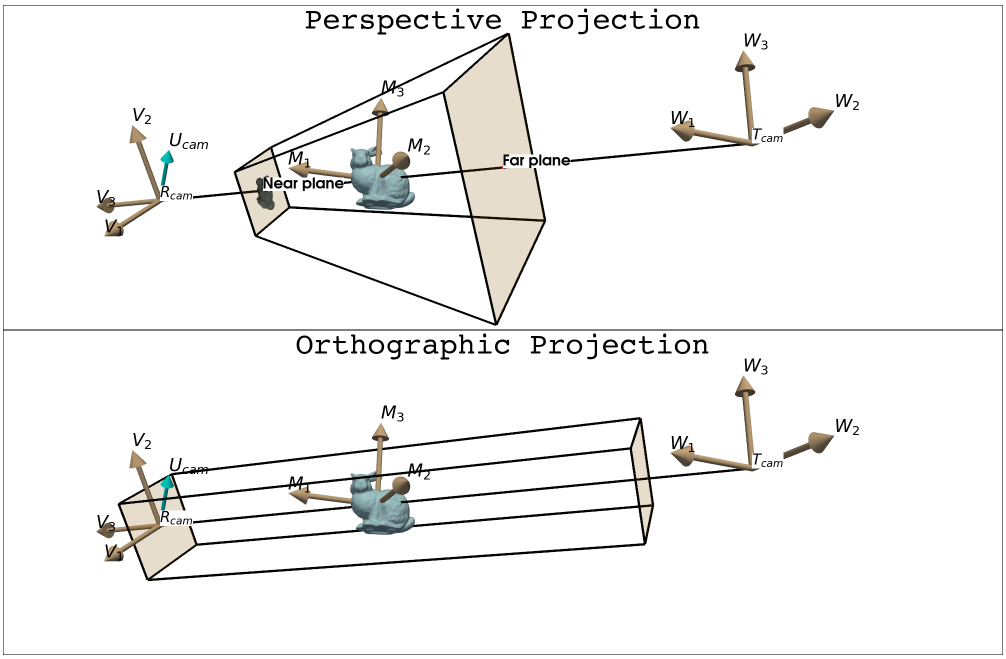

Figure 2.4. Perspective and orthographic projections with relevant camera frustum attributes labeled

While the perspective projection is shown in Figure 2.4, only orthographic projection is relevant for future simulation tasks as both the observer and Sun are assumed to be very far from the object. In the limit, the true perspective nature of the camera behaves as an orthographic projection as negligible foreshortening occurs for objects as they retreat from the camera.

2.1.11.2 Transformations

Transformations in computer graphics are often represented by 4×4 matrices. These matrices operate on so-called homogeneous coordinates, operating on vectors in $\mathbb{R}^4$ of the form $[x, y, z, w]^T$ [58]. The inclusion of the fourth component enables simultaneous rotation, translation, and scaling of the input points by the matrix, provided that the outputs are normalized to set $w = 1$ [58].

DISTRIBUTION A: Distribution approved for public release.

There are a few fundamental matrices used in computer graphics that are necessary for later hardware-accelerated light curve simulation algorithms. The first is the model matrix $M \in \mathbb{R}^{4\times4}$ which transforms from the world frame to the model frame given the origin of the model body frame $\boldsymbol{r}_m = [r_{m,x}, r_{m,y}, r_{m,z}]^T$ and the orientation of the model body frame relative to the world frame $\mathbf{q}_m \in \mathbb{R}^4$ as a quaternion [58]:

$$M = \begin{bmatrix} -q_2^2 - q_3^2 + q_1^2 + q_4^2 & 2\,q_1q_2 + 2\,q_3q_4 & 2\,q_1q_3 - 2\,q_2q_4 & -r_{m,x} \\ 2\,q_1q_2 - 2\,q_3q_4 & -q_1^2 - q_3^2 + q_2^2 + q_4^2 & 2\,q_1q_4 + 2\,q_2q_3 & -r_{m,y} \\ 2\,q_1q_3 + 2\,q_2q_4 & 2\,q_2q_3 - 2\,q_1q_4 & -q_1^2 - q_2^2 + q_3^2 + q_4^2 & -r_{m,z} \\ 0 & 0 & 0 & 1 \end{bmatrix}. \quad (2.36)$$

Equation 2.36 uses Equation 2.7 to transform the quaternion into a DCM. The model matrix basis vectors are illustrated in Figure 2.4 as M_{i}, with the world frame basis vectors notated with $\boldsymbol{W}_{\text{i}}$. Given the location of the camera origin $\boldsymbol{r}_{cam} \in \mathbb{R}^3$, its target position $\boldsymbol{t}_{cam} \in \mathbb{R}^3$, and the camera up direction $\boldsymbol{u}_{cam} \in \mathbb{R}^3$, the view matrix $V \in \mathbb{R}^{4\times4}$ that transforms from the world frame to the camera frame is given by [58]:

$$\begin{aligned} \boldsymbol{v}_3 &= \frac{\boldsymbol{r}_{cam} - \boldsymbol{t}_{cam}}{\|\boldsymbol{r}_{cam} - \boldsymbol{t}_{cam}\|} \\ \boldsymbol{v}_1 &= \frac{\boldsymbol{u}_{cam} \times \boldsymbol{v}_z}{\|\boldsymbol{u}_{cam} \times \boldsymbol{v}_3\|} \\ \boldsymbol{v}_2 &= \boldsymbol{v}_1 \times \boldsymbol{v}_3 \\ V &= \begin{bmatrix} v_{1,x} & v_{1,y} & v_{1,z} & -\boldsymbol{v}_1 \cdot \boldsymbol{r}_{cam} \\ v_{2,x} & v_{2,y} & v_{2,z} & -\boldsymbol{v}_2 \cdot \boldsymbol{r}_{cam} \\ v_{3,x} & v_{3,y} & v_{3,z} & -\boldsymbol{v}_3 \cdot \boldsymbol{r}_{cam} \\ 0 & 0 & 0 & 1 \end{bmatrix}. \end{aligned} \quad (2.37)$$

The view matrix basis vectors are illustrated in Figure 2.4 as $\boldsymbol{v}_{\text{i}}$. Given the field of view of the camera FOV in radians, the distance from the camera origin to the near n and far f

DISTRIBUTION A: Distribution approved for public release.

clipping planes, and the camera aspect ratio a, the orthographic projection matrix $P \in \mathbb{R}^{4\times4}$ that transforms from the camera frame to the image plane is given by [58]:

$$
\begin{aligned}
t &= n \cdot \tan\left(\frac{FOV}{2}\right) \\
r &= t \cdot a \\
P &= \begin{bmatrix} \frac{2n}{2r} & 0 & 0 & 0 \\ 0 & \frac{2n}{2t} & 0 & 0 \\ 0 & 0 & -\frac{f+n}{f-n} & \frac{2fn}{f-n} \\ 0 & 0 & -1 & 0 \end{bmatrix}
\end{aligned} \tag{2.38}
$$

Together, these matrices form the so-called Model-View-Projection matrix through the matrix product $\mathcal{MVP} = PVM$ which transforms directly from coordinates in the object body frame $\boldsymbol{r}_{\text{obj}}$ to the image plane:

$$
\begin{bmatrix} x_h \\ y_h \\ z_h \\ w_h \end{bmatrix} = \mathcal{MVP} \begin{bmatrix} \boldsymbol{r}_{\text{obj},x} \\ \boldsymbol{r}_{\text{obj},y} \\ \boldsymbol{r}_{\text{obj},z} \\ 1 \end{bmatrix}. \tag{2.39}
$$

In Equation 2.39, x_h/w_h and y_h/w_h are homogeneous coordinates in the image plane, running linearly from $[-1,-1]$ at the top left corner of the image to $[1,1]$ at the bottom right. Given the width of the image in w_{pix} pixels as well as the aspect ratio of the image a, the image coordinates (x, y) of r_{obj} in pixels are:

$$
\begin{bmatrix} x \\ y \end{bmatrix} = \begin{bmatrix} w_{\text{pix}}\left(\frac{1}{2} + \frac{x_h}{2w_h}\right) \\ a \cdot w_{\text{pix}}\left(\frac{1}{2} + \frac{y_h}{2w_h}\right) \end{bmatrix}. \tag{2.40}
$$

The transformation summarized in Eqs 2.39 and 2.40 are crucial in Section 2.1.11.4 for the shadow mapping algorithm used to compute pixel-wise self-shadowing effects.

Many existing light curve simulation methods for nonconvex objects rely on ray tracing schemes like Möller and Trumbore's ray-triangle intersection algorithm [5], [23]. This com-

DISTRIBUTION A: Distribution approved for public release.

putation has complexity $\mathcal{O}(n^2)$ if implemented naively, but can be improved to $\mathcal{O}(n \ln n)$ with better spatial data structures. For human-made space objects, there may be significant self-shadowing at large phase angles. As a result, it cannot be assumed that the self-shadowing conditions $\delta_{\text{ij,ss}}$ and $\delta_{\text{ij,os}}$ are zero [5], [14]. Naïve ray traced shadows generally require $\mathcal{O}(n^2)$ ray-triangle intersections per timestep for n faces. For this reason, ray traced shadows quickly become infeasible for complex objects without GPU parallelization. The limitations of ray-triangle intersections for light curve simulation is discussed at length by Frueh et al. [14].

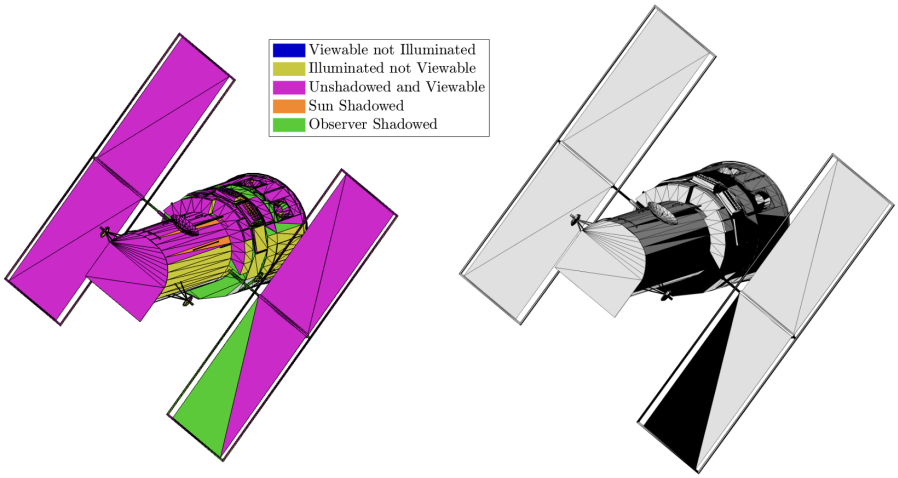

Figure 2.5. Hubble Space Telescope ray traced shadow categorization and shading. Models from [59]

The facet-wise shadow categorization shown in Figure 2.5 informs the μ_{ij} self-shadowing term in Equation 2.34. The major downside of facet-wise shadow categorization is that it is difficult to determine the fraction of each face is illuminated — it categorizes the entire face together, leading to unphysical discontinuities in simulated light curves.

2.1.11.3 The Importance of Self-Shadowing

To motivate the need for accurate shadows when dealing with human-made space objects, consider the error introduced by neglecting shadows for different types of space objects. Kaasalainen and Torppa's work on asteroids reasonably assumed that shadowing was a

DISTRIBUTION A: Distribution approved for public release.

negligible contribution to the measured light curve. Human-made objects do not afford the same luxury. Figure 2.6 displays light curves for the asteroid Bennu and the Hubble Space Telescope with and without accurate shadows under a single-axis spin profile with inertially fixed Sun and observer vectors. Without accurate shadowing, the light curve's intensity and its time derivative can be significantly error-prone.

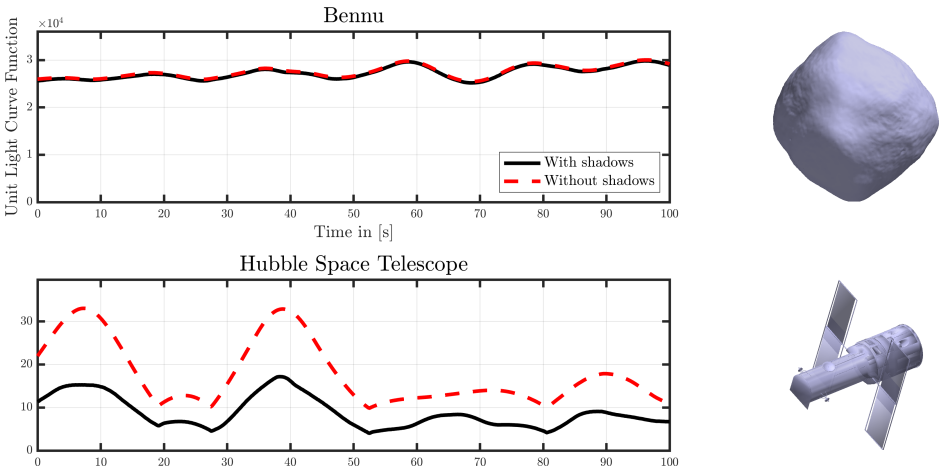

Figure 2.6. Normalized irradiance errors introduced by neglecting shadows for Bennu and HST. Models from [59]

2.1.11.4 Shadow Mapping

Shadow mapping is used in the simulations presented in this work for faster and more accurate self-shadowing. Shadow mapping is a well understood technique in computer graphics [60]. Although modern ray traced shadowing may be more computationally efficient, shadow mapping was selected for its ease of implementation [60]. Shadow mapping shades individual pixel fragments instead of entire faces, offering increasing shadow quality over facewise ray tracing as the number of mesh faces falls.

Given an observer and Sun vector in the body frame of the object, shadow mapping proceeds in a four step process. In step one, a camera is positioned along the Sun vector and a perpendicular depth texture is computed. In the second step, depth values in Sun camera space are transformed to observer camera space, where a second depth texture is computed. This second texture is used to find the closest fragment along each ray to the Sun [61]. Self-

DISTRIBUTION A: Distribution approved for public release.

shadowed fragments are classified as those further from the Sun than the closest fragment along the same ray, indicated in red in Figure 2.7. Fragments that do not pass the convex shadowing condition are horizon shadowed, indicated in blue in Figure 2.7, determining the Sun and observer shadowing conditions at once. All remaining fragments are shaded with using the same Lambertian reflection model in 2.34. Computing the light curve function for the final rendered image requires summing all pixel values and dimensionalizing the result by the area of the observer camera's field of view. The light curve simulation environment used in this work was implemented in C and OpenGL [62].

In order to compute the final shaded and shadowed image, a depth map must be computed from the perspective of two orthographic cameras in the Sun and observer directions. These depth masks require a set of transformations from the model body frame to screen space. With this background laid out, the process for computing a perpendicular depth map $d(x, y)$ from the perspective of an arbitrary orthographic camera is detailed in Algorithm 1.

Algorithm 1 Pixel-wise depth map computation for shadow mapping

$(x, y) \in \mathbb{Z}$	▷ Pixel coordinates on the image plane
$\boldsymbol{r}_{\text{pix}} \in \mathbb{R}^3$	▷ Pixel world coordinates; provided by OpenGL
$d(x, y) \leftarrow (\boldsymbol{r}_{cam} - \boldsymbol{r}_{\text{pix}}) \cdot \boldsymbol{r}_{cam}$	▷ Pixel depth in the camera view direction

The pixel-wise shading process is summarized in Algorithm 4 in Appendix 6.1.1. This shading and shadow mapping procedure is detailed graphically in Figure 2.7.

An image shaded by Algorithm 4 is dimensionalized to a normalized irradiance value by computing the area of the square orthographic field of view given the image pixel count n_{pix}:

$$A_{image} = 2n_{\text{pix}} \left(FOV\right)^2 . \tag{2.41}$$

The field of view FOV must be set dynamically at runtime to account for the size of the 3D model. The pixel values v in the image are stored as unsigned 8 bit integers which take on values from 0 to 255, corresponding to the power range 0 to 1 within the pixel shading procedure described by Algorithm 4. The total normalized irradiance in image j is computed by summing over all n_{pix} pixels, each having a value v_{i}, and dimensionalizing by the area of the image plane:

DISTRIBUTION A: Distribution approved for public release.

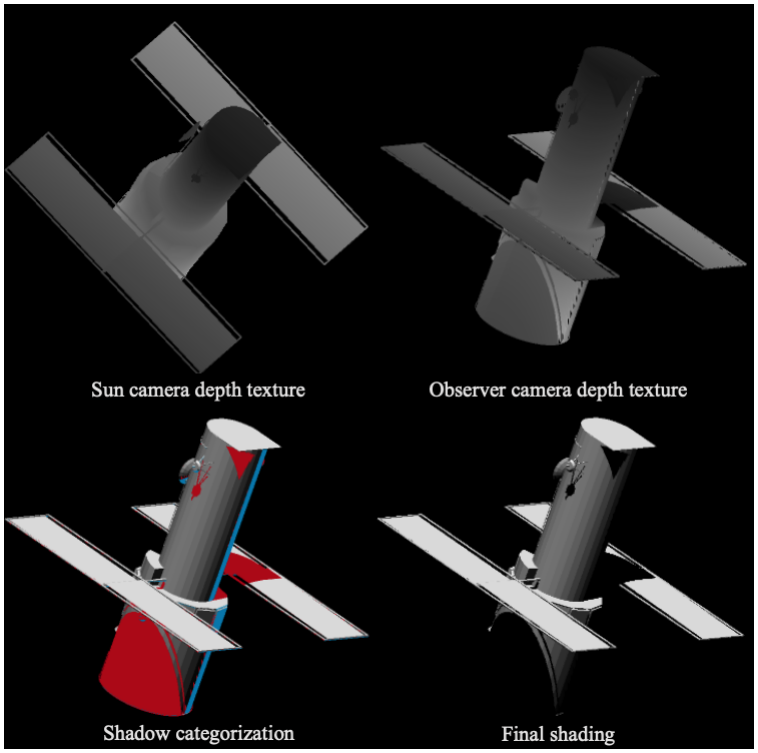

Figure 2.7. Hubble Space Telescope shadow mapping with self (red) and horizon (blue) shadows rendered. Models from [59]

$$\check{I}_{\mathrm{j}} = \frac{A_{image}}{n_{\mathrm{pix}}} \sum_{\mathrm{i}=1}^{n_{\mathrm{pix}}} \frac{v_{\mathrm{i}}}{255} \tag{2.42}$$

2.2 Simulating The Observations

2.3 Time Systems

In order to accurately predict the position of a space object and an observer, it is necessary to understand how a given time translates to the orientation of the relevant reference frames. These calculations require conversions between various time scales, the Julian date, and sidereal time.

DISTRIBUTION A: Distribution approved for public release.

2.3.1 Time Scales

There are a variety of scales used to measure time. What follows is a minimal treatment of each. For a more comprehensive overview, see Section 3.5 of [3]. International Atomic Time (TAI) is based on measurements from atomic clocks and is independent of astronomical effects or observations. By definition, TAI proceeds at the rate of 1 SI second per second. Universal Time (UT0) is derived directly from observations of the apparent position of the stars. UT1 is derived from UT0 by adjusting for polar motion. UT1 is offset from TAI by $\Delta UT1$, which is a dynamic quantity that must be continually observed. Universal Coordinated Time (UTC) is a truncation of UT1 that uses an integer number of leap seconds ΔAT to stay within 0.9 seconds of TAI. Terrestrial Time (TT) is defined by a constant offset of $TT - TAI = 32.184$ seconds from TAI and preceding at the same rate as TAI. These time scale relations are summarized in Equation 2.43.

$$\begin{aligned} UTC &= UT1 - \Delta UT1 \\ TAI &= UTC + \Delta AT \\ TT &= TAI + 32.184^s \end{aligned} \tag{2.43}$$

These time scales are relevant for this research as the precise coordinate frame transformation from ITRF to the J2000.0 realization of ICRF relies on quantities expressed in UT1. Date timestamps are usually standardized to UTC, requiring the transformations in Equation 2.43 for full accuracy. Figure 2.8 shows the evolution of UTC, UT1, and TT with respect to TAI. Notice that $\Delta UT1$ continually changes while ΔAT is always truncated to a nearby integer.

2.3.2 Julian Date

Most tasks in astrodynamics are easier when using a continuous time system. For this reason, the Julian date is adopted. This quantity is defined as the number of days elapsed

DISTRIBUTION A: Distribution approved for public release.

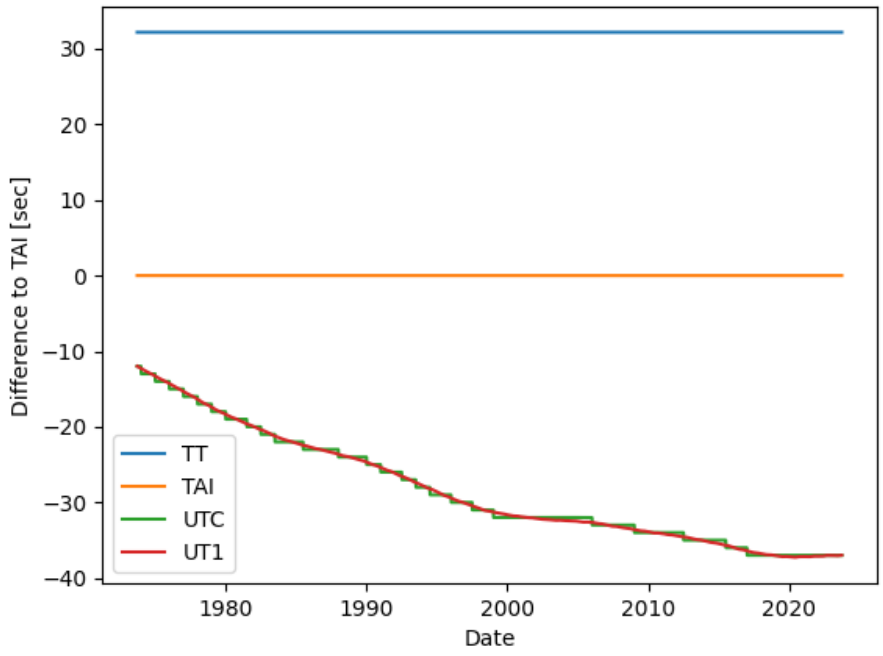

Figure 2.8. Time scales relative to TAI

since January 1, 4713 B.C., at 12:00 [3]. Given a date timestamp of the form D/M/Y h:m:s between the years of 1900 and 2100, the Julian date JD is computed via:

$$JD = 376Y - \text{floor}\left[\frac{7Y + 7 \cdot \text{floor}\left(\frac{M+9}{12}\right)}{4}\right] + \text{floor}\left(\frac{275M}{9}\right) + d + 1721013.5 + \frac{\left(\frac{s}{60}+60\right)}{60} + h}{24}. \tag{2.44}$$

Note that Equation 2.44 is always a function of the time scale used in the input, i. e. a UTC timestamp yields JD_{UTC} whereas a UT1 timestamp yields JD_{UT1}. Another useful quantity for later time and coordinate system calculations is the number of Julian centuries since a particular epoch, T. The J2000.0 epoch is used unless otherwise stated, resulting in [3]:

$$T = \frac{JD - 2451545.0}{36535}. \tag{2.45}$$

DISTRIBUTION A: Distribution approved for public release.

Often, more specificity is needed with respect to the time scale used in Equation 2.45. For example, computing T with an input date in UT1 yields T_{UT1} using JD_{UT1}, which is in turn a function of a date expressed in UT1.

2.3.3 Solar and Sidereal Time

A solar day is defined as the time required for the Sun to pass and return to an observer's meridian — a line of constant longitude extending from the geographic south pole to the geographic north pole [3]. By contrast, a sidereal day is the time required for the stars to complete a revolution around an observer's meridian. Due to the Earth's orbit around the Sun, the sidereal day is about 4 minutes shorter than the solar day [3]. The Greenwich mean sidereal time (GMST) θ_{GMST} is computed in seconds via [4]:

$$\theta_{\text{GMST}} = 67310.54841 + \left(3.15576 \cdot 10^9 + 8640184.812866\right) T_{UT1} + 0.093104 T_{UT1}^2 - 6.2 \cdot 10^{-6} T_{UT1}^3. \tag{2.46}$$

Accounting for the variations in the inclination of the ecliptic ϵ and the change in the equinox compared to the reference epoch $\Delta\Psi$ produces Greenwich apparent sidereal time (GAST) θ_{GAST} via [4]:

$$\theta_{\text{GAST}} = \theta_{\text{GMST}} + \Delta\Psi \cos\epsilon. \tag{2.47}$$

Both the inclination of the ecliptic and the difference in the equinox are computed with series expansions following the IAU 1980 theory of nutation [3].

2.4 Coordinate Systems

A precise definition of coordinate systems is necessary for determining the position of the observer and the observed space object at a given time. The relevant conversions are summarized by a single question: how is a fixed position on the surface of the Earth transformed into a standardized inertial reference frame?

DISTRIBUTION A: Distribution approved for public release.

2.4.1 Latitude, Longitude and Altitude

Latitude, longitude, and altitude (LLA) is a spherical representation of position on or above the surface of the Earth. For the purposes of precise station positioning, the difference between the two types of longitude — geocentric and geodetic — is important. Geocentric latitude is the angle between the line from the center of mass of the Earth to the position of interest and the equatorial plane. Geodetic latitude instead measures the angle between the local ellipsoid surface normal and the equatorial plane. Geodetic latitude ϕ_{geod} is converted to geocentric ϕ_{geoc} latitude using the flattening ratio of the ellipsoid f with [4]:

$$\phi_{\text{geoc}} = \tan^{-1}\left((1-f)^2 \tan\phi_{\text{geod}}\right). \tag{2.48}$$

Additionally, the radius of the ellipsoid r_E at a given geocentric latitude is a function of the equiatorial radius of the Earth ellipsoid R_E and is necessary for later conversions, expressed by [4]:

$$r_E = R_E - f\sin^2\left(\phi_{\text{geoc}}\right). \tag{2.49}$$

The altitude in a set of LLA coordinates needs a reference point. Different observers may be defined differently — either relative to the approximate ellipsoidal shape of the Earth, the hypothetical mean sea level, or the surrounding terrain.

2.4.1.1 Ellipsoid

Due to Earth's equatorial bulge, it is common to model the rough shape of the Earth as an ellipsoid. In particular, the 1984 World Geodetic Survey (WGS-84) model is used throughout this work to define the shape of the Earth ellipsoid, with parameters listed in Table 2.2 for use in Eqs 2.48 and 2.49.

Parameter	**Value**
Equatorial radius R_E	6378.137 $[km]$
Flattening ratio f	1/298.257

Table 2.2. WGS-84 ellipsoid model of the Earth [3].

DISTRIBUTION A: Distribution approved for public release.

These parameters are needed for the conversion from LLA to the International Terrestrial Reference Frame.

2.4.1.2 Geoid

The geoid accounts for the gravitational potential differences across the Earth's surface [3]. It is a surface of equal gravitational potential; the surface the ocean relaxes to without the influence of the wind and tides [3]. For this reason, the geoid is alternatively known as the mean sea level (MSL). The ellipsoid is a good approximation of the geoid, which deviates from the ellipsoid by less than ≈ 100 meters at all latitudes and longitudes. The height of the geoid above the ellipsoid can be computed from a high-fidelity gravity model, but it is often more convenient to interpolate a pre-computed grid of geoid heights. Figure 2.9 displays global geoid heights derived from the 1996 Earth Gravitational Model (EGM-96) relative to the ellipsoid.

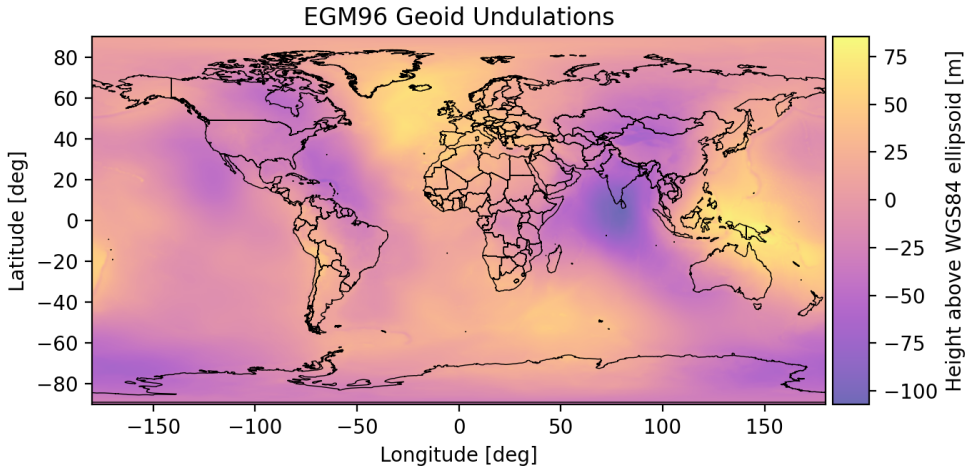

Figure 2.9. EGM-96 geoid heights above the WGS-84 ellipsoid

2.4.1.3 Terrain

Terrain elevation is usually the final component needed to fully define the altitude of a ground station, which is often defined relative to MSL. This work uses 30-meter terrain tiles

DISTRIBUTION A: Distribution approved for public release.

from the Shuttle Radar Topography Mission (SRTM). Figure 2.10 shows the local elevation around the Purdue Optical Ground Station using SRTM data.

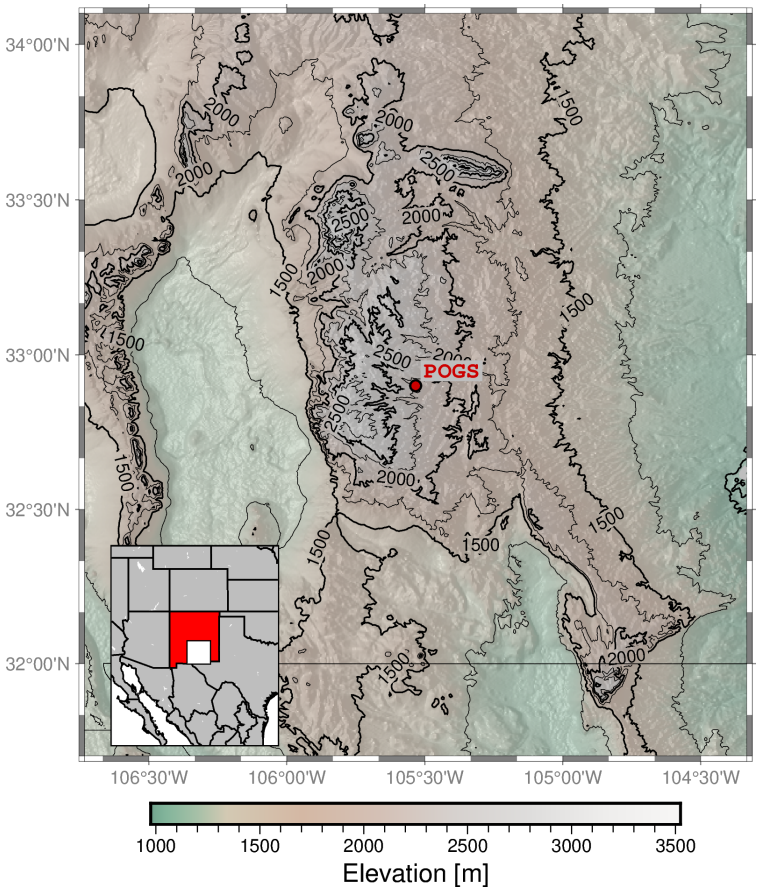

Figure 2.10. MSL elevations surrounding the Purdue Optical Ground Station

2.4.1.4 Altitude Conversions

Given an altitude relative to the terrain a_{terrain}, the elevation above the ellipsoid a_{ellip} is given as a function of the terrain elevation above the geoid $h_{\text{terrain}}(\lambda, \phi_{\text{geod}})$ and the geoid elevation above the ellipsoid $h_{\text{geoid}}(\lambda, \phi_{\text{geod}})$, each evaluated at a given geodetic latitude ϕ_{geod} and longitude λ, yielding [3]:

$$a_{\text{ellip}} = a_{\text{terrain}} + h_{\text{terrain}}(\lambda, \phi_{\text{geod}}) + h_{\text{geoid}}(\lambda, \phi_{\text{geod}}). \tag{2.50}$$

DISTRIBUTION A: Distribution approved for public release.

2.4.2 International Terrestrial Reference Frame (ITRF)

The Cartesian form of LLA is known as the Earth-centered Earth-fixed (ECEF) reference frame. Throughout this work, ECEF and ITRF will be used interchangeably. This frame has its origin at the center of mass of the Earth and its axes fixed in the crust. The fundamental plane of the frame is defined to be the equator — orienting the z-axis through Earth's instantaneous spin axis, and the reference direction through the intersection of the prime meridian and the equator — defining the x-axis. Completing the right-handed system with $\hat{\boldsymbol{y}} = \hat{\boldsymbol{z}} \times \hat{\boldsymbol{x}}$ yields a reference frame that remains fixed, neglecting effects like continental drift. The transformation from LLA $(\lambda, \phi_{\text{geod}}, a_{\text{ellip}})$ to a position vector $\boldsymbol{r}_{\text{itrf}} = [x_{\text{itrf}}, y_{\text{itrf}}, z_{\text{itrf}}]^T$ in ITRF is given by [3]:

$$
\begin{aligned}
\mathrm{e}^2 &= 2f - f^2 \\
N &= \frac{R_E}{\sqrt{(1 - \mathrm{e}^2 \sin(\phi_{\text{geod}})^2)}} \\
\rho &= (N + a_{\text{ellip}}) \cos(\phi_{\text{geod}}) \\
x_{\text{itrf}} &= \rho \cos(\lambda) \\
y_{\text{itrf}} &= \rho \sin(\lambda) \\
z_{\text{itrf}} &= \Big(N(1 - \mathrm{e}^2) + a_{\text{ellip}}\Big) \sin(\phi_{\text{geod}}).
\end{aligned}
\tag{2.51}
$$

In Equation 2.51, e^2 is the squared eccentricity of the ellipsoid as a function of the flattening coefficient f, N is the radius of curvature in the meridian, and ρ is the $x-y$ plane magnitude of the station's position [3].

Many later transformations require the body axis rotation matrices R_1, R_2, and R_3 which are expressed as a function of an angle θ:

DISTRIBUTION A: Distribution approved for public release.

$$
\begin{aligned}
R_1(\theta) &= \begin{bmatrix} 1 & 0 & 0 \\ 0 & \cos\theta & \sin\theta \\ 0 & -\sin\theta & \cos\theta \end{bmatrix} \\
R_2(\theta) &= \begin{bmatrix} \cos\theta & 0 & -\sin\theta \\ 0 & 1 & 0 \\ \sin\theta & 0 & \cos\theta \end{bmatrix} \\
R_3(\theta) &= \begin{bmatrix} \cos\theta & \sin\theta & 0 \\ -\sin\theta & \cos\theta & 0 \\ 0 & 0 & 1 \end{bmatrix}.
\end{aligned} \tag{2.52}
$$

2.4.3 Topocentric East North Up (ENU) Reference Frame

The remaining transformations in this chapter will only be defined in terms of their rotation matrices. It is often useful to express observations in a local reference frame. The East North Up (ENU) coordinate system is used throughout this work. This system has an origin at the observing station, with the first two basis vectors pointing towards the local East and North and the third pointing towards zenith. The transformation from a vector $\boldsymbol{r}_{\text{itrf}}$ in ITRF to $\boldsymbol{r}_{\text{enu}}$ in ENU is a function of the longitude of the station λ and the geocentric latitude ϕ_{geoc} by [4]:

$$
\boldsymbol{r}_{\text{enu}} = F_2 F_1 R_2(\phi_{\text{geoc}}) R_3(\lambda) \boldsymbol{r}_{\text{itrf}}. \tag{2.53}
$$

In Equation 2.53, R_3 is a rotation about the third body axis, F_1 swaps the second and third unit vectors, and F_2 swaps the first and third unit vectors. The orientation of the ENU reference frame at the Purdue Optical Ground Station is depicted in Figure 2.11.

DISTRIBUTION A: Distribution approved for public release.

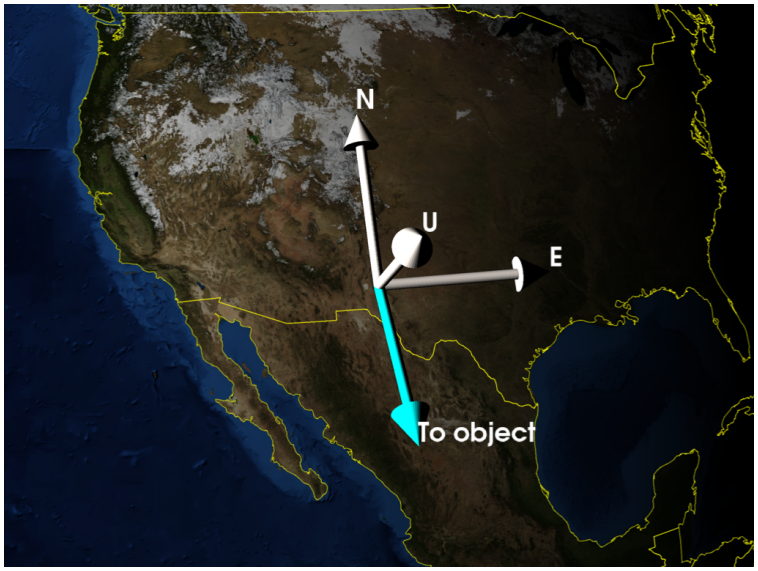

Figure 2.11. ENU reference frame orientation at Purdue Optical Ground Station

2.4.4 International Celestial Reference Frame (ICRF/J2000)

Transforming from ITRF to a standardized inertial reference frame is an involved process due to the variety of nonlinear effects impacting the Earth's rotational motion. In total, this transformation must account for polar motion, the nutation and precession of the Earth's pole, and the mean sidereal time. These transformations are treated much more thoroughly in Montenbruck and Gill [63].

Accounting for polar motion — the motion of the Earth's pole that cannot be explained through nutation theory — transforms from $\boldsymbol{r}_{\text{itrf}}$ in ITRF to $\boldsymbol{r}_{\text{gtod}}$ in Greenwich True of Date (GTOD) via [3]:

$$\boldsymbol{r}_{\text{gtod}} = R_1(y_p)R_2(x_p)\boldsymbol{r}_{\text{itrf}}, \tag{2.54}$$

where x_p and y_p are the angular components of the polar motion at the time of interest [4]. Accounting for the sidereal rotation of the Earth about its pole transforms from $\boldsymbol{r}_{\text{gtod}}$ in GTOD to $\boldsymbol{r}_{\text{teme}}$ in the True Equator, Mean Equinox (TEME) reference frame via [4]:

DISTRIBUTION A: Distribution approved for public release.

$$\boldsymbol{r}_{\text{teme}} = R_3(-\theta_{\text{GMST}})\boldsymbol{r}_{\text{gtod}}, \tag{2.55}$$

where θ_{GMST} is the Greenwich mean sidereal time. Accounting for the difference between GMST and GAST at the date of interest transforms $\boldsymbol{r}_{\text{teme}}$ TEME to $\boldsymbol{r}_{\text{tod}}$ in the True of Date (TOD) reference frame via [3]:

$$\boldsymbol{r}_{\text{tod}} = R_3(-\Delta\Psi \cos\epsilon)\boldsymbol{r}_{\text{teme}}, \tag{2.56}$$

where $\Delta\Psi$ is the angular difference in the longitude of the vernal equinox between GMST and GAST, and ϵ is the true inclination of the ecliptic [3]. Accounting for the nutation of Earth's pole transforms $\boldsymbol{r}_{\text{tod}}$ from TOD to $\boldsymbol{r}_{\text{mod}}$ in the Mean of Date (MOD) reference frame via [3]:

$$\boldsymbol{r}_{\text{mod}} = R_1(-\bar{\epsilon})R_3(\Delta\Psi)R_1(\bar{\epsilon} + \Delta\epsilon)\boldsymbol{r}_{\text{tod}}, \tag{2.57}$$

where $\bar{\epsilon}$ is the mean inclination of the ecliptic at the time of interest, and ϵ is the true inclination of the ecliptic [3].

Accounting for the secular precession of Earth's pole transforms $\boldsymbol{r}_{\text{mod}}$ from MOD to $\boldsymbol{r}_{\text{icrf}}$ in ICRF via [3]:

$$\boldsymbol{r}_{\text{icrf}} = R_3(\zeta)R_2(\theta)R_3(z)\boldsymbol{r}_{\text{mod}}, \tag{2.58}$$

through the 3-2-3 Euler angle sequence (z, θ, ζ). Each of these angles modeling the precession are a function of the date of the transformation, and are approximated by polynomial expansions in the Julian century T [4].

The specific realization of ICRF used in this work is referenced to the position of the equator and equinox at the J2000.0 epoch (January 1, 2000 12:00:00.000 TT), leading to the common name for this reference frame, "J2000" [3].

DISTRIBUTION A: Distribution approved for public release.

2.4.5 Right Ascension and Declination

Right ascension and declination, often shortened to RA/Dec, are useful angles for describing the angular position of an object on the celestial sphere from the perspective of an observer. As such, RA/Dec values are inertial, but can be defined relative to a topocentric observer or the center of the Earth [4]. The topocentric RA/Dec is exclusively used in this work for later simulations. Right ascension is defined as the angle of the observation projected onto the inertial $x-y$ plane, measured counterclockwise from inertial $\hat{\boldsymbol{x}}$, represented by α. Declination is the angle from the $x-y$ plane to the observation with positive values above the $x-y$ plane (closer to inertial z) and negative values below. Declination is represented by δ. Given a vector direction $[x_{\text{itrf}}, y_{\text{itrf}}, z_{\text{itrf}}]^T$ in J2000, the corresponding J2000 RA/Dec is computed via [4]:

$$\begin{bmatrix} \alpha \\ \delta \end{bmatrix} = \begin{bmatrix} \text{atan2}(y_{\text{itrf}}, x_{\text{itrf}}) \\ \text{atan2}(z_{\text{itrf}}, \sqrt{x_{\text{itrf}}^2 + y_{\text{itrf}}^2}) \end{bmatrix}. \tag{2.59}$$

2.4.6 Azimuth and Elevation

Azimuth and elevation, often shortened to Az/El, are similar angular quantities to right ascension and declination [4]. Instead of being based on the inertial sphere, they are referenced to an arbitrary reference frame. For a telescope making observations of an object, the local topocentric ENU frame may be used. For a satellite star tracker, star azimuth and elevation might be reported in the satellite body frame. In either case, Equation 2.59 can be repurposed in terms of Az/El, where a vector $[x_{\text{enu}}, y_{\text{enu}}, z_{\text{enu}}]^T$ is expressed in the frame of interest [4].

$$\begin{bmatrix} Az \\ El \end{bmatrix} = \begin{bmatrix} \text{atan2}(y_{\text{enu}}, x_{\text{enu}}) \\ \text{atan2}(z_{\text{enu}}, \sqrt{x_{\text{enu}}^2 + y_{\text{enu}}^2}) \end{bmatrix} \tag{2.60}$$

Note that Equation 2.60 references azimuth to the x-axis, proceeding in the counterclockwise direction. Often, this reference axis and direction may be changed depending on the reference frame being used. For example, ground station observations may be referenced

DISTRIBUTION A: Distribution approved for public release.

to local North — the second axis of the ENU system — proceeding clockwise. This would require the substitution $Az' = \frac{\pi}{2} - Az$. Notice that this substitution leads to Az' leaking outside the domain of $[0, 2\pi)$. This is not an issue for later coordinate transformations but may be undesirable for plots. Wrapping the result back to the standard azimuth range via $Az_{wrapped} = \text{mod}(Az, 2\pi)$ is a sufficient fix.

2.4.7 Coordinate Transformations Summary

With these transformations, any topocentric observation directions in RA/Dec or Az/El can be converted into a Cartesian representation and transformed into J2000. Simultaneously, any propagated space object orbits can be transformed similarly from an arbitrary propagation frame such that all future computations requiring the observation geometry take place in the same reference frame.

2.4.8 Planetary Ephemerides

The Spacecraft, Planet, Instrument, C-matrix, and Events (SPICE) toolkit is used for the propagation of the Sun and Moon throughout the results presented in this work [64]. SPICE is maintained by the NASA Jet Propulsion Laboratory's Navigation and Ancillary Information Facility (NAIF) and provides the state of the art solutions for the positions and orientations of solar system bodies [64]. All calculations of $\boldsymbol{r}_{\text{sun}}$ and $\boldsymbol{r}_{\text{moon}}$ rely on queries to SPICE using the DE440s planetary ephemeris files.

2.5 The Charge Coupled Device (CCD)

Many optical telescopes, including the Purdue Optical Ground Station, use a CCD to convert incident photons into a digital signal on a pixel grid [9]. CCDs accomplish this with a matrix of semiconductor pixel wells which collect electrons released by the photoelectric effect when photons are incident on that pixel [9]. The release of these photoelectrons is wavelength dependent and is captured by the quantum efficiency spectrum of a given CCD. Developing this background in photometry is useful for both light curve simulation as well as simulating the CCD camera measuring that light curve.

DISTRIBUTION A: Distribution approved for public release.

Due to the sheer distance from the observer to any space object, taking an image that resolves the object's geometry is generally impossible. For an observer with the pixel scale of the Purdue Optical Ground Station ($s_{\text{pix}} = 0.72$ arcseconds per pixel), a 6U CubeSat in LEO occupies about 1/44 of a pixel area, while a large communications satellite in GEO occupies approximately 1/13 of a pixel area. In either case, no geometric information is left on the image plane even before diffraction is taken into account.

Whenever an optical telescope is observing an unresolved space object, the object's signal is necessarily superimposed on whatever signals exist in the background as the unresolved signal spreads much farther than the object's actual geometric bounds. In this context, background does not only refer to sources physically further than the object — as light can easily enter optical path through atmospheric scattering — but all sources that impact the image apart from the object signal. Some of these sources even originate within the telescope optics and its sensor. To faithfully simulate a telescope observing an object, many position-based SDA tasks are able to ignore background effects while acquiring or tracking objects. For photometry-based SDA, the background is critical. The overall noise floor can be broken up into background signal sources and sensor effects.

2.5.1 Diffraction

Many objects of interest are far past LEO, making optical observations diffraction limited. Diffraction is always occurring when observing an object at any distance through any optics, but it begins to dominate when the object's scale is equal or smaller than the Rayleigh criterion [4].

2.5.1.1 Rayleigh Criterion

The Rayleigh criterion states that light of wavelength λ will spread into a diffraction pattern with the first minimum of the distribution at an angular radius θ_R when passing through a circular aperture of diameter d [4] such that:

DISTRIBUTION A: Distribution approved for public release.

$$\sin\theta_R = \frac{1.22\lambda}{d}, \qquad \theta_R \approx \frac{1.22\lambda}{d}. \tag{2.61}$$

For a 0.5-meter aperture optical telescope with a pixel scale of 1 arcsecond per pixel, observing a 40-meter wide object in GEO — occupying approximately 0.2 pixel widths on the image — Equation 2.61 predicts that the diffraction pattern will be 2.4 times wider than the object at a wavelength of 550 nanometers. Similarly, a 60-centimeter wide object in LEO observed with the same telescope occupies 0.1 pixel widths in the image while producing an Airy disk 4.5 times wider than the object itself. As a result, GEO objects cannot be resolved from the ground, independent of atmospheric effects.

2.5.1.2 The Airy Disk

The far-field diffraction pattern produced by a point source is known as an Airy pattern or disk [4]. The Airy disk is expressed in terms of an amplitude C at an angular distance θ from the center $C(\theta)$ [4] as:

$$C_{\text{airy}}(\theta) = C_0 \left(\frac{2J_1(k \cdot r_d \sin\theta)}{k \cdot r_d \sin\theta} \right). \tag{2.62}$$

In Equation 2.62, C_0 is the amplitude of the center of the Airy disk, r_d is the radius of the aperture, $k = \frac{2\pi}{\lambda}$ is the wavenumber, and J_1 is the first order Bessel function of the first kind. The central magnitude C_0 is expressed:

$$C_0 = \frac{S_{\text{obj}}^2 A_{\text{aperture}}^2}{2f^4}. \tag{2.63}$$

In Equation 2.63, S_{obj} is the total mean irradiance incident on the CCD due to the source, A_{aperture} is the aperture area, and f is the focal length of the optics [4]. The pattern produced by Equation 2.62 is depicted in Figure 2.12.

DISTRIBUTION A: Distribution approved for public release.

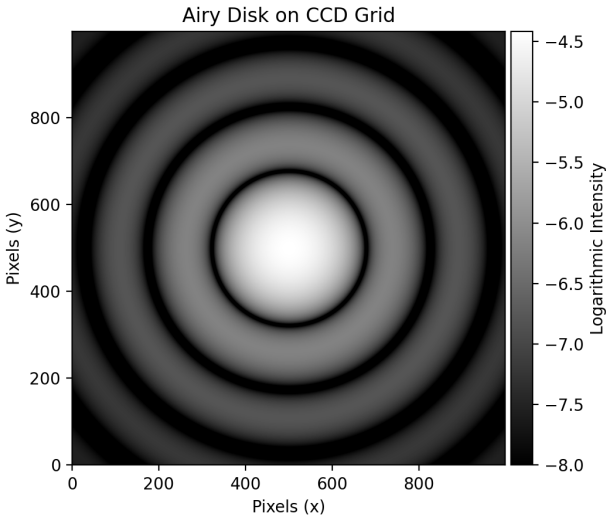

Figure 2.12. Airy disk diffraction pattern

The Rayleigh criterion expresses the angular size of the first zero of the Airy disk, after which the amplitude of the Airy disk drops off exponentially. It is often useful to approximate the Airy disk with a 2D Gaussian. Given the total signal to be approximated, this Gaussian is fit with a single parameter — the full width at half maximum (FWHM). The FWHM expresses the diameter at which the signal drops to half the magnitude of its central maximum [4]. The FWHM of the Airy disk is expressed as a function of the radius of the aperture r_d and the incident wavelength λ [4]:

$$\text{FWHM}_{\text{airy}} = \frac{1.028\lambda}{2r_d}. \tag{2.64}$$

The diffraction pattern is not the only effect that spreads the unresolved signal over the pixel grid. Atmospheric turbulence contributes to further spreading and speckling of the signal [4]. This effect — known as the *seeing* — is encapsulated in $\text{FWHM}_{\text{seeing}}$ and is generally between 1 and 3 arcseconds [4]. While the seeing and diffraction pattern FWHMs are additive, it is sufficient to take the larger value for simulation purposes [4]. The standard deviation σ of the Gaussian approximation of the Airy disk is given as a function of only the FWHM:

DISTRIBUTION A: Distribution approved for public release.

$$\sigma = \frac{\text{FWHM}}{2\sqrt{2\ln 2}}. \tag{2.65}$$

The full Gaussian approximation at an angular distance θ from the source, $C_{\text{gauss}}(\theta)$, is given as a function of the total mean signal $\bar{C}_{\text{all}}$, the variance of the Gaussian σ^2:

$$C_{\text{gauss}}(\theta) = \frac{0.838\bar{C}_{\text{all}}}{2\pi\sigma^2} \exp\left(-\frac{\theta^2}{2\sigma^2}\right) \tag{2.66}$$

In practice, computing the Airy disk or its Gaussian approximation on rectangular pixel grid amounts to integrating the amplitude function $C(\theta)$ over the pixel area, yielding $C_{\text{pix}}(x, y)$, the total signal contained in pixel (x, y):

$$C_{\text{pix}}(x, y) = \int_x^{x+\Delta x} \int_y^{y+\Delta y} C_{\text{gauss}}(\theta(x, y))\, dy\, dy. \tag{2.67}$$

The area within the first maximum of the Airy disk is a function of the pixel scale s_{pix}, the aperture area A_{aperture}, and the incident wavelength λ as [4]:

$$A_{\text{airy}} = \pi\left(\frac{648000/\pi}{s_{\text{pix}}} \sin^{-1}\left(\frac{1.22\lambda}{A_{\text{aperture}}}\right)\right)^2. \tag{2.68}$$

2.5.2 Signal-to-Noise Ratio

Because the unresolved object signals are always superimposed on the background of the image, the signal-to-noise ratio (SNR) of a CCD is expressed with the signal S_{obj} included in the denominator noise term N [4]:

$$SNR = \frac{S_{\text{obj}}}{\sqrt{S_{\text{obj}} + N}}. \tag{2.69}$$

Explicitly, the SNR for a signal spread over n_{pix} pixels is expanded in terms of the signal means S_{obj} and variances for the background $\lambda_{\text{background}}$ as well as the sensor noise terms λ_{dark} for intergration noise, σ^2_{read} for read noise, and $\frac{g^2}{24}$ for the truncation noise noise, assuming that their respective probability density functions are independent [4]:

DISTRIBUTION A: Distribution approved for public release.

$$SNR = \frac{S_{\text{obj}}}{\sqrt{S_{\text{obj}} + n_{\text{pix}}\left(\lambda_{\text{background}} + \lambda_{\text{dark}} + \sigma^2_{\text{read}} + \frac{g^2}{24}\right)}}. \tag{2.70}$$

It should be noted that the SNR computed in Equation 2.70 is idealized. In reality, the discrete sampling of each random variable in each object pixel — as well as the Poisson sampling of the object signal — results in a slightly different value. As the number of object pixels approaches infinity, the SNR computed from the image would approach the theoretical value. Figure 2.13 illustrates the effect of raising the background noise level while holding the object signal constant on the SNR.

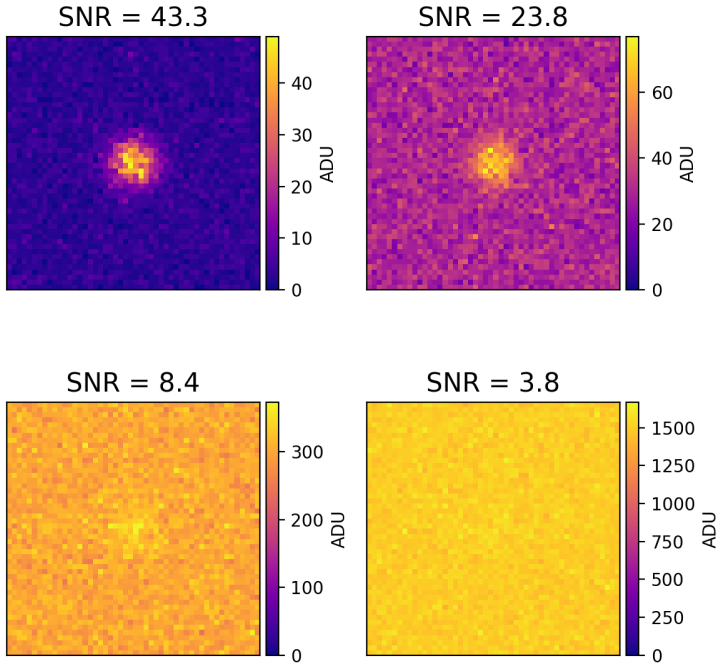

Figure 2.13. Signal-to-noise ratio reduction on a synthetic CCD pixel grid

The SNR is an important constraint when determining whether an object signal is visible above the background. If the SNR is too low, it becomes difficult or impossible to notice and quantify the object signal. Simulations in this work are all performed with a reasonable SNR limit of 3.

DISTRIBUTION A: Distribution approved for public release.

2.5.3 Telescope Properties

While much of the focus in this work is directed towards the CCD, the telescope it is mounted within has a few important properties which must be known for accurate CCD simulation.

The aperture of the telescope is the beginning of the optical path within the telescope — the area that collects incoming light. The area of the aperture $A_{\text{aperture}} = \pi r_d^2$, where r_d is the radius of the aperture must be distinguished from the *effective* aperture area, which is the total area of the aperture which actually collects light. Some telescopes have central obstructions which remove an amount of aperture area from the optical path, such that the effective aperture area is:

$$A_{\text{eff}} = A_{\text{aperture}} - \pi r_o^2, \tag{2.71}$$

where r_o is the radius of the obstruction. The telescope focal length f is the length of the optical path within the optics required to resolve a focused image. The pixel scale s_{pix} is a measure of the angle spanned by the side length of each square pixel, often expressed in arcseconds per pixel.

2.5.4 Brightness Units

In the context of photometry, "brightness" is a catch-all term for a variety of units. Defining the relationships between these units will make later light curve conversions more clear. Brightness conversions are needed for both light curves and the environmental data sources that drive the CCD performance model described in Section 2.5.

2.5.4.1 S_{10} Surface Brightness

While apparent magnitude and irradiance are effective for quantifying the flux of point sources, other units exist to describe diffuse or extended sources where brightness is spread over an area. S_{10} is a unit of surface brightness representing the number of 10th magnitude stars per square degree that would produce the same flux as a given diffuse source. Surface

DISTRIBUTION A: Distribution approved for public release.

brightness in S_{10} over a given solid angle Ω $[sr]$ can be converted to total irradiance I $\left[\frac{W}{m^2}\right]$ via [9]:

$$\frac{I}{S_{10}} = 10^{-10/2.5}\left(\Omega\frac{180^2}{\pi^2}\right)\int_{10^{-8}}^{10^{-6}} \mathcal{ZM}(\lambda)\, d\lambda = 8.26617\Omega \cdot 10^{-9}. \tag{2.72}$$

In 2.72, $\mathcal{ZM}(\lambda)$ $\left[\frac{W}{m^2 \cdot m}\right]$ is the representative spectrum of a 0th magnitude star, QE(λ) is the quantum efficiency spectrum of the observing sensor, ATM(λ) is the atmospheric transmission spectrum, λ $[m]$ is wavelength, h $\left[\frac{m^2 \cdot kg}{s}\right]$ is Plank's constant, and c $\left[\frac{m}{s^2}\right]$ is the speed of light in vacuum. Quantum efficiency has units of photoelectrons, conveying the fraction of incident photons converted to photoelectrons in the CCD sensor. Atmospheric transmission is a unitless quantity conveying the fraction of light that is not absorbed by the atmosphere. Example spectra for ATM(λ) and QE(λ) are displayed in Figure 2.15, with underlying data provided in Appendix 6.2.0.1.

2.5.4.2 Magnitude per Square Arcsecond

A second surface brightness unit is $\left[\frac{mag}{arcsec^2}\right]$, also known as MPSAS (magnitude per square arcsecond) [9]. This quantity can be thought of as a generalized S_{10}, where instead of quantifying the number of stars of a certain magnitude in a solid angle, the equivalent magnitude of a single point source is measured. A surface brightness B_{10} in S_{10} can be converted into surface brightness B_{mag} in $\left[\frac{mag}{arcsec^2}\right]$ by applying Equation 2.31.

$$B_{\text{mag}} = -2.5\log_{10}\left(\frac{B_{10} \cdot 10^{-4}}{12960000}\right). \tag{2.73}$$

In Equation 2.73 B_{10} is converted to the total irradiance per square degree, converted square degrees to square arcseconds, and finally transformed into apparent magnitude. B_{mag} in MPSAS is converted to irradiance per steradian — radiance R — using 2.31 and the total solar irradiance I_s via:

$$R = \left(\frac{180}{3600\pi}\right)^2 I_s \cdot 10^{-0.4B_{\text{mag}}}. \tag{2.74}$$

DISTRIBUTION A: Distribution approved for public release.

2.5.4.3 Candela

Some light pollution datasets are given in units that include candela. Candela is the SI base unit of luminous intensity defined by the International Committee for Weights and Measures as "fixing the numerical value of the luminous efficacy of monochromatic radiation of frequency $540 \cdot 10^{12}$ Hz to be equal to exactly 683" [65]. This means that an isotropic green light source with frequency $540 \cdot 10^{12}$ Hz ($\lambda = 555$ nm) has a luminous efficacy of $K_{\text{cd}} = 683\ [lm/W]$ where lm stands for lumens. Luminous efficacy itself determines how well a source produces visible light. For a given wavelength, candela B_{cd} is converted to watts per steradian B_{wsr} via [65]:

$$B_{\text{wsr}}(\lambda) = \frac{B_{\text{cd}}}{K_{\text{cd}}(\lambda)}. \tag{2.75}$$

The luminous efficiency function $K_{\text{cd}}(\lambda)$ models the human eye's response to the visible spectrum [66]. Different fits of this function exist; the function proposed by Sharpe et al. is adopted, displayed in Figure 2.14 [66].

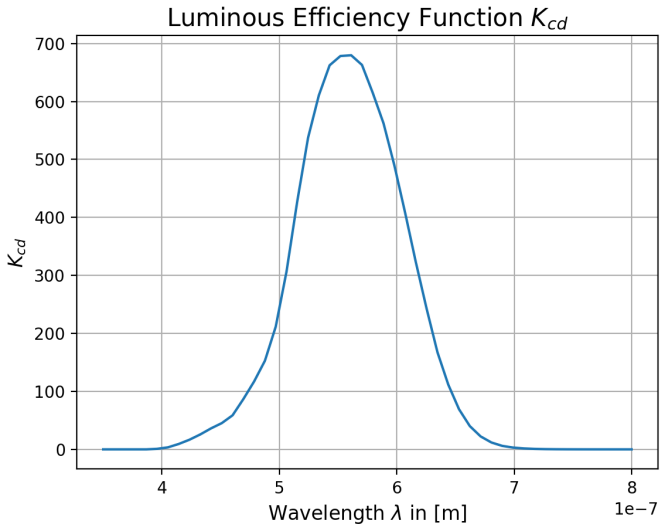

Figure 2.14. Luminous efficiency function from [66]

Candela per unit area can be converted into MPSAS as $B_{\text{mag}}(\lambda)$ by combining Equation 2.75 with 2.30, yielding a formulation which is still a function of the source's wavelength:

DISTRIBUTION A: Distribution approved for public release.

$$B_{\text{mag}}(\lambda) = -2.5 \log_{10} \left(\frac{B_{\text{cd}}}{\left(\frac{180}{3600\pi}\right)^2 K_{\text{cd}}(\lambda) I_s} \right). \tag{2.76}$$

2.5.4.4 Photoelectron Counts

Accurately simulating measured light curves requires an accurate simulation of the CCD camera taking the image. The first step towards that is understanding how irradiance at the telescope aperture is converted into pixel values in the final image. Raw images taken by a CCD-equipped telescope have pixel values measured in photoelectron counts, otherwise known as Analog-to-Digital Units (ADU) [9]. The count in a single pixel obtained is directly proportional (via the CCD's gain) to the number of photons incident on that pixel during the integration time [9]. Higher order effects in the silicon of the CCD renders this description incomplete, but for non-resolved imaging applications concerned about, effects smaller than the sensor readout noise and dark current can be safely neglected [4]. Irradiance can be converted to ADU via the conversion factor $\mathcal{S}_{\text{int}}$ through [9]:

$$\mathcal{S}_{\text{int}} = A_{\text{eff}} \int_{10^{-8}}^{10^{-6}} \left(\frac{\text{sun}(\lambda)}{I_s} \right) \cdot \text{QE}(\lambda) \cdot \text{ATM}(\lambda) \cdot \left(\frac{\lambda}{hc} \right) \, d\lambda. \tag{2.77}$$

In Equation 2.77, $\text{sun}(\lambda)$ is the spectrum of solar irradiance in $\left[\frac{W}{m^2 \cdot m}\right]$, I_s is the irradiance of the Sun, generally taken to be the solar constant 1361 $\left[\frac{W}{m^2}\right]$, and A_{eff} is the effective aperture area. Read literally, the integral term has units $\left[\frac{1}{Ws}\right]$, giving the number of counts per incident Watt of solar radiation and second of integration time. The aperture diameter factor outside the integral accounts for the area of light incident on the CCD, giving $\mathcal{S}_{\text{int}}$ units of $\left[\frac{m^2}{Ws}\right]$. The spectra in Equation 2.77 are plotted in Figure 2.15 with data in Appendix 6.2. Multiplying by irradiance in $\left[\frac{W}{m^2}\right]$ and an integration time Δt in seconds will yield the mean photoelectron signal $\bar{C}_{\text{all}}$ in ADU via:

$$\bar{C}_{\text{all}} = \mathcal{S}_{\text{int}} \cdot I \cdot \Delta t. \tag{2.78}$$

DISTRIBUTION A: Distribution approved for public release.

For completeness, irradiance can be recovered from a signal in ADU and the integration time:

$$I = \frac{S}{\mathcal{S}_{\text{int}}} \cdot \Delta t. \tag{2.79}$$

2.5.5 Background Signal Sources

2.5.5.1 Background Source Importance

Some background signals are more impactful than others. For simulating realistic light curves, it is important to only model those background sources that have the possibility of being at or above the order of magnitude of the object signal, thereby seriously degrading the signal-to-noise ratio. As a baseline, the background terms modeled by Krag for the PROOF CCD performance model were implemented, namely scattered moonlight, airglow, zodiacal light, and integrated starlight [9]. In addition, twilight and light pollution models were implemented to increase the time and station location flexibility of the simulation. Each background term is modeled at medium fidelity — often using tabulated measurements or a set of exponential distributions to govern the scattering physics. As a result, this background performance model does not capture local weather conditions or precisely simulate the scattering of each photon through the atmosphere, but still strives to faithfully model the physics of each background signal process. Table 2.3 ranks the approximate magnitudes in photoelectrons per pixel one can expect from a telescope similar to the Purdue Optical Ground Station.

2.5.5.2 Astronomical Spectra

Four of the quantities needed for the background model vary with wavelength. These are the atmospheric transmission, the sensor quantum efficiency, the irradiance of a 0th magnitude star, and the solar spectrum. Each spectrum is displayed in Figure 2.15.

DISTRIBUTION A: Distribution approved for public release.

Source	**Magnitude** [$\mathbf{e^-/pix}$]
Twilight	$10^1 - 10^7$
Scattered moonlight	$0 - 10^5$
Airglow	$10^3 - 10^4$
Zodiacal light	$10^2 - 10^4$
Light pollution	$10^2 - 10^3$
Integrated starlight	$10^1 - 10^2$

Table 2.3. Background signal importance, values generated by the author using models by Krag and Daniels [9], [67]

DISTRIBUTION A: Distribution approved for public release.

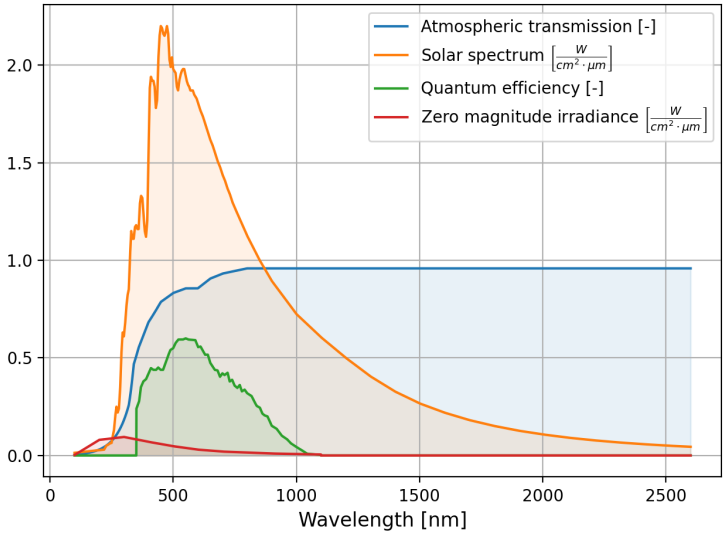

Figure 2.15. Astronomical Spectra, atmospheric transmission and zero magnitude stellar spectrum from [9]

In practice, the quantum efficiency curve varies by sensor and the thermal conditions of the observation. The curve adopted in this work is that used by Krag; modern sensors will often perform better.

2.5.5.3 Airglow

Certain chemical reactions from 80-110 km altitude in the upper atmosphere release visible light [9]. This effect is known as airglow. Since these reactions are assumed to be isotropic — equally intense when integrated along any vertical line extending upwards from the surface. The airglow signal $\mathcal{A}_{\text{int}}$ is modeled in asimilar fashion to integrated starlight. Given the airglow spectra $\mathcal{A}(\lambda)$ $\left[\frac{W}{m^2 \cdot m \cdot sr}\right]$, the sensor quantum efficiency $\text{QE}(\lambda)$, the atmospheric transmission $\text{ATM}(\lambda)$, as well as Plank's constant h and the speed of light in vacuum c, the airglow signal is computed by integrating over a range of wavelengths λ from the UV to IR bands via [9]:

$$\mathcal{A}_{\text{int}} = A_{\text{aperture}} \int_{10^{-8}}^{10^{-6}} \mathcal{A}(\lambda) \cdot \text{QE}(\lambda) \cdot \text{ATM}(\lambda) \cdot \left(\frac{\lambda}{hc}\right) d\lambda. \tag{2.80}$$

DISTRIBUTION A: Distribution approved for public release.

The quantity $\mathcal{A}_{\text{int}}$ has units $\left[\frac{1}{s \cdot sr}\right]$, meaning that the mean airglow signal in ADU per pixel $\bar{S}_{\text{airglow}}$ is simply given by:

$$\bar{S}_{\text{airglow}} = \mathcal{A}_{\text{int}} \cdot \text{AM}(\theta_z) \cdot \Delta t \cdot \left(\frac{\pi s_{\text{pix}}}{648000}\right)^2. \tag{2.81}$$

In Equation 2.81, $\text{AM}(\theta_z)$ is the relative airmass function which accounts for the accumulation of air along the optical path at different zenith angles [4]. This airmass is termed *relative* as it relates the ratio of absolute airmass at a zenith angle to the absolute airmass at zenith. Often, this function is approximated by the Van-Rhijn factor $\text{AM}(\theta_z) = \sec\theta_z$, which remains accurate up to $\theta_z \approx 70°$ before diverging to infinity. Instead, a function proposed by Pickering is used [68].

$$\text{AM}(\theta_z) = \frac{1}{\sin\left((90 - \theta_z) + \frac{244}{165 + 47(90-\theta_z)^{1.1}}\right)} \tag{2.82}$$

Using Equation 2.82 instead of the Van-Rhijn factor enables the computation of background signals near the horizon without the singularity of $\sec\theta_z$. Figure 2.16 displays this comparison in action.

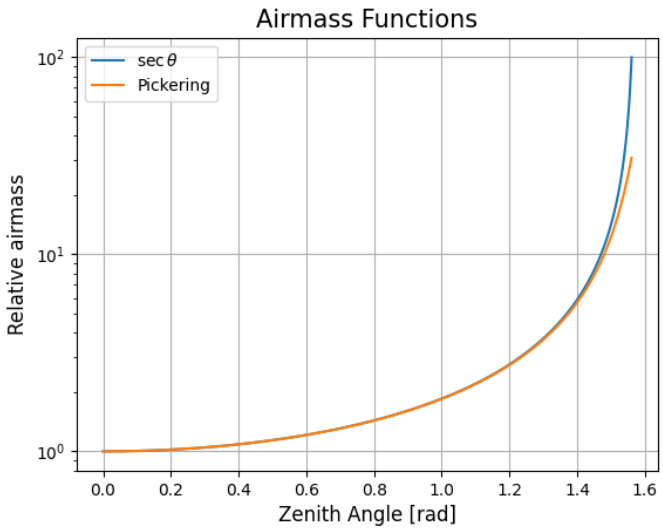

Figure 2.16. Airmass function comparison. The Van-Rhijn factor diverges to $+\infty$ while Pickering's function reaches the correct maximum of $\text{AM}(\theta_z) \approx 40$.

DISTRIBUTION A: Distribution approved for public release.

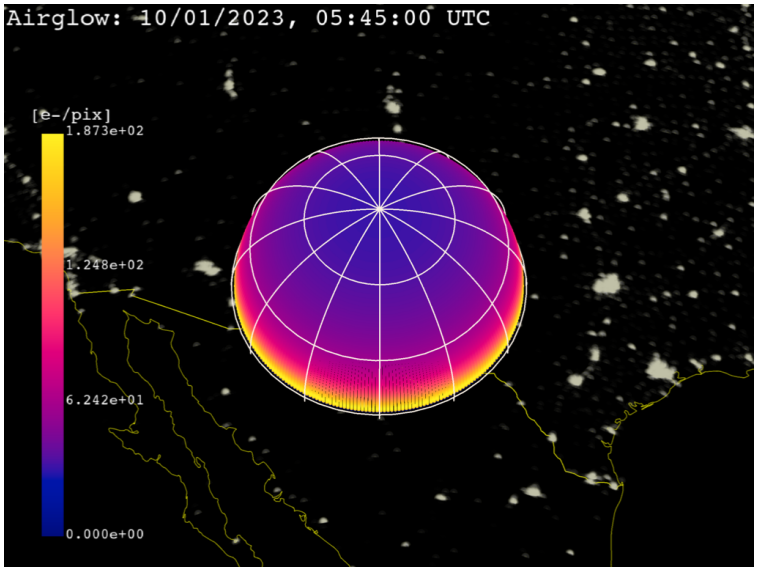

Figure 2.17. Mean airglow signal on the local observer hemisphere. The observer is in New Mexico, USA at 32.900° N, −105.533° W

2.5.5.4 Light Pollution

Another source of background noise is light pollution. On a cloudless night with low levels of atmospheric aerosols, the zenith surface brightness is approximately 22 $\left[\frac{mag}{arcsec^2}\right]$ (MPSAS) [9]. As light pollution increases, this zenith brightness may dip down to $14 - 15$ $\left[\frac{mag}{arcsec^2}\right]$. To get accurate localized zenith brightness values, the 2015 World Atlas of Sky Brightness dataset is used [69]. The data is reported in $\left[\frac{mcd}{cm^2}\right]$ on a 30-arcsecond grid, requiring conversion to a more useful unit. A subset of the global dataset is displayed in 2.18 This conversion is listed in Equation 2.76, using a monochromatic $\lambda = 474$ nm to fit the conversions of Falchi et al. [70].

The mean light pollution CCD signal in ADU per pixel is formulated similarly to airglow. The station's zenith surface brightness $B_{\text{poll},z}$ in MPSAS, linearly interpolated from the World Atlas dataset, is converted to irradiance per steradian via 2.74 and to ADU per pixel via the conversion factor $\mathcal{S}_{\text{int}}$, the integration time Δt, and the pixel scale s_{pix}, as $\bar{S}_{\text{pollution}}$ via:

$$\bar{S}_{\text{pollution}} = B_{\text{poll},z} \cdot \mathcal{S}_{\text{int}} \cdot \text{AM}(\theta_z) \cdot \Delta t \cdot \left(\frac{\pi s_{\text{pix}}}{648000}\right)^2. \tag{2.83}$$

DISTRIBUTION A: Distribution approved for public release.

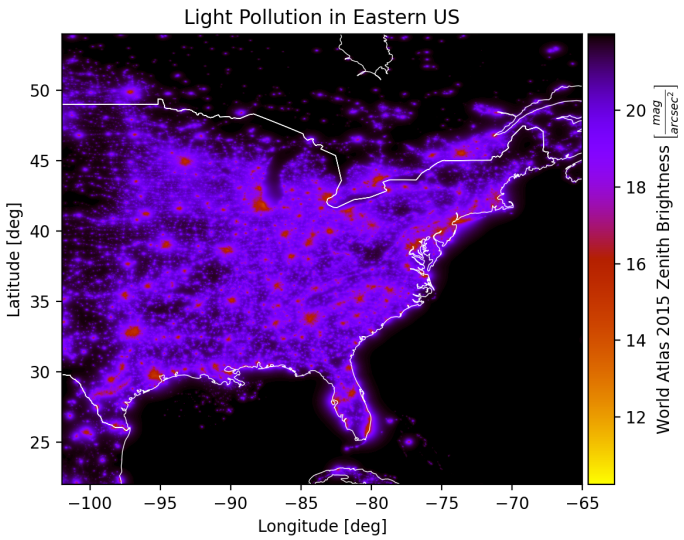

Figure 2.18. Zenith light pollution in the eastern USA, data from [69]

Note that Krag does not implement a specific light pollution model, but instead takes the dark sky site zenith brightness of 22 MPSAS as input to an atmospherically scattered light model [9]. The formulation of the light pollution model in Equation 2.83 is simply an adaptation of Krag's model with a variable zenith brightness driven by a light pollution dataset.

2.5.5.5 Twilight

Even after the Sun sets, scattered sunlight in the upper atmosphere creates a signal on the CCD. The twilight model implemented for this work is due to Patat et al. and was developed for the European Southern Observatory at Paranal in Chile [71]. This model implements the zenith brightness as a function of the solar zenith angle γ — the angle from zenith to the Sun's apparent centroid. The model of Patat et al. fits a second-degree polynomial in γ to approximately 2000 observations in varying atmospheric conditions, yielding separate curves for each of the UBVRI passbands. For example, for the V band, the twilight zenith brightness in MPSAS is given by [71]:

DISTRIBUTION A: Distribution approved for public release.

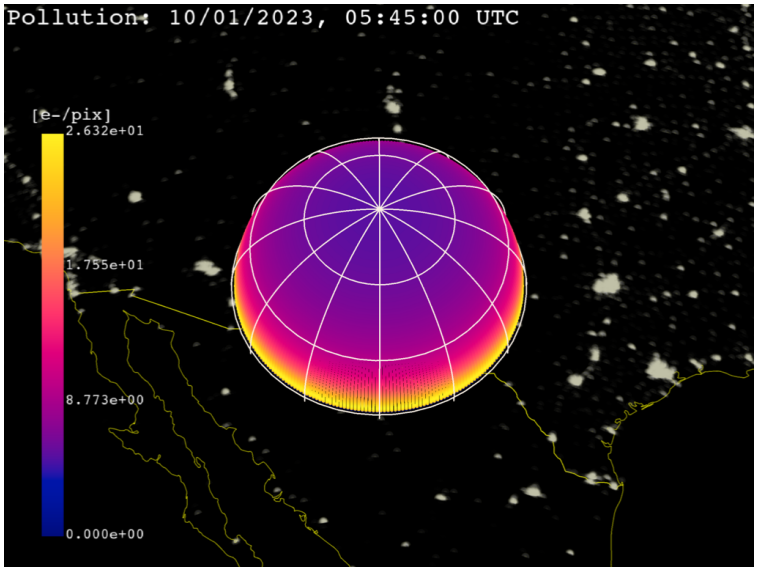

Figure 2.19. Mean light pollution signal on the local observer hemisphere. The observer is in New Mexico, USA at 32.900° N, −105.533° W

$$B_{twi,z} = 11.84 + 1.518(\gamma - 95^\circ) - 0.057(\gamma - 95^\circ)^2. \tag{2.84}$$

Equation 2.84 is valid from $95^\circ \leq \gamma \leq 105^\circ$. While $\gamma \leq 95^\circ$, the zenith brightness is taken to be constant and equal to the brightness at $\gamma = 95^\circ$. This is not accurate, as it predicts daylight to be the brightness of twilight, but is sufficiently bright to correctly forbid daytime observations by lowering the SNR drastically. After $\gamma = 105^\circ$ the zenith surface brightness is set to $B_{twi,z} = 22$ MPSAS to match the optimal observation condition of the light pollution model [9]. Zenith twilight brightness is plotted as a function of γ in Figure 2.20.

Computing the mean CCD signal in ADU per pixel due to the twilight brightness proceeds identically to the light pollution formulation. This conversion from MPSAS to ADU uses the conversion factor $\mathcal{S}_{\text{int}}$, the integration time Δt, and the pixel scale s_{pix}, as $\bar{S}_{\text{twilight}}$ via:

$$\bar{S}_{\text{twilight}} = B_{twi,z} \cdot \mathcal{S}_{\text{int}} \cdot \text{AM}(\theta_z) \cdot \Delta t \cdot \left(\frac{\pi s_{\text{pix}}}{648000}\right)^2. \tag{2.85}$$

The mean twilight signal on the local observer hemisphere is displayed in Figure 2.21.

DISTRIBUTION A: Distribution approved for public release.

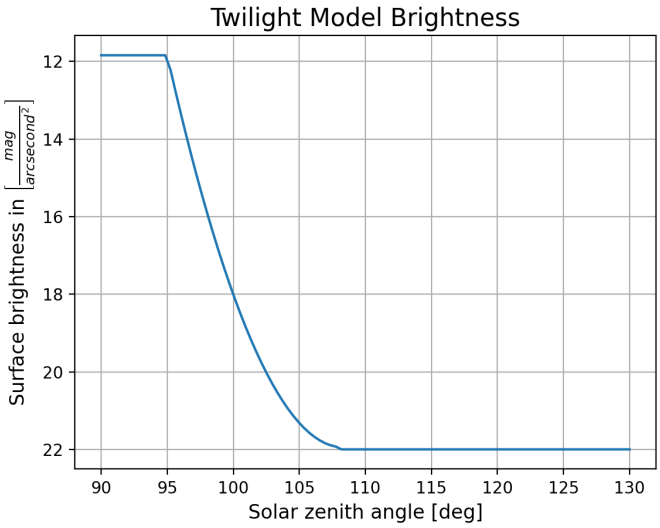

Figure 2.20. Twilight model surface brightness at zenith as a function of solar zenith angle

2.5.5.6 Integrated Starlight

Stars are almost always present in optical images of space objects. The brightest stars streaking across the field of view in Figure 2.22 have high SNRs and stand out clearly against the dark background. This raises a question: if the telescope observes a full $1^\circ \times 1^\circ$ area of the sky, where are the rest of the stars? The Milky Way alone contains approximately $1 \cdot 10^{11}$ stars. The answer is clear: many more stars are present in the image, most of them falling into the background. This residual faint starlight is termed "integrated" starlight. Computing the brightness of the integrated starlight in the background of the image circumvents the need to model all the stars in the catalog.

Krag [9] modeled this signal by building a $1^\circ \times 1^\circ$ grid of surface brightness values for the full inertial sphere, parameterized by RA/Dec. Krag used the Guide Star catalog, which contains 15 million stars down to apparent magnitude 16. Exponential extrapolation was used to predict star counts in each bin for higher magnitudes [9]. Twenty years later, larger star catalogs exist that are nearly complete to much higher apparent magnitudes. The integrated starlight catalog used in this work was built from the GAIA catalog with

DISTRIBUTION A: Distribution approved for public release.

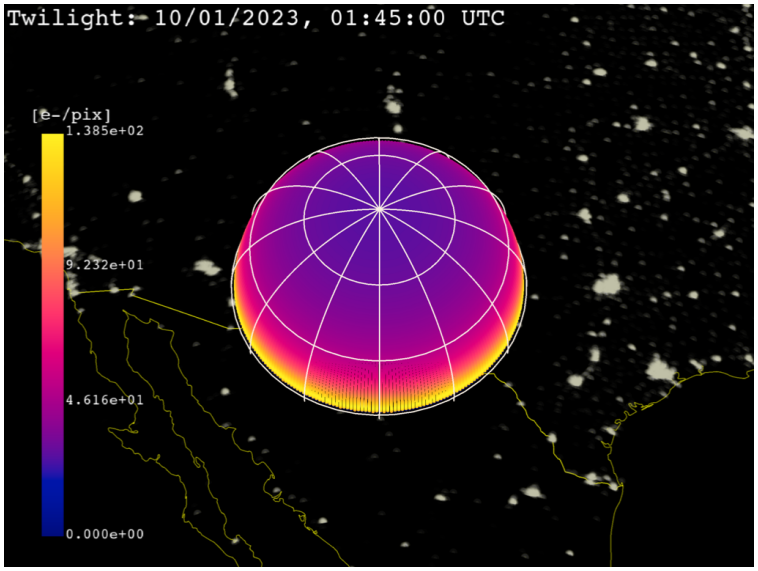

Figure 2.21. Mean twilight signal on the local observer hemisphere. The observer is in New Mexico, USA at 32.900° N, −105.533° W

approximately 1.5 billion stars down to magnitude 21-22 [72]. The same $1° \times 1°$ grid was computed using GAIA [73], resulting in Figure 2.23 which shows the computed brightness map in units of S_{10}.

With this map of exoatmospheric mean brightness of the night sky due to integrated starlight, the corresponding signal mean in the telescope CCD $\mathcal{Z}$ is computed using the zero magnitude star spectrum $\mathcal{ZM}(\lambda)$, the quantum efficiency $\mathrm{QE}(\lambda)$, and the atmospheric transmission $\mathrm{ATM}(\lambda)$, adopting Krag's formulation [9].

$$\mathcal{Z} = A_{\text{aperture}} \int_{10^{-8}}^{10^{-6}} \mathcal{ZM}(\lambda) \cdot \mathrm{QE}(\lambda) \cdot \mathrm{ATM}(\lambda) \cdot \left(\frac{\lambda}{hc}\right) d\lambda \tag{2.86}$$

In Equation 2.86, A_{aperture} is the telescope aperture area in meters, h is Plank's constant in $\left[\frac{m^2 kg}{s}\right]$, and c is the speed of light in vacuum in $\left[\frac{m}{s}\right]$. The resulting quantity $\mathcal{Z}$ has units of $\left[\frac{1}{s}\right]$, representing the mean total photons passing through the telescope aperture due to a zero magnitude star source per second of integration time. This quantity is used to compute the total signal in the CCD due to integrated starlight:

DISTRIBUTION A: Distribution approved for public release.

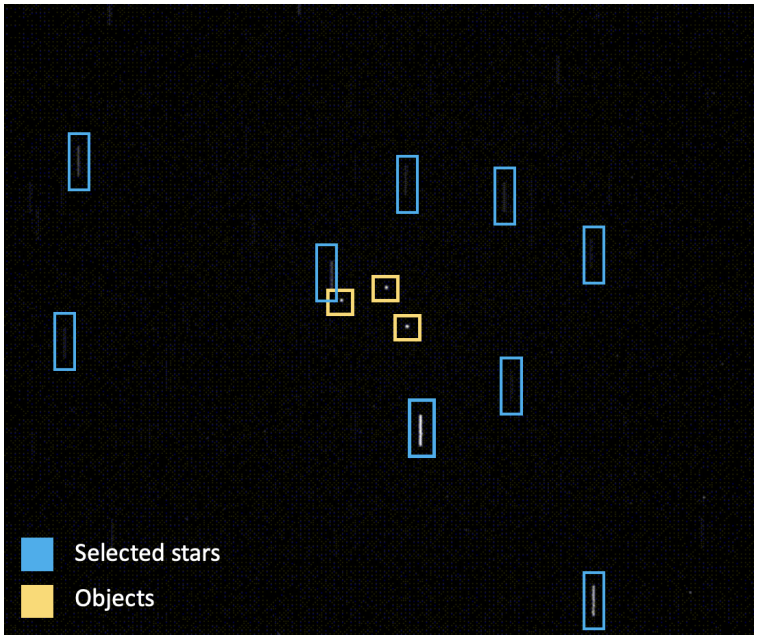

Figure 2.22. Raw image of three GEO objects with stars streaking through the background. As expected, the star signals have a variety of signal-to-noise ratios. Taken by the Purdue Optical Ground station at 32.900° N, −105.533° W by Nathan Houtz.

$$\bar{S}_{\text{star}} = 10^{-4} \cdot \mathcal{Z} \cdot \left(\frac{s_{\text{pix}}}{3600}\right)^2 \cdot \Delta t \cdot B_{\text{is}}, \tag{2.87}$$

In Equation 2.87, B_{is} is the integrated starlight brightness in $[S_{10}]$ computed by linearly interpolating the dataset in Figure 2.23, s_{pix} is the telescope pixel scale in $\left[\frac{arcsecond}{pix}\right]$ and Δt is the integration time in seconds. Note the addition of the 10^{-4} factor to reconcile catalog surface brightness in terms of 10th magnitude stars, and the 0th magnitude source in $\mathcal{Z}$. This yields $\bar{S}_{\text{star}}$ with units $\left[\frac{\text{e}^-}{pix^2}\right]$; photoelectron counts (ADU) per pixel. Figure 2.24 shows the background signal mean due to integrated starlight.

2.5.5.7 Scattered Moonlight

Moonlight scattering through the atmosphere significantly increases background brightness [9]. This scattering effect can be decomposed into Rayleigh (isotropically distributed)

DISTRIBUTION A: Distribution approved for public release.

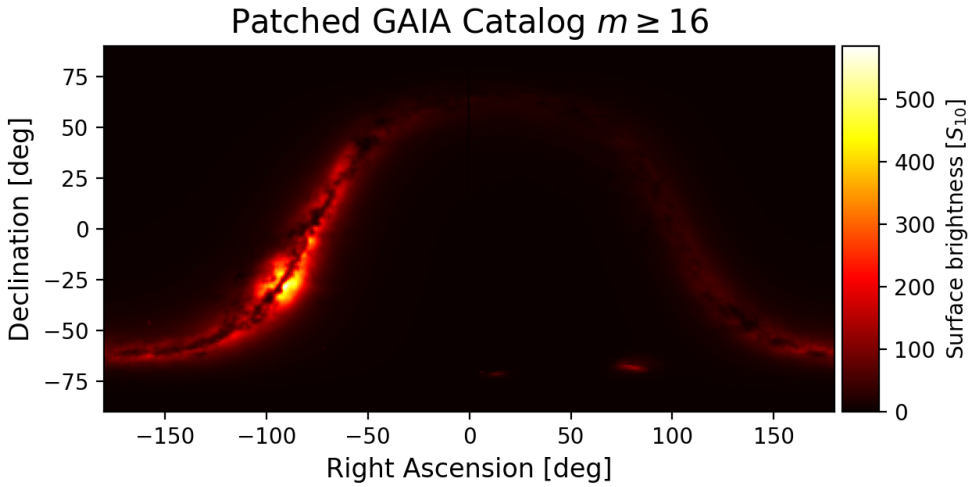

Figure 2.23. Integrated starlight brightness map, produced from Gaia DR3 data [72] using [73]

and Mie (exponentially distributed) scattering modes. The Rayleigh scattered component is computed with Table 4 published by Daniels parameterized by the angle from the observation to zenith θ_{obs}, the angle from the Moon to zenith θ_{moon}, and the angle between the observation and the Moon on the horizon ΔAz [67]. Interpolating this table yields the intensity of the Rayleigh scattering F_{rs} in 10^{-10} $W/(cm^2 \cdot \mu m \cdot sr)$ [9]. The Mie scattered component F_{ms} is formulated [9]:

$$F_{ms}(\lambda) = a_1 \left[\mathrm{e}^{-\left(\frac{\Psi}{\Psi_1}\right)} + a_2 \mathrm{e}^{-\left(\frac{\pi-\Psi}{\Psi_2}\right)} \right] F_{rs}(\lambda). \tag{2.88}$$

Daniels recommends $a_1 \in [50, 100]$, $a_2 \in [0.01, 0.02]$, $\Psi_1 \in [10°, 20°]$, and $\Psi_2 \approx 50$ [67]. Prior to any station-specific fitting, the center of each interval is chosen, yielding $a_1 = 75$, $a_2 = 0.015$, $\Psi_1 = 15°$, and $\Psi_2 = 50°$. a_1 and a_2 are dimensionless, such that F_{ms} also has

DISTRIBUTION A: Distribution approved for public release.

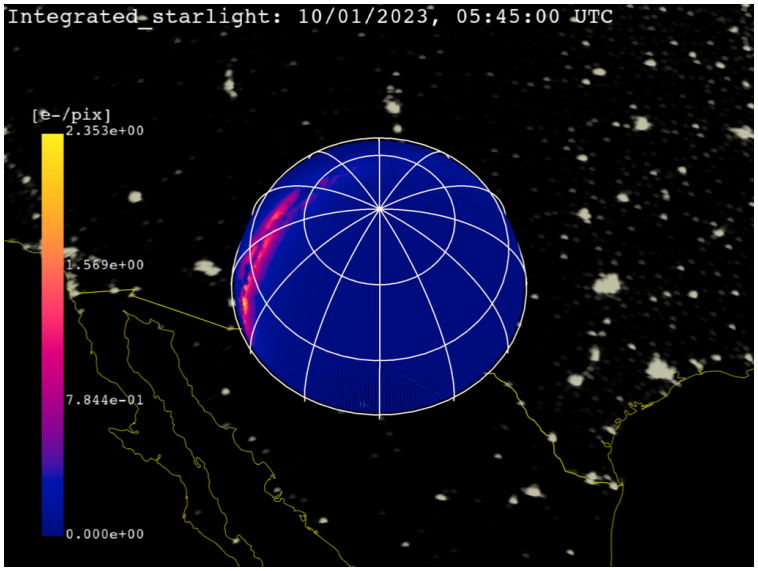

Figure 2.24. Integrated starlight signal on the local observer hemisphere. The observer is in New Mexico, USA at 32.900° N, −105.533° W

units of $10^{-10}\ W/(cm^2 \cdot \mu m \cdot sr)$. The total intensity of the scattered moonlight F_{mt}, following Krag's formulation, is given by [9]:

$$F_{mt} = f(\theta)\left[F_{rs}(\lambda) + F_{ms}(\lambda)\right]. \tag{2.89}$$

In Equation 2.89, $f(\theta)$ is the lunar phase function which describes the fraction of the full Moon brightness reflected at an observer when the Sun-Moon-observer angle is θ. This function is linearly interpolated within Table 3 in [67]. Finally, Krag introduces a correction factor f_{corr} to account for the difference between the Sun's irradiance spectrum sun(λ) and the spectrum of scattered moonlight, defined to be [9]:

$$f_{\text{corr}} = \frac{I_s}{\text{sun}(550\ [\text{nm}])}. \tag{2.90}$$

With all these pieces, the mean scattered moonlight signal in ADU per pixel is simply the product of the total scattering intensity F_{mt}, the irradiance to ADU conversion factor $\mathcal{S}_{\text{int}}$, the pixel scale s_{pix}, the integration time Δt, and the spectral correction factor f_{corr} [9]:

DISTRIBUTION A: Distribution approved for public release.

$$\bar{S}_{\text{moon}} = F_{mt}(550\ [\text{nm}]) \cdot \mathcal{S}_{\text{int}} \cdot \left(\frac{s_{\text{pix}}}{3600}\right)^2 \cdot \Delta t \cdot f_{\text{corr}}. \tag{2.91}$$

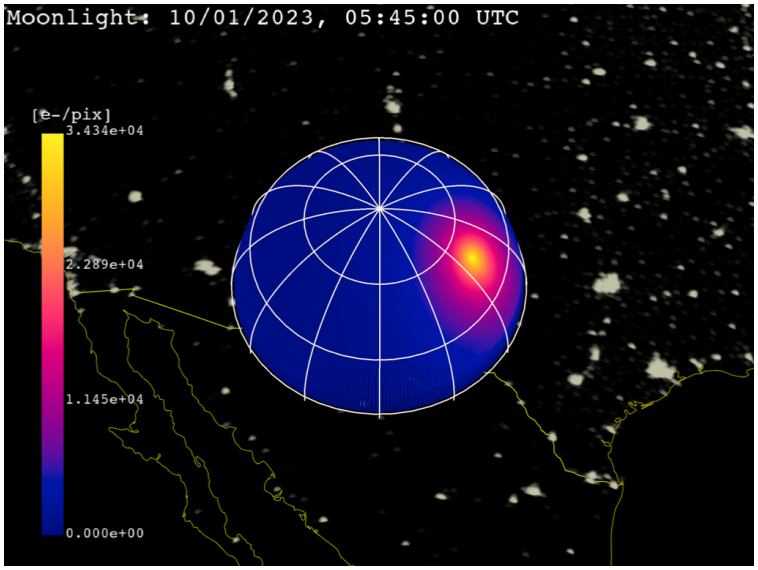

Figure 2.25. Mean scattered moonlight signal on the local observer hemisphere. The observer is in New Mexico, USA at 32.900° N, −105.533° W

2.5.5.8 Zodiacal Light

Zodiacal light is an effect created by sunlight reflecting off of dust in the ecliptic plane [9]. Zodiacal light is strongest around the Sun — an exclusion zone for most optical telescopes — but also reaches a peak directly away from the Sun due to the opposition effect. This peak is known as the Gegenschein, meaning "opposing light". The zodiacal light brightness is linearly interpolated within Table 1 of [74] which is listed for convenience in Appendix 6.2.3. This reports the surface brightness of the zodiacal light $B_{\text{zod}}(\alpha, \delta)$ in S_{10}, which is used without conversion to find the mean CCD signal in ADU per pixel using the pixel scale s_{pix} and the integration time Δt via:

$$\bar{S}_{\text{zod}} = \mathcal{Z} \cdot \left(\frac{s_{\text{pix}}}{3600}\right)^2 \cdot \Delta t \cdot B_{\text{zod}}(\alpha, \delta) \cdot 10^{-4}. \tag{2.92}$$

DISTRIBUTION A: Distribution approved for public release.

As in the integrated starlight signal, the 10^{-4} factor reconciles the S_{10} surface brightness with the 0th magnitude source in $\mathcal{Z}$.

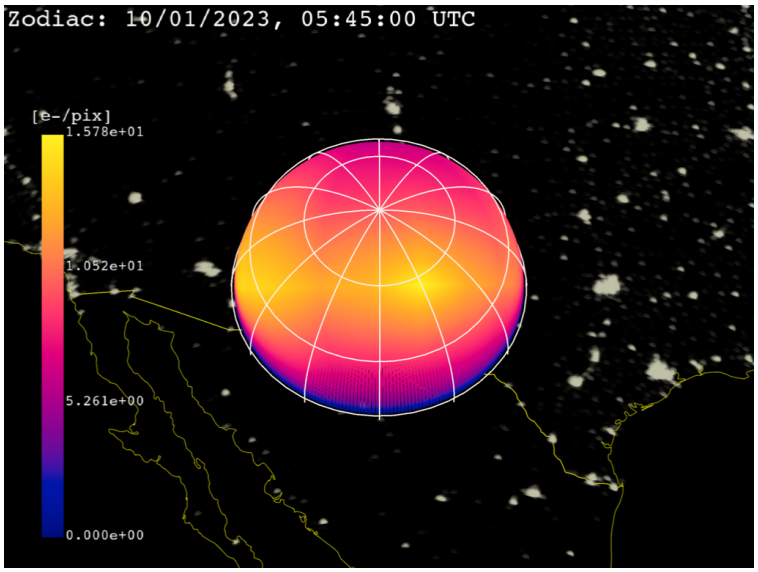

Figure 2.26. Mean zodiacal light signal on the local observer hemisphere. The observer is in New Mexico, USA at 32.900° N, −105.533° W

2.5.5.9 Background Sampling

The background signals are only defined in terms of their means, as each signal models the expected amount of radiation without accounting for the quantized nature of light [9]. Since light is transmitted in individual photons, their incidence on a given pixel will follow a statistical distribution. Assuming that each photon does not interact with others, the incidence of a photon on a pixel is well modeled as a Poisson process for each background term [4]. This distribution models the number of independent and identically distributed events that occur during a time period. For CCD astronomy, this translates to the event of a photon hitting the sensor. A Poisson distribution is defined on the positive integers by a single parameter λ which is both the mean and variance of the distribution. The probability density function (PDF) for the Poisson distribution takes the form [4]:

$$P_\lambda(x = k) = \frac{\lambda^k \mathrm{e}^{-\lambda}}{k!}. \tag{2.93}$$

DISTRIBUTION A: Distribution approved for public release.

This distribution has a useful property that $P_{\lambda_1+\lambda_2}(x=k) = P_{\lambda_1}(x=k) + P_{\lambda_2}(x=k)$ so long as the distributions described by λ_1 and λ_2 are independent. The background sources modeled in this work are reasonably assumed to be independent as they each originate from distinct physical processes, yielding the overall Poisson parameter for the background $\lambda_{\text{background}}$.

$$\lambda_{\text{background}} = \bar{S}_{\text{airglow}} + \bar{S}_{\text{pollution}} + \bar{S}_{\text{twilight}} + \bar{S}_{\text{star}} + \bar{S}_{\text{moon}} + \bar{S}_{\text{zod}} \tag{2.94}$$

Drawing samples from the Poisson distribution defined by $\lambda_{\text{background}}$ computes the background of the CCD image.

2.5.6 Sensor Effects

CCD sensors accumulate noise during both the integration time and readout phases. Characterizing these noise sources is necessary to sample realistic light curves and compute the signal-to-noise ratio of the measurements.

2.5.6.1 Dark Noise

The dark noise, also called the dark current or dark count, captures the temperature-dependent accumulation of electrons in the CCD pixel wells [9]. This noise source is modeled as a Poisson process with parameter λ_{dark} [4] and is assumed to be independent from the other sensor effects. This source accumulates with the integration time, giving it units of counts per second [9].

2.5.6.2 Readout Noise

When the CCD is read out, the charge contained in each pixel well must be digitized. This process introduces noise in the final signal due to electronic effects within the CCD circuitry and its surrounding environment [9]. The readout noise is modeled as a zero-mean Gaussian distribution with variance σ^2_{read} and is also assumed to be independent from other sensor effects [4].

DISTRIBUTION A: Distribution approved for public release.

2.5.6.3 Truncation Noise

Truncation noise in a CCD stems from the fact that the charge in each pixel is digitized into an integer factor of the gain [4]. This is modeled using a uniform distribution on $[-g/2, g/2]$, yielding a variance $N_{\text{trunc}}^2 = \frac{g^2}{24}$ [4].

The particular noise variances for the Purdue Optical Ground Station are listed in 6.1.

2.5.7 Observer Constraints

Accurately simulating light curves requires realistic constraints on the observing station. For an optical ground station, basic operational constraints include local eclipse, target SNR, Moon exclusion angle, and minimum elevation constraints. This section develops these constraints.

2.5.7.1 Earth Penumbra

The Earth casts a conical shadow into space. Outside this shadow, the fraction of received solar irradiance f_{sun} is assumed to be 1. Inside the shadow, the central region of zero received solar irradiance $f_{\text{sun}} = 0$ is known as umbra, while the boundary between umbra and full Sun is known as the penumbra where $f_{\text{sun}} \in (0, 1)$. The precise gradient of the penumbra is defined by the geometry of the overlapping Earth and Sun disks from the perspective of the object. Given the position of the Sun $\boldsymbol{r}_{\text{sun}}$ computed following Section 2.4.8 and object in J2000, the local irradiance fraction is expressed [9]:

DISTRIBUTION A: Distribution approved for public release.

$$
\begin{aligned}
\boldsymbol{r}_{obj\to Sun} &= \boldsymbol{r}_{\text{sun}} - \boldsymbol{r}_{\text{obj}} \\
\epsilon_s &= \sin^{-1}\left(\frac{R_{\text{sun}}}{\|\boldsymbol{r}_{obj\to Sun}\|}\right) \\
\epsilon_{\text{e}} &= \sin^{-1}\left(\frac{R_{\text{Earth}}(\phi_{\text{obj}})}{\|\boldsymbol{r}_{\text{obj}}\|}\right) \\
\epsilon &= \cos^{-1}\left(-\hat{\boldsymbol{r}}_{obj\to Sun}\cdot\hat{\boldsymbol{r}}_{\text{obj}}\right) \\
\epsilon_1 &= \frac{\epsilon^2 - \epsilon_{\text{e}}^2 + \epsilon_s^2}{2\epsilon} \\
\epsilon_2 &= \frac{\epsilon^2 + \epsilon_{\text{e}}^2 - \epsilon_s^2}{2\epsilon}.
\end{aligned}
\tag{2.95}
$$

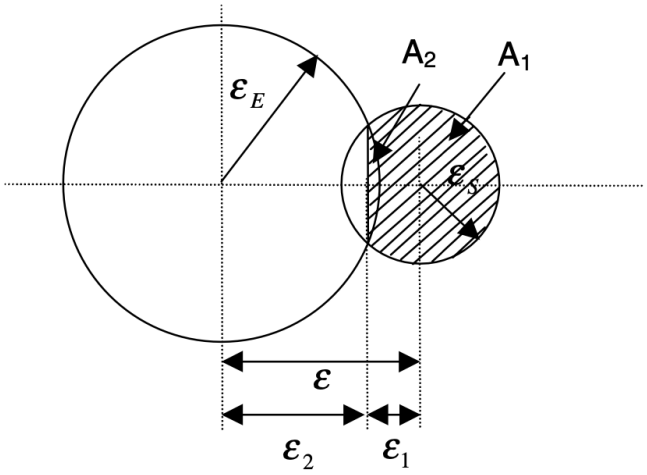

Figure 2.27. Angle and area definitions for penumbra shadowing, Figure 5.20 in [9]

In Equation 2.95, $\boldsymbol{r}_{obj\to Sun}$ is the vector from the object to the Sun in J2000, ϵ_s is the half-angle of the Sun disk at the object, ϵ_{e} is the half-angle of the Earth disk from the object as a function of the geodetic latitude of the object ϕ_{obj}. Additionally, ϵ is the angle between the center of the Earth and Sun from the perspective of the object, with ϵ_1 and ϵ_2 being the angles from the center of the Sun and Earth disks to the center of their overlap, if it exists

DISTRIBUTION A: Distribution approved for public release.

[9]. These angles are defined in Figure 2.27. Given these angles, the illumination fraction f_{sun} is computed:

$$f_{\text{sun}} = \begin{cases} 1 & \epsilon \geq (\epsilon_s + \epsilon_e) \\ 0 & \epsilon \leq (\epsilon_e - \epsilon_s) \\ \frac{a_1 - a_2}{\pi \epsilon_s^2} & \text{else} \end{cases}. \tag{2.96}$$

In Equation 2.96, the solid angles a_1 and a_2 are defined graphically in Figure 2.27 and are computed via:

$$\begin{aligned} a_1 &= \pi \epsilon_s^2 - \epsilon_s^2 \cos^{-1}\left(\frac{\epsilon_1}{\epsilon_s}\right) + \epsilon_1 \sqrt{\epsilon_s^2 - \epsilon_1^2} \\ a_2 &= \epsilon_e^2 \cos^{-1}\left(\frac{\epsilon_2}{\epsilon_e}\right) - \epsilon_2 \sqrt{\epsilon_e^2 - \epsilon_2^2} \end{aligned} \tag{2.97}$$

Computing Equation 2.96 for a dense grid of points in the J2000 reference frame reveals the geometry of the penumbra and umbra in Figure 2.28, illustrating that the penumbra expands into the umbra as the observer recedes from the Earth.

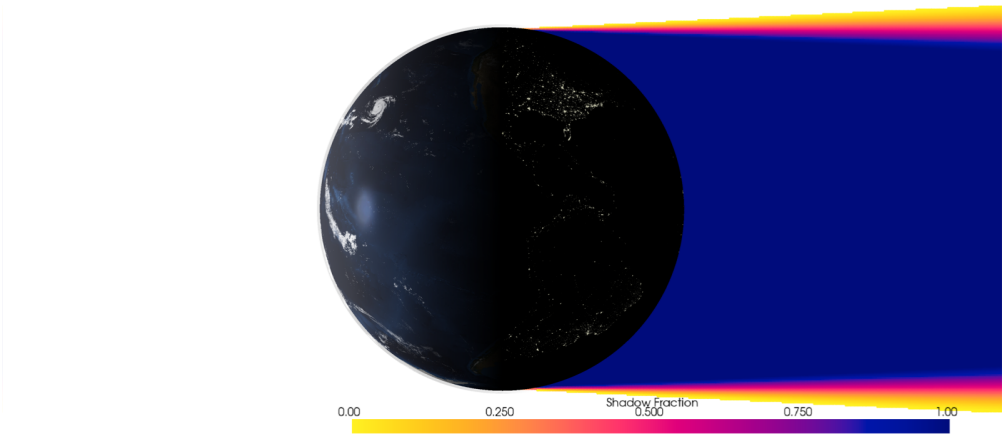

Figure 2.28. Shadow fraction in J2000, effect exaggerated by scaling the Sun radius by a factor 10

DISTRIBUTION A: Distribution approved for public release.

2.5.7.2 SNR

As the signal-to-noise ratio of an object signal on the CCD pixel grid degrades, it becomes more difficult to determine whether an object is present at all. Given a minimum limiting SNR SNR_{min} this constraint takes the form:

$$\nu_{\text{SNR}} = \begin{cases} 1 & \text{SNR} > \text{SNR}_{min} \\ 0 & \text{else} \end{cases}. \tag{2.98}$$

In Equation 2.98, $\nu_{\text{SNR}} = 1$ implies that the observation is valid, with $\nu_{\text{SNR}} = 0$ implying that the object signal cannot be discerned from the image background.

2.5.7.3 Moon Exclusion Angle

Focusing the irradiance of the Moon onto the sensor grid will seriously damage the CCD. For the Purdue Optical Ground Station, stray light from the Moon begins leaking into the optics around 30° from the center of the Moon disk. This observation constraint ν_{moon} is imposed for an arbitrary exclusion angle $\theta_{Moon,ex}$ for a certain inertial position of the Moon $\boldsymbol{r}_{\text{moon}}$, observer $\boldsymbol{r}_{\text{obs}}$, and object $\boldsymbol{r}_{\text{obj}}$ via:

$$\nu_{\text{moon}} = \begin{cases} 1 & \cos^{-1}\left(\frac{(\boldsymbol{r}_{\text{moon}}-\boldsymbol{r}_{\text{obs}})\cdot(\boldsymbol{r}_{\text{obj}}-\boldsymbol{r}_{\text{obs}})}{\|\boldsymbol{r}_{\text{moon}}-\boldsymbol{r}_{\text{obs}}\|\|\boldsymbol{r}_{\text{obj}}-\boldsymbol{r}_{\text{obs}}\|}\right) > \theta_{Moon,ex} \\ 0 & \text{else} \end{cases}. \tag{2.99}$$

In Equation 2.99, $\nu_{\text{moon}} = 1$ implies that the observation is valid, with $\nu_{\text{moon}} = 0$ implying that the observation is too close to the Moon. $\boldsymbol{r}_{\text{moon}}$ should be computed with SPICE following Section 2.4.8.

2.5.7.4 Minimum Elevation

Due to the local topology at the observer location, an operator may assign a minimum angle from the horizon $\theta_{elev,min}$ for observations. Approximating the station inertial position $\boldsymbol{r}_{\text{obs}}$ as being aligned with zenith, this yields the condition $\nu_{\text{elevation}}$ for the object inertial position $\boldsymbol{r}_{\text{obj}}$ and observer inertial position $\boldsymbol{r}_{\text{obs}}$:

DISTRIBUTION A: Distribution approved for public release.

$$\nu_{\text{elevation}} = \begin{cases} 1 & 90^\circ - \cos^{-1}\left(\frac{\left(\boldsymbol{r}_{\text{obj}} - \boldsymbol{r}_{\text{obs}}\right)\cdot\left(\boldsymbol{r}_{\text{obs}}\right)}{\|\boldsymbol{r}_{\text{obj}} - \boldsymbol{r}_{\text{obs}}\|\|\boldsymbol{r}_{\text{obs}}\|}\right) > \theta_{elev,min} \\ 0 & \text{else} \end{cases}. \tag{2.100}$$

In Equation 2.100, $\nu_{\text{elevation}} = 1$ implies that the observation is valid, with $\nu_{\text{elevation}} = 0$ implying that the observation is too close to the horizon.

2.5.8 Mean Irradiance at The Observer

Given the normalized irradiance computed via Equation 2.34 for convex objects or Equation 2.42 for any object shaded using Algorithm 4, the received mean irradiance at the telescope aperture is given by the normalized irradiance $\check{I}$, the observer position $\boldsymbol{r}_{\text{obs}}$, the object position $\boldsymbol{r}_{\text{obj}}$, the total solar irradiance I_s, and the solar illumination fraction f_{sun}:

$$\bar{I} = \nu_{Moon,ex} \cdot \nu_{\text{elevation}} \cdot \nu_{\text{SNR}} \cdot \frac{I_s f_{\text{sun}} \check{I}}{\left(\boldsymbol{r}_{\text{obj}} - \boldsymbol{r}_{\text{obs}}\right)^2}. \tag{2.101}$$

In Equation 2.101, the conditions $\nu_{Moon,ex}, \nu_{\text{elevation}}, \nu_{\text{SNR}}$ determine whether the telescope can take the observation and identify the object in the image, $I_s f_{\text{sun}}$ determines the solar irradiance incident on the object, and the remaining terms $\check{I}/\left(\boldsymbol{r}_{\text{obj}} - \boldsymbol{r}_{\text{obs}}\right)^2$ dimensionalize the normalized irradiance. In order to sample a noisy light curve, this mean irradiance must be converted into a mean photoelectron count $\bar{C}_{\text{all}}$ via Equation 2.78 as a function of the integration time Δt, the irradiance to count conversion factor $\mathcal{S}_{\text{int}}$, and the mean irradiance $\bar{I}$ as:

$$\bar{C}_{\text{all}} = \mathcal{S}_{\text{int}} \cdot \bar{I} \cdot \Delta t. \tag{2.102}$$

2.5.9 Sampling Noisy Light Curves

Given the irradiance of the object observed by the telescope, the noisy light curve is computed by building a grid containing the object signal, background noise, and sensor noise. On a pixel-by-pixel basis, the mean object signal is given by an alteration of

DISTRIBUTION A: Distribution approved for public release.

Equation 2.66 where the angle θ from the center of the frame is converted into pixels via $\theta^2 = \left((x - x_0)^2 + (y - y_0)^2\right) / s_{\text{pix}}^2$:

$$\bar{C}_{\text{obj}}(x, y) = \frac{0.838 \bar{C}_{\text{all}}}{2\pi\sigma^2} \exp\left(-\frac{(x - x_0)^2 + (y - y_0)^2}{2\sigma^2 s_{\text{pix}}^2}\right). \tag{2.103}$$

In Equation 2.103, (x_0, y_0) are the exact pixel coordinates of the object centroid, σ is the Gaussian standard deviation from Equation 2.65 in arcseconds, and s_{pix} is the pixel scale in arcseconds per pixel. Likewise, the total noise sampled in each pixel is given by samples from all the relevant source distributions is given by C_{noise}:

$$C_{\text{noise}} = N_{\text{background}} + N_{\text{dark}} + N_{\text{trunc}} + N_{\text{read}}. \tag{2.104}$$

In Equation 2.104, $N_{\text{background}}$ is a sample drawn from $\text{Pois}(\lambda_{\text{background}})$, N_{dark} is drawn from $\text{Pois}(\Delta t \cdot \lambda_{\text{dark}})$, N_{trunc} is drawn from $\text{Uniform}(-g/2, g/2)$, and N_{read} is drawn from $\text{N}(0, \sigma_{\text{read}}^2)$.

Assuming perfect knowledge of the image background mean in the region around the object signal — a reasonable assumption given that there are generally millions of background pixels in the image — the counts $C_{\text{obj},meas}$ attributed to the object pixels $\{x_{\text{obj}}, y_{\text{obj}}\}$ is given by:

$$\begin{aligned} C_{noise,all} &= \sum_{\text{i}=1}^{A_{\text{airy}}} C_{noise,\text{i}} \\ C_{\text{obj},all} &= \sum_{x \in x_{\text{obj}},\, y \in x_{\text{obj}}} \bar{C}_{\text{obj}}(x, y) \\ C_{\text{obj},meas} &= C_{noise,all} - A_{\text{airy}} \left(\Delta t \cdot \lambda_{\text{dark}} + \lambda_{\text{background}}\right) \end{aligned} \tag{2.105}$$

In Equation 2.105, A_{airy} is the area of the central maximum of the Airy disk in square pixels presented in Equation 2.68. The measured object signal $C_{\text{obj},meas}$ can then be transformed into irradiance $I_{\text{obj},meas}$ via Equation 2.79 using the integration time Δt and the irradiance to count conversion factor $\mathcal{S}_{\text{int}}$:

DISTRIBUTION A: Distribution approved for public release.

$$I_{\text{obj},meas} = \frac{C_{\text{obj},meas}}{\mathcal{S}_{\text{int}} \cdot \Delta t} \tag{2.106}$$

or to apparent magnitude $m_{\text{obj},meas}$ by applying Equation 2.31 using the zero point irradiance I_0:

$$m_{\text{obj},meas} = -2.5 \log_{10} \left(\frac{I_{\text{obj},meas}}{I_0} \right) \tag{2.107}$$

or normalized irradiance $\check{I}_{\text{obj},meas}$ by applying Equation 2.32 using the total solar irradiance I_s and the position of the object $\boldsymbol{r}_{\text{obj}}$ and observer $\boldsymbol{r}_{\text{obs}}$ relative to some common origin:

$$\check{I}_{\text{obj},meas} = \frac{\|\boldsymbol{r}_{\text{obj}} - \boldsymbol{r}_{\text{obs}}\|^2}{I_s} I_{\text{obj},meas}. \tag{2.108}$$

2.6 Light Curve Simulation Results

2.6.1 Case 1: Normalized Light Curve of a Simple Object

This section presents the entire process for simulating the normalized light curve of a simple object. To begin, the properties of the object and the observing station are defined in Table 2.4. The cube model used for this case is displayed in Figure 2.29.

To begin, the position of the object in TEME is computed using SGP4. That position is converted to ICRF using Eqs 2.56, 2.57, and 2.58. The position of the station in ITRF is computed using Equation 2.51 and converted to ICRF using Eqs 2.54, 2.55, 2.56, 2.57, and 2.58. The position of the Sun is determined with SPICE following Section 2.4.8.

The attitude profile of the object is propagated with Eqs 2.9 and 2.8 using $\boldsymbol{M} = \boldsymbol{0}$ for torque free rigid body motion. The resulting attitude time history produces $\boldsymbol{q}(t)$, $\boldsymbol{\omega}(t)$, as well as the body frame vectors from the object to the Sun and observer depicted in Figure 2.30.

Next, the BRDF is used to compute the reflection matrix for the cube with Equation 3.9. The normalized light curve is simply computed with Equation 2.34, using Equation 2.19 and

DISTRIBUTION A: Distribution approved for public release.

Parameter	**Value**
Object	`cube.obj` 6.4
SATNUM	36411
$\boldsymbol{q}_0$	$[0, 0, 0, 1]^T$
$\boldsymbol{\omega}_0$	$[0.04082483, 0.08164966, 0.04082483]^T$ $[rad/s]$
J	$\text{diag}\,(1.0, 2.0, 3.0)$ $[kg \cdot m^2]$
BRDF	Phong
C_s	0.3
C_d	0.7
n	5
Initial date	2023-03-26 05:00:00 UTC
Δt	0.1 $[s]$
n_{obs}	360 $[s]$
ϕ_{geod}	$32.900°$
λ	$-105.533°$

Table 2.4. Object and station simulation parameters for case 1

DISTRIBUTION A: Distribution approved for public release.

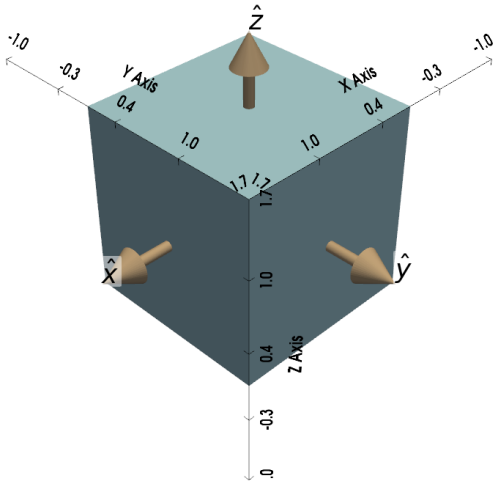

Figure 2.29. Cube model for case 1

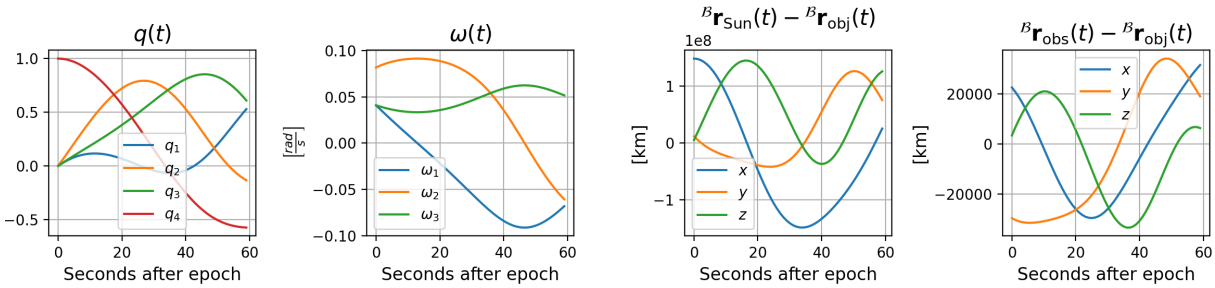

Figure 2.30. Attitude time history for case 1

noting that $\mu_{ij} = 0$ as the object is convex. This yields the normalized light curve depicted in Figure 2.31.

Figure 2.31 has a few important features to recognize. Some sections of the light curve are flat, indicating that all illuminated faces are orthogonal to each other and reflecting diffusely. When one of the face normal vectors approaches the halfway vector H, a specular glint occurs, leading to a temporary sharp increase in the light curve value. Overall, this is exactly the behavior expected given the observation conditions.

DISTRIBUTION A: Distribution approved for public release.

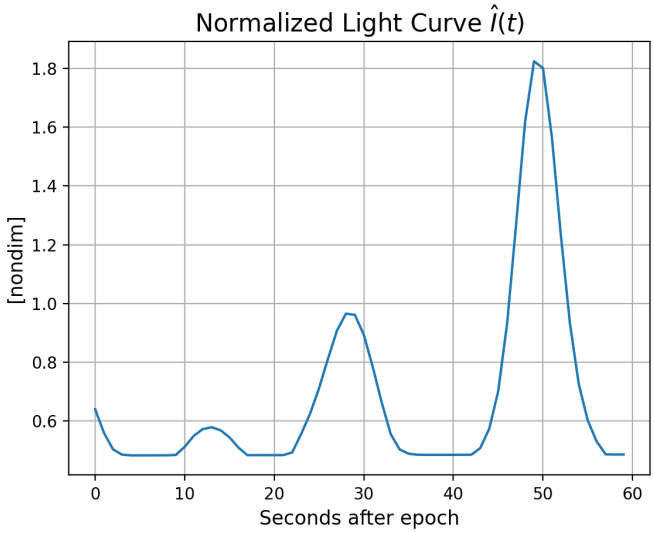

Figure 2.31. Normalized light curve for case 1

2.6.2 Accurate Satellite Models

To produce accurate light curves for real space objects, 3D model files were collected and tuned for use with the light curve simulator. These models are shown in Figure 2.32. Each model is correctly scaled, with accurate material properties applied to their faces. Figure 2.32 highlights the size of the GEO communications satellites (TELSTAR, HYLAS, Hispasat, and ASTRA). In contrast, the LEO satellites (Starlink and Landsat) are dwarfed at the left end of the lineup.

2.6.3 Case 2: Realistic Light Curve for a Box-Wing Satellite

The second case deals with simulating a realistic noisy light curve for a complex, non-convex satellite model with observer constraints. Table 2.5 summarizes the simulation parameters for the object and station. The object geometry is displayed in Figure 2.33.

To begin, the position of the object in TEME is computed using SGP4. That position is converted to ICRF using Eqs 2.56, 2.57, and 2.58. The position of the station in ITRF is

DISTRIBUTION A: Distribution approved for public release.

Parameter	**Value**
Object	goes17.obj
SATNUM	32711
$\boldsymbol{q}_0$	$[0, 0, 0, 1]^T$
$\boldsymbol{\omega}_0$	$[0.00707107, 0., 0.00707107]^T$ $[rad/s]$
J	$\text{diag}\,(1.0, 2.0, 2.0)$ $[kg \cdot m^2]$
BRDF	Phong
Initial date	2022-12-09 08:00:00 UTC
Δt	10 $[s]$
n_{obs}	180 $[s]$
Telescope	Table 6.1
ϕ_{geod}	32.900°
λ	-105.533°
SNR_{min}	3
$\theta_{Moon,ex}$	30°
$\theta_{elev,min}$	15°

Table 2.5. Object and station simulation parameters for case 2

DISTRIBUTION A: Distribution approved for public release.

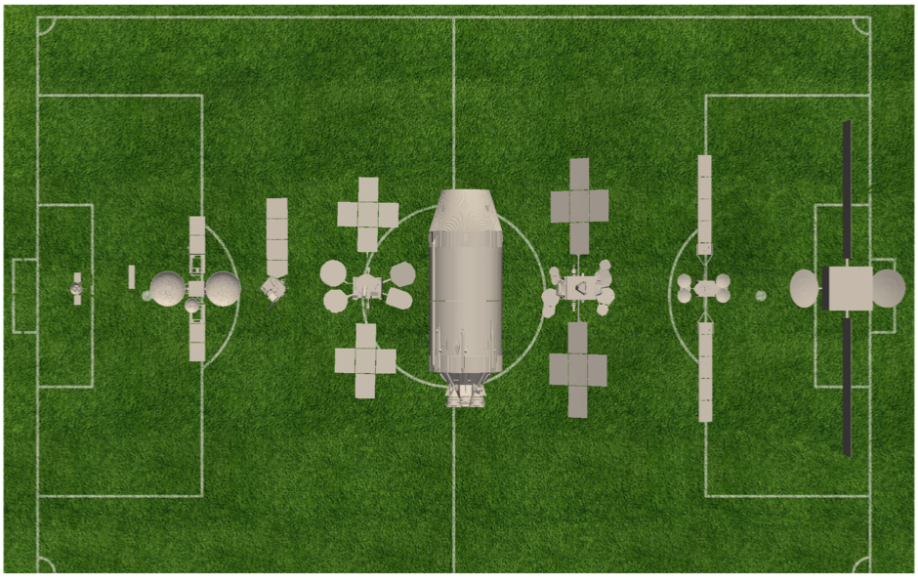

Figure 2.32. Selected space objects with soccer field for size reference. In order, the objects are TESS, Starlink V1, TDRS, Landsat 8, Hispasat 30W-6, Saturn V SII, TELSTAR 19V, HYLAS 4, and simplified ASTRA.

computed using Equation 2.51 and converted to ICRF using Eqs 2.54, 2.55, 2.56, 2.57, and 2.58. The position of the Sun is determined with SPICE following Section 2.4.8.

The attitude profile of the object is propagated with Eqs 2.9 and 2.8 using $\boldsymbol{M} = \mathbf{0}$ for torque free rigid body motion. The resulting attitude time history produces $\boldsymbol{q}(t)$, $\boldsymbol{\omega}(t)$, as well as the body frame vectors from the object to the Sun and observer depicted in Figure 2.34.

The BRDF — which varies across the surface of the object — is encoded in the `.obj` file in the red channel of the diffuse material color R such that $C_d = R$ and $C_s = 1 - R$. Given the unit vectors in the object body frame pointing towards the observer and the Sun, Algorithms 1 and 4 are used to render images of the object which are integrated to yield a mean normalized irradiance value $\check{I}$ with Eqs 2.41 and 2.42.

DISTRIBUTION A: Distribution approved for public release.

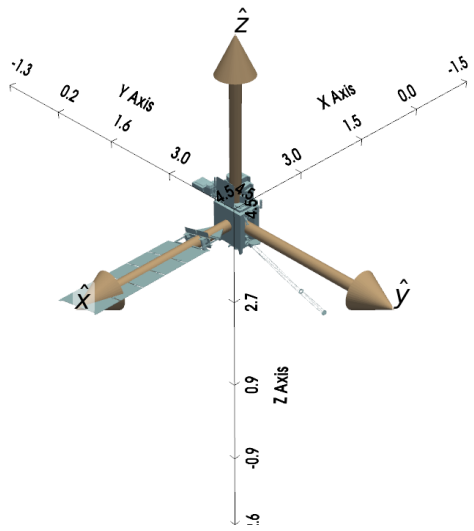

Figure 2.33. GOES 17 model for case 2

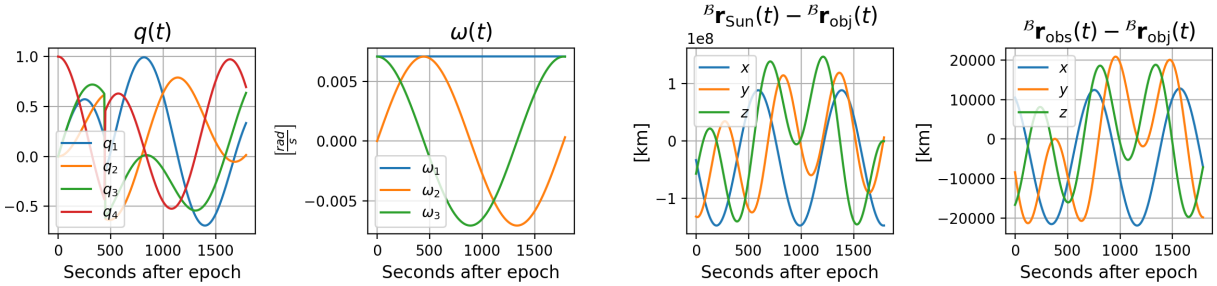

Figure 2.34. Attitude time history for case 2

This normalized irradiance is dimensionalized with Equation 2.32 to yield a mean irradiance I. Next, the background signal variances are computed for the Moonlight in Equation 2.91, zodiacal light in Equation 2.92, integrated starlight in Equation 2.87, twilight in Equation 2.85, light pollution in Equation 2.83, and airglow in Equation 2.81. These background signal variances are used to compute the overall background variance $\lambda_{\text{background}}$. The signal variance due to read noise, dark noise, and truncation noise are found in Table 6.1, yielding the overall mean and variance of the background pixels.

These means and variances are used to compute the SNR of each attempted observation using Equation 2.69. This SNR is used compute the minimum SNR constraint in Equation

DISTRIBUTION A: Distribution approved for public release.

2.98. The Moon exclusion angle constraint is also evaluated with Equation 2.99 and the minimum elevation constraint is evaluated with Equation 2.100. If all constraints are satisfied, the object is observable and the light curve measurement process can continue. Otherwise, the measurement is impossible and no value is saved for this timestep.

The mean value of the total photoelectron counts due to the object signal is computed from the mean irradiance I using Equation 2.78 using the telescope parameters in Table 6.1. This total mean count is then distributed across the CCD pixel grid using Equation 2.103. Now that all mean values are known, samples from the Poisson, Gaussian, and uniform distributions are sampled pixel-by-pixel to yield a final background and object signal on the CCD grid. The noisy light curve in ADU is then computed with Equation 2.105 and transformed back to irradiance with Equation 2.106, depicted in Figure 2.35.

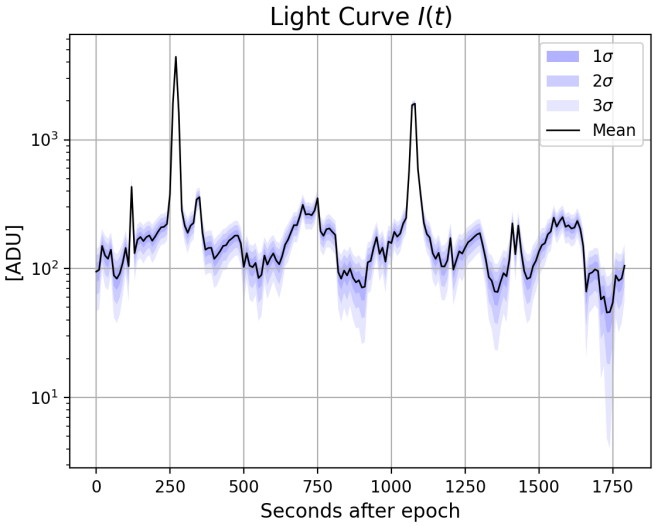

Figure 2.35. Light curve for case 2, produced with an object scale factor of 1/10 to exaggerate noise

Figure 2.35 possesses a few important characteristics to note when compared to the results from case 1 in Figure 2.31. The light curve for case 2 is much more complex, with higher frequency variation in the mean due to the many small geometric features making up the satellite model. As in the cube light curve, specular peaks are still evident around 260 and 1050 seconds after the simulation epoch. The noise is clearly seen in the regions

DISTRIBUTION A: Distribution approved for public release.

shaded by standard deviation. As a result of this noise, the lower magnitude signals regions — where little specular reflection is occurring — are much more corrupted by the noise as its standard deviation represents a larger fraction of the signal magnitude. Importantly, these regions possess high-frequency oscillations in the mean that are highly obscured in any one sampling due to the additive noise. This highlights the importance of specular reflection for extracting reliable accurate features by pinpointing the normal vectors of certain faces by reaching above the noise. It must be noted that Figure 2.35 was produced with a scale factor of 1/10 applied to the vertices of the GOES 17 3D model to make the effect of the noise more clear. In reality, large GEO objects like GOES should produce light curves with much less noise on the signal, as predicted by the simulator developed in this work.

DISTRIBUTION A: Distribution approved for public release.

REFERENCES

[1] ESA Space Debris Office, "Esa's annual space environment report," European Space Agency, Tech. Rep., Apr. 2022.

[2] N. G. S. F. Center, *Vanguard 1*, https://nssdc.gsfc.nasa.gov/nmc/spacecraft/display.action?id=1958-002B, Accessed: 2023-09-04.

[3] D. Vallado, *Fundamentals of Astrodynamics and Applications, 4th ed.* J. Wertz, Ed. Microcosm Press, Mar. 2013.

[4] C. Frueh, *Space traffic management*, Lecture Notes, 2019.

[5] S. Fan, "The light curve simulation and its inversion problem for human-made space objects," Ph.D. dissertation, Purdue University, Aug. 2020. DOI: 10.25394/PGS.12749570.v1.

[6] T. Schildknecht, R. Musci, and M. Fruh C. Ploner, "Color Photometry and Light Curve Observations of Space Debris in GEO," in *Advanced Maui Optical and Space Surveillance Technologies Conference*, C. Paxson, H. Snell, J. Griffin, *et al.*, Eds., Jan. 2008, E51, E51.

[7] T. Schildknecht, N. Koshkin, E. Korobeinikova, *et al.*, "Photometric Monitoring of Non-resolved Space Debris and Databases of Optical Light Curves," in *Advanced Maui Optical and Space Surveillance Technologies Conference*, Jan. 2015, 25, p. 25.

[8] A. Burton and S. Fan, "Mapping the solution space for light curve attitude estimation," *43rd COSPAR Scientific Assembly. Held 28 January-4 February*, vol. 43, p. 2193, 2021.

[9] H. Krag, "A method for the validation of space debris models and for the analysis and planning of radar and optical surveys," Ph.D. dissertation, Technische Universität Braunschweig, Mar. 2003.

[10] M. Kaasalainen, J. Torppa, and K. Muinonen, "Optimization methods for asteroid lightcurve inversion: Ii. the complete inverse problem," *Icarus*, vol. 153, no. 1, pp. 37–51, 2001, ISSN: 0019-1035. DOI: https://doi.org/10.1006/icar.2001.6674. [Online]. Available: https://www.sciencedirect.com/science/article/pii/S0019103501966746.

DISTRIBUTION A: Distribution approved for public release.

[11] S. Fan, C. Frueh, and A. Buzzoni, "A light curve simulation of the apollo lunar ascent module," in *AIAA/AAS Astrodynamics Specialist Conference*, 2016, pp. 1–10. DOI: 10.2514/6.2016-5504.

[12] A. M. Friedman, "Observability analysis for space situational awareness," Ph.D. dissertation, Purdue University, Apr. 2020. DOI: 10.25394/PGS.12196863.v1.

[13] D. Kobayashi and C. Frueh, "Compressed sensing for satellite characterization," in *Proceedings of the 20th AAS/AIAA Astrodynamics Specialist Conference*, Aug. 2020, pp. 1–20.

[14] C. Früh and M. K. Jah, "Coupled orbit attitude motion of high area-to-mass ratio (hamr) objects including efficient self-shadowing," *Acta Astronautica*, vol. 95, pp. 227–241, 2014, ISSN: 0094-5765. DOI: https://doi.org/10.1016/j.actaastro.2013.11.017.

[15] R. Furfaro, R. Linares, and V. Reddy, "Shape Identification of Space Objects via Light Curve Inversion Using Deep Learning Models," in *Proceedings of the 20th Advanced Maui Optical and Space Surveillance Technologies Conference*, S. Ryan, Ed., Sep. 2019, 17, p. 17.

[16] D. V. Cabrera, J. Utzmann, and R. Förstner, "Inversion of the shape of space debris from non-resolved optical measurements within spook," in *Proceedings of the 22nd Advanced Maui Optical and Space Surveillance Technologies Conference*, 2021, pp. 1–18.

[17] B. K. Bradley and P. Axelrad, "Lightcurve inversion for shape estimation of geo objects from space-based sensors," in *Proceedings of the International Symposium on Space Flight Dynamics*, 2014, pp. 1–20.

[18] R. Linares and J. L. Crassidis, "Space-object shape inversion via adaptive hamiltonian markov chain monte carlo," *Journal of Guidance, Control, and Dynamics*, vol. 41, no. 1, pp. 47–58, 2018.

[19] K. McNally, D. Ramirez, A. M. Anton, D. Smith, and J. Dick, "Artificial intelligence for space resident objects characterisation with lightcurves," in *Proceedings of the 8th European Conference on Space Debris*, ESA Space Debris Office, 2021, pp. 1–12.

[20] L. D. J. Blacketer, "Attitude characterisation of space objects using optical light curves," Ph.D. dissertation, University of Southampton, Mar. 2022. [Online]. Available: https://eprints.soton.ac.uk/457200/.

DISTRIBUTION A: Distribution approved for public release.

[21] J. Allworth, L. Windrim, J. Wardman, D. Kucharski, J. Bennett, and M. Bryson, "Development of a high fidelity simulator for generalised photometric based space object classification using machine learning," in *Proceedings of 70th International Astronautical Congress*, International Astronautical Congress, 2019, pp. 1–14. DOI: 10.48550/ARXIV.2004.12270. [Online]. Available: https://arxiv.org/abs/2004.12270.

[22] J. Allworth, L. Windrim, J. Bennett, and M. Bryson, "A transfer learning approach to space debris classification using observational light curve data," *Acta Astronautica*, vol. 181, pp. 301–315, Jan. 2021. DOI: 10.1016/j.actaastro.2021.01.048.

[23] T. Möller and B. Trumbore, "Fast, minimum storage ray-triangle intersection," *Journal of Graphics Tools*, vol. 2, Aug. 2005. DOI: 10.1145/1198555.1198746.

[24] B. T. Phong, "Illumination for computer generated pictures," in *Seminal Graphics: Pioneering Efforts That Shaped the Field*. New York, NY, USA: Association for Computing Machinery, 1998, pp. 95–101, ISBN: 158113052X. [Online]. Available: %5Curl%7Bhttps://doi.org/10.1145/280811.280980%7D.

[25] M. Ashikhmin and P. Shirley, "An anisotropic phong brdf model," *Journal of Graphics Tools*, vol. 5, Jan. 2001. DOI: 10.1080/10867651.2000.10487522.

[26] R. L. Cook and K. E. Torrance, "A reflectance model for computer graphics," *ACM Trans. Graph.*, vol. 1, no. 1, pp. 7–24, Jan. 1982, ISSN: 0730-0301. DOI: 10.1145/357290.357293. [Online]. Available: https://doi.org/10.1145/357290.357293.

[27] M. Oren and S. K. Nayar, "Generalization of lambert's reflectance model," in *Proceedings of the 21st Annual Conference on Computer Graphics and Interactive Techniques*, ser. SIGGRAPH '94, New York, NY, USA: Association for Computing Machinery, 1994, pp. 239–246, ISBN: 0897916670. DOI: 10.1145/192161.192213. [Online]. Available: https://doi.org/10.1145/192161.192213.

[28] W. Matusik, H. Pfister, M. Brand, and L. McMillan, "A data-driven reflectance model," *ACM Transactions on Graphics*, vol. 22, no. 3, pp. 759–769, Jul. 2003.

[29] H. N. Russell, "On the light-variations of asteroids and satellites," *The Astrophysical Journal*, vol. 24, no. 1, pp. 1–18, 1906.

[30] M. Kaasalainen and J. Torppa, "Optimization methods for asteroid lightcurve inversion: I. shape determination," *Icarus*, vol. 153, no. 1, pp. 24–36, 2001, ISSN: 0019-1035. DOI: https://doi.org/10.1006/icar.2001.6673. [Online]. Available: https://www.sciencedirect.com/science/article/pii/S0019103501966734.

DISTRIBUTION A: Distribution approved for public release.

[31] H. Minkowski, "Allgemeine lehrsätze über die konvexen polyeder," in *Ausgewählte Arbeiten zur Zahlentheorie und zur Geometrie: Mit D. Hilberts Gedächtnisrede auf H. Minkowski, Göttingen 1909*. Springer Vienna, 1909, ch. 22, pp. 121–139. [Online]. Available: https://doi.org/10.1007/978-3-7091-9536-9_5.

[32] J. J. Little, "An iterative method for reconstructing convex polyhedra from extended gaussian images," in *Proceedings of the Third AAAI Conference on Artificial Intelligence*, ser. AAAI'83, Washington, D.C.: AAAI Press, 1983, pp. 247–250.

[33] J. Durech and M. Kaasalainen, "Photometric signatures of highly nonconvex and binary asteroids," *Astronomy & Astrophysics*, vol. 404, no. 2, pp. 709–714, Jun. 2003. DOI: 10.1051/0004-6361:20030505.

[34] C.-K. Chng, M. Sasdelli, and T.-J. Chin, "Globally optimal shape and spin pole determination with light-curve inversion," *Monthly Notices of the Royal Astronomical Society*, vol. 513, no. 1, pp. 311–332, Jan. 2022, ISSN: 0035-8711. DOI: 10.1093/mnras/stac198. eprint: https://academic.oup.com/mnras/article-pdf/513/1/311/43446894/stac198.pdf. [Online]. Available: https://doi.org/10.1093/mnras/stac198.

[35] J. Durech, V. Sidorin, and M. Kaasalainen, "DAMIT: a database of asteroid models," *Astronomy and Astrophysics*, vol. 513, A46, A46, Apr. 2010. DOI: 10.1051/0004-6361/200912693.

[36] M. Kaasalainen, J. urech, and V. Sidorin, *DAMIT: Database of Asteroid Models from Inversion Techniques*, Astrophysics Source Code Library, record ascl:1412.004, Dec. 2014. ascl: 1412.004.

[37] B. Calef, J. Africano, B. Birge, D. Hall, and P. Kervin, "Photometric signature inversion," in *Unconventional Imaging II*, V. L. Gamiz, P. S. Idell, and M. S. Strojnik, Eds., International Society for Optics and Photonics, vol. 6307, SPIE, 2006, pp. 141–150. DOI: 10.1117/12.683015. [Online]. Available: https://doi.org/10.1117/12.683015.

[38] S. Fan and C. Frueh, "A direct light curve inversion scheme in the presence of measurement noise," *The Journal of the Astronautical Sciences*, vol. 67, Aug. 2019. DOI: 10.1007/s40295-019-00190-3.

[39] S. Fan and C. Frueh, "Multi-hypothesis light curve inversion scheme for convex objects with minimal observations," in *Proceedings of the 8th European Conference on Space Debris*, ESA Space Debris Office, 2021, pp. 1–7.

DISTRIBUTION A: Distribution approved for public release.

[40] A. M. Friedman and C. Frueh, "Observability of light curve inversion for shape and feature determination exemplified by a case analysis," *Journal of the Astronautical Sciences*, vol. 69, no. 2, pp. 537–569, Apr. 2022. DOI: 10.1007/s40295-021-00293-w.

[41] R. Linares, M. Jah, and J. Crassidis, "Inactive space object shape estimation via astrometric and photometric data fusion," *Advances in the Astronautical Sciences*, vol. 143, pp. 217–232, Jan. 2012.

[42] R. Linares, M. K. Jah, J. L. Crassidis, and C. K. Nebelecky, "Space object shape characterization and tracking using light curve and angles data," *Journal of Guidance, Control, and Dynamics*, vol. 37, no. 1, pp. 13–25, 2014. DOI: 10.2514/1.62986.

[43] R. Linares and R. Furfaro, "Space object classification using deep convolutional neural networks," in *19th International Conference on Information Fusion*, Jul. 2016, pp. 1–8.

[44] E. Kerr, G. P. Elisabeth, P. Talon, and D. Petit, "Using ai to analyse light curves for geo object characterisation," in *Proceedings of the 22nd Advanced Maui Optical and Space Surveillance Technologies Conference*, 2021, pp. 1–9.

[45] S. Karpov, E. Katkova, G. Beskin, *et al.*, "Massive photometry of low-altitude artificial satellites on Mini-Mega-TORTORA," in *Revista Mexicana de Astronomia y Astrofisica Conference Series*, ser. Revista Mexicana de Astronomia y Astrofisica Conference Series, vol. 48, Dec. 2016, pp. 112–113.

[46] C. Benson, D. Scheeres, and N. Moskovitz, "Light curves of retired geosynchronous satellites," in *7th European Conference on Space Debris*, vol. 7, 2017, p. 04.

[47] N. Koshkin, L. Shakun, E. Korobeynikova, *et al.*, "Monitoring of space debris rotation based on photometry," *Odessa Astronomical Publications*, vol. 31, pp. 179–185, 2018.

[48] Y. Wang, X. Du, J. Zhao, Z. Yin, and Y. Song, "What causes the abrupt changes in the light curve of a geo satellite?" *Acta Astronautica*, vol. 153, pp. 130–137, 2018, ISSN: 0094-5765. DOI: https://doi.org/10.1016/j.actaastro.2018.10.035. [Online]. Available: https://www.sciencedirect.com/science/article/pii/S0094576518313857.

[49] Space-Track.org, *Space-track.org*, https://www.space-track.org/, Accessed: 2023-10-10, 2023.

DISTRIBUTION A: Distribution approved for public release.

[50] T. Payne, F. Hoots, A. Butkus, Z. Slatton, and D. Nguyen, "Improvements to the sgp4 propagator (sgp4-xp)," in *Proceedings of the 2022 AMOS Technical Conference*, 2022.

[51] C. J. Benson, D. J. Scheeres, W. H. Ryan, and E. V. Ryan, "Cyclic complex spin state evolution of defunct geo satellites," in *Proceedings of the Advanced Maui Optical and Space Surveillance Technologies Conference, Maui, HI*, 2018.

[52] F. L. Markley and J. L. Crassidis, *Fundamentals of Spacecraft Attitude Determination and Control*. Springer, May 2014.

[53] M. D. Shuster, "Survey of attitude representations," *Journal of the Astronautical Sciences*, vol. 41, no. 4, pp. 439–517, Oct. 1993.

[54] *Wavefront obj file format*, https://www.loc.gov/preservation/digital/formats/fdd/fdd000507.shtml, Accessed: 2023-08-30, 2020.

[55] B. Duvenhage, K. Bouatouch, and D. Kourie, "Numerical verification of bidirectional reflectance distribution functions for physical plausibility," in *SAICSIT '13: Proceedings of the South African Institute for Computer Scientists and Information Technologists Conference*, Oct. 2013, pp. 200–208, ISBN: 9781450321129. DOI: 10.1145/2513456.2513499.

[56] R. M. Soldado and C. U. Almagro, "An overview of brdf models," 2012. [Online]. Available: https://api.semanticscholar.org/CorpusID:44900609.

[57] F. Fankhauser, J. A. Tyson, and J. Askari, "Satellite optical brightness," *The Astronomical Journal*, vol. 166, no. 2, p. 59, Jul. 2023. DOI: 10.3847/1538-3881/ace047. [Online]. Available: https://doi.org/10.3847%2F1538-3881%2Face047.

[58] P. Shirley and S. Marschner, *Fundamentals of Computer Graphics*, 3rd. USA: A. K. Peters, Ltd., 2009, ISBN: 1568814690.

[59] W. Keeter, *Nasa 3d models*, https://nasa3d.arc.nasa.gov/models/, Accessed: 2022-04-27, Feb. 2013.

[60] H. Kolivand and M. S. Sunar, "Survey of shadow volume algorithms in computer graphics," *IETE Technical Review*, vol. 30, no. 1, pp. 38–46, 2013. DOI: 10.4103/0256-4602.107338.

DISTRIBUTION A: Distribution approved for public release.

[61] S. Brabec, T. Annen, and H.-P. Seidel, "Practical shadow mapping," *Journal of Graphics Tools*, vol. 7, no. 4, pp. 9–18, 2002.

[62] R. Santamaria, *Raylib*, https://www.raylib.com, Accessed: 2022-04-28, Nov. 2021.

[63] O. Montenbruck and E. Gill, *Satellite orbits: models, methods, and applications*. Springer Science & Business Media, 2012.

[64] N. J. P. Laboratory, *Spice*, https://naif.jpl.nasa.gov/naif/toolkit.html, Accessed: 2023-10-24, 2023.

[65] D. Newell and E. Tiesinga, *The international system of units (si), 2019 edition*, en, Aug. 2019. DOI: https://doi.org/10.6028/NIST.SP.330-2019.

[66] L. T. Sharpe, A. Stockman, W. Jagla, and H. Jägle, "A luminous efficiency function, $V^{\star}(\lambda)$, for daylight adaptation," *Journal of Vision*, vol. 5, no. 11, pp. 3–3, Dec. 2005, ISSN: 1534-7362. DOI: 10.1167/5.11.3. eprint: https://arvojournals.org/arvo/content_public/journal/jov/932833/jov-5-11-3.pdf. [Online]. Available: https://doi.org/10.1167/5.11.3.

[67] G. M. Daniels, "A night sky model for satellite search systems.," *Optical Engineering*, vol. 16, pp. 66–71, Feb. 1977.

[68] K. A. Pickering, "The Southern Limits of the Ancient Star Catalog and the Commentary of Hipparchos," *DIO*, vol. 12, pp. 3–27, Sep. 2002.

[69] F. Falchi, P. Cinzano, D. Duriscoe, *et al.*, *Supplement to: The new world atlas of artificial night sky brightness. v. 1.1. gfz data services.* https://doi.org/10.5880/GFZ.1.4.2016.001, Accessed: 2023-08-25, 2016.

[70] F. Falchi, P. Cinzano, D. Duriscoe, *et al.*, "The new world atlas of artificial night sky brightness," *Science Advances*, vol. 2, no. 6, e1600377, 2016. DOI: 10.1126/sciadv.1600377. eprint: https://www.science.org/doi/pdf/10.1126/sciadv.1600377. [Online]. Available: https://www.science.org/doi/abs/10.1126/sciadv.1600377.

[71] F. Patat, O. S. Ugolnikov, and O. V. Postylyakov, "UBVRI twilight sky brightness at ESO-Paranal," *Astronomy and Astrophysics*, vol. 455, no. 1, pp. 385–393, Aug. 2006. DOI: 10.1051/0004-6361:20064992. arXiv: astro-ph/0604128 [astro-ph].

DISTRIBUTION A: Distribution approved for public release.

[72] A. e. a. Vallenari, "Gaia Data Release 3. Summary of the content and survey properties," *Astronomy & Astrophysics*, vol. 674, A1, A1, Jun. 2023. DOI: 10.1051/0004-6361/202243940. arXiv: 2208.00211 [astro-ph.GA].

[73] J. C. Segovia, *Astroquery.gaia package*, https://astroquery.readthedocs.io/en/latest/gaia/gaia.html, Accessed: 2023-08-21, 2016.

[74] F. E. Roach, "A Photometric Model of the Zodiacal Light," *Astronomical Journal*, vol. 77, p. 887, Dec. 1972. DOI: 10.1086/111363.

[75] A. Burton, L. Robinson, and C. Frueh, "Attitude estimation from light curves using particle swarm optimizers," in *International Orbital Debris Conference*, 2023.

[76] T. Campbell, A. Battle, B. Gray, *et al.*, "Physical characterization of moon impactor we0913a," *The Planetary Science Journal*, vol. 4, p. 217, Nov. 2023. DOI: 10.3847/PSJ/acffb8.

[77] M. Kaasalainen and J. Torppa, "Optimization methods for asteroid lightcurve inversion: I. shape determination," *Icarus*, vol. 153, no. 1, pp. 24–36, 2001, ISSN: 0019-1035. DOI: https://doi.org/10.1006/icar.2001.6673. [Online]. Available: https://www.sciencedirect.com/science/article/pii/S0019103501966734.

[78] B. Horn, "Extended gaussian images," *Proceedings of the IEEE*, vol. 72, no. 12, pp. 1671–1686, 1984. DOI: 10.1109/PROC.1984.13073.

[79] J. J. Little, "Extended gaussian images, mixed volumes, shape reconstruction," in *Proceedings of the First Annual Symposium on Computational Geometry*, ser. SCG '85, Baltimore, Maryland, USA: Association for Computing Machinery, 1985, pp. 15–23, ISBN: 0897911636. DOI: 10.1145/323233.323236. [Online]. Available: https://doi.org/10.1145/323233.323236.

[80] C. L. Lawson and R. J. Hanson, "Solving least squares problems," in *Classics in applied mathematics*, 1976. [Online]. Available: https://api.semanticscholar.org/CorpusID:122862057.

[81] R. Bro and S. De Jong, "A fast non-negativity-constrained least squares algorithm," *Journal of Chemometrics*, vol. 11, no. 5, pp. 393–401, 1997. DOI: https://doi.org/10.1002/(SICI)1099-128X(199709/10)11:5<393::AID-CEM483>3.0.CO;2-L. [Online]. Available: https://analyticalsciencejournals.onlinelibrary.wiley.com/doi/abs/10.1002/%28SICI%291099-128X%28199709/10%2911%3A5%3C393%3A%3AAID-CEM483%3E3.0.CO%3B2-L.

DISTRIBUTION A: Distribution approved for public release.

[82] B. Keinert, M. Innmann, M. Sänger, and M. Stamminger, "Spherical fibonacci mapping," *ACM Transactions on Graphics*, vol. 34, no. 6, pp. 1–7, 2015.

[83] E. W. Weisstein, *Sphere point picking*, https://mathworld.wolfram.com/SpherePointPicking.html, Accessed: 2022-07-03, 2002.

[84] R. Gardner and P. Milanfar, "Reconstruction of convex bodies from brightness functions," *Discrete and Computational Geometry*, vol. 29, pp. 279–303, Jul. 2003. DOI: 10.1007/s00454-002-0759-2.

[85] A. R. Conn, N. I. M. Gould, and P. L. Toint, *Trust-Region Methods*. Philadelphia, PA, USA: SIAM, 2000.

[86] C. T. Loop, "Smooth subdivision surfaces based on triangles," Ph.D. dissertation, University of Utah, Aug. 1987. [Online]. Available: https://www.microsoft.com/en-us/research/publication/smooth-subdivision-surfaces-based-on-triangles/.

[87] L. Robinson and C. Frueh, "Light curve inversion for reliable shape reconstruction of human-made space objects," in *Proceedings of the 32nd AIAA/AAS Astrodynamics Specialist Conference*, Sep. 2022, pp. 1–19.

[88] A. Bærentzen and H. Aanæs, "Generating signed distance fields from triangle meshes," Jan. 2002.

[89] D. Cohen-Or, D. Levin, and A. Solomovici, "Three-dimensional distance field metamorphosis," *ACM Transactions on Graphics*, vol. 17, Feb. 2000. DOI: 10.1145/274363.274366.

[90] W. E. Lorensen and H. E. Cline, "Marching cubes: A high resolution 3d surface construction algorithm," in *Proceedings of the 14th Annual Conference on Computer Graphics and Interactive Techniques*, ser. SIGGRAPH '87, New York, NY, USA: Association for Computing Machinery, 1987, pp. 163–169, ISBN: 0897912276. DOI: 10.1145/37401.37422. [Online]. Available: https://doi.org/10.1145/37401.37422.

[91] W. Schroeder, R. Maynard, and B. Geveci, "Flying edges: A high-performance scalable isocontouring algorithm," Oct. 2015. DOI: 10.13140/RG.2.1.3415.9609.

[92] S. M. Omohundro, *Five balltree construction algorithms*. International Computer Science Institute Berkeley, 1989.

DISTRIBUTION A: Distribution approved for public release.